

Early-Stage Innovations (ESI)
NASA Grant Number **80NSSC22K0263**

Advanced Lightweight Heat Rejection Radiators for Space Nuclear Power Systems

Final Report


Submission Date 02/14/2025

Unique Entity Identifier (UEI) number, also known as a DUNS number, and EIN
number: **F6XLTRUQJEN4**

The University of New Mexico, 1700 Lomas Blvd NE STE 2200,
Albuquerque, NM 87131

University Identifying Number (if any)

Reporting Period: (01/18/2022 - 01/17/2025)

Principal Investigator	Mohamed S. El-Genk, Distinguished and Regents' Professor and Founding Director, Institute for Space and Nuclear Power Studies https://isnsp.unm.edu/ , University of New Mexico, Albuquerque, NM 87131. mgenk@unm.edu, Ph: 505-277-5442.
NASA Research Collaborator	NASA RC Fernando Reyes Tirado, MSFC
Grant Period of Performance	01/18/2022 - 01/17/2025
Final Report	<input checked="" type="checkbox"/> Yes <input type="checkbox"/> No
PI Signature (Digital or Handwritten)	 Recoverable Signature X Mohamed S. El-Genk <hr/> Principal Investigator (PI) Signed by: dc3670d7-0642-41c7-83ff-2fa1937967f7

Advanced Lightweight Heat Rejection Radiators for Space Nuclear Power Systems

Mohamed S. El-Genk and Timothy M. Schriener

Institute for Space and Nuclear Power Studies and Nuclear
Engineering Department, <https://isnps.unm.edu/>

The University of New Mexico, Albuquerque, NM.

FINAL REPORT

Submitted

14 February 2025

Table of Contents

List of Figures	iv
List of Tables	viii
Executive Summary	1
1. Background	3
2. Research Objectives and Summary of Accomplishments	10
3. Lightweight Heat Pipe Radiator Design Concepts	14
3.1. <i>NaK-78 flow duct design and thermal analysis</i>	16
3.2 <i>Radiator panel design</i>	17
4. Thermal Analysis of Advanced Lightweight Radiator Modular Designs	19
4.1 <i>3-D CFD thermal analyses of heat pipe radiator modules</i>	21
4.2 <i>Results and discussion</i>	22
5. Micrometeoroid Protection Analyses of Radiator Panel on Lunar Surface	25
5.1 <i>Micrometeoroid and orbital debris environmental models</i>	25
5.2 <i>Methodology and approach</i>	28
5.3 <i>Armor analysis results</i>	30
5.3.1 <i>Estimates of C-C armor for Cs-Ti heat pipes</i>	32
5.3.2 <i>C-C Arming HOPG/Ti heat spreading fins</i>	35
5.4. <i>Summary</i>	39
6. Finite Element Stress Analyses of Heat Pipe Module and Panel During Launch	40
6.1 <i>Approach</i>	41
6.2 <i>Analyses Methodology</i>	42
6.3. <i>Numerical Meshing and Sensitivity Analysis</i>	43
6.4. <i>Single HP radiator module stress analyses</i>	47
6.5. <i>Launch vibration stress analysis of ten modules radiator panel</i>	54
6.5. <i>Summary</i>	59
7. Performance Parameters and Estimates of the Heat Pipe Radiator Panel	61
8. Summary and Conclusions	64
9. Dissemination of Results	65
10. NASA Collaboration	67
11. Annual Technical Seminars	68
12. New Technology, Reportable Items, Inventions, and Patents	69
13. Students	70
14. Technology Outlook	71
Acknowledgements	72
Nomenclature	73
References	76

List of Figures

- Figure 1:** Conceptual layouts and surface temperatures of heat pipe heat rejection radiators for space nuclear reactor power systems with different energy conversion options. 3
- Figure 2:** Conceptual layout of heat pipe heat rejection radiators of select nuclear reactor systems with TE and CBC energy conversion for lunar surface power. 4
- Figure 3:** Comparisons of the saturation vapor pressures and Figure of Merit (FOM) curves of candidate heat pipe working fluids as function of operating temperature [24]. 5
- Figure 4:** Heat pipe equivalent diameters for operating in continuum and transition flow regimes of Cs, Rb, and K working fluids versus temperature [24]. 5
- Figure 5:** Section views of the evaporator and condenser of the Version 4 heat pipe module with redesigned NaK-78 flow duct [24]. 14
- Figure 6:** Developed lightweight Cs-Ti heat pipe radiator modules armored C-C composite fibers and with 10 cm wide HOPG/Ti heat spreading fins for rejecting waste heat at surface average temperature of 600 K into space. 15
- Figure 7:** Developed designs of Ver. 6 and Ver. 8 lightweight Cs-Ti heat pipe radiator modules with 10 cm wide HOPG/Ti heat spreading fins. 16
- Figure 8:** Exterior and x-ray views of the liquid NaK-78 flow duct of the developed Cs-Ti heat pipe module showing the orifice plates and the dividing ribs. 17
- Figure 9:** A radiator panel comprised of ten, Ver. 7 Cs-Ti heat pipe modules which are hydraulically coupled in parallel and mounted within aluminum frame for structural support. 18
- Figure 10:** Comparison of the speed of Cs vapor exiting the evaporator sections of the Cs-Ti heat pipes in Versions 4, 5, 6, and 7 radiator modules, with the same evaporator section length, $L_{ev} = 10$ cm and width of heat spreading fins, $W_{fin} = 10$ cm, versus the heat pipe power throughput. 19
- Figure 11:** Section view of the computational numerical mesh grid within the straight section of the liquid NaK-78 flow duct [24]. 20
- Figure 12:** Spatial distributions of the surface temperatures for Ver. 6, 7, and 8 radiator modules for $W_{fin} = 10$ cm, NaK-78 $T_{in} = 650$ K and $\dot{m} = 1.56$ kg/s [24]. 21
- Figure 13:** Estimates of the HP entrainment limit and the Power throughput Ver. 4, 5, 6, 7, and 8 of the Cs-Ti heat pipe radiator modules calculated using HPTrAM™ at NaK-78 inlet temperature of 650 K, versus equivalent hydraulic diameter of Cs vapor flow [24].

	23
Figure 14: Comparison of the micrometeoroid cumulative interplanetary flux distributions for NASA's MEM [36], ESA's IMEM1 [37] and IMEM2 [38] and the micrometeoroid model of Gruen et al. [41] versus the micrometeor mass in grams [27].	
	27
Figure 15: Comparisons of perforation probabilities of Cs-Ti heat pipes with C-C composite armor in radiator modules in Fig. 6, using MEM, IMEM1, and IMEM2 for incident particles densities of 1.0 and 2.5 g/cm ³ [51].	
	31
Figure 16: Perforation probability estimates of Cs-Ti heat pipes with C-C composite armor in Ver. 4-7 radiator modules (Fig. 6) for incident particle densities of 1.0 and 2.5 g/cm ³ [51].	
	33
Figure 17: Mass estimates of the C-C composite armor of the Cs-Ti heat pipes C-C in the Vers. 4-7 modules (Fig. 6) using NASA's MEM [51].	
	34
Figure 18: Comparison of the estimated penetration probabilities of the 10 cm-wide HOPG/Ti heat spreading fins in Vers. 4-7 radiator modules (Fig. 6), using ESA IMEM1, NASA MEM and ESA IMEM2 for 1.0 and 2.5 g/cm ³ incident particle densities [51].	
	36
Figure 19: Estimates based on NASA's MEM of the penetration probability of the HOPG/Ti heat spreading fins of Vers. 4-7 radiator modules in Fig. 6, for particle densities of 1.0 and 2.5 g/cm ³ [51].	
	37
Figure 20: Mass estimates of the C-C composite armor of the HOPG/Ti heat spreading fins in Vers. 4-7 radiator modules in Fig. 6 [51].	
	38
Figure 21: Lateral sinusoidal acceleration loads experienced by payloads onboard the Falcon Heavy and Delta IV Heavy launch vehicles [55, 56].	
	41
Figure 22: Single Ver. 7 heat pipe module in metal support frame used in the performed FEA of the induced solid stresses.	
	42
Figure 23: Section view of the numerical mesh gride used in performed sensitivity analysis for Ver. 7 heat pipe module (Fig. 5a).	
	43
Figure 24: Images of the induced Von Mises stress along the inner surface of the Ti wall of the Cs-Ti heat pipe and NaK-78 flow duct of Ver. 7 module with Meshes 1 and 2 and for 5 Hz lateral vibration load.	
	45
Figure 25: Images of the calculated Von Mises stresses along the inner surface of the Ti wall of the Cs-Ti heat pipe and NaK-78 flow duct of Ver. 7 module with Meshes 3 and 4 and for 5 Hz lateral vibration load.	
	45

Figure 26: Enlarged images of the calculated Von Mises stress at the ends of the Cs-Ti heat pipe in Fig. 24 using Meshes 1 and 2 for 5 Hz lateral vibration load.

46

Figure 27: Enlarged views of Von Mises stress for the ends of the Cs-Ti heat pipe in Fig. 25 for Meshes 3 and 4 with 5 Hz lateral vibration load.

46

Figure 28: Effect of the number of mesh gride cells on the highest calculated Von Mises stress and vertical displacement for the Ver. 7 heat pipe module.

47

Figure 29: Calculated vertical displacement for the Ver. 7 heat pipe module for the lateral sinusoidal acceleration loads of the Falcon Heavy and Delta IV Heavy launch vehicles at 5 Hz and 100 Hz frequencies.

48

Figure 30: Image of the calculated Von Mises stress along the inner surface of the Ti wall of the Cs-Ti heat pipe and the NaK-78 flow duct of Ver. 7 heat pipe module for Falcon Heavy launch loads with frequencies of 5, 50, and 100 Hz (images not to scale).

49

Figure 31: Calculated images on the induced Von Mises stress along the inner surface of the Ti wall of the Cs-Ti heat pipe and NaK-78 flow duct of Ver. 7 heat pipe module for Delta IV Heavy launch loads with frequencies of 5, 50, and 100 Hz (images not to scale).

49

Figure 32: Enlarged images of the calculated Von Mises stress in the Ti wall of the Cs-Ti heat pipe and NaK-78 flow duct of Ver. 7 heat pipe module, at the ends of the Cs-Ti heat pipe in Fig. 30, for the Falcon Heavy acceleration loads.

50

Figure 33: Enlarged views of induced Von Mises stresses in the Ti wall of the Cs-Ti heat pipe and NaK-78 flow duct of Ver. 7 heat pipe module at the ends of the Cs-Ti heat pipe in Fig. 31 for the Delta IV Heavy acceleration loads.

51

Figure 34: Plots of Von Mises stresses along the Ti cladding of the HOPG/Ti fins for the Ver. 7 heat pipe module due to the lateral sinusoidal acceleration loads of the Falcon Heavy launch vehicle at frequencies of 5 and 100 Hz.

52

Figure 35: Plots of the calculated Von Mises stresses along the Ti cladding of the HOPG/Ti fins of Ver. 7 heat pipe radiator module, subject to the lateral sinusoidal acceleration loads of the Delta IV Heavy launch vehicle at frequencies of 5 Hz and 100 Hz.

53

Figure 36: Highest calculated Von Mises stress in the Ti heat pipe wall and tensile stress in the HOPG layer of the heat spreading fins for a single Ver. 7 heat pipe radiator module versus vibration frequency of the lateral loads for Falcon Heavy and Delta IV Heavy launch vehicles.

54

Figure 37: Integrated radiator panel of ten Ver. 7 heat pipe modules in support frame.

54
Figure 38: Calculated vertical displacement along midpoint of radiator panel with ten Ver. 7 heat pipe modules subject to the launch loads of the Falcon Heavy at 5, 25, and 50 Hz.

55
Figure 39: Images of the calculated Von Mises stresses along the inner surface of the Ti walls of the Cs-Ti heat pipes in the integrated panel with ten Ver. 7 heat pipe modules, for the Falcon Heavy launch loads and frequencies of 5, 25, and 50 Hz.

56
Figure 40: Images of calculated Von Mises stress in Ti walls of NaK-78 flow ducts of integrated radiator panel with ten Ver. 7 heat pipe modules for the Falcon Heavy at 5, 25, and 50 Hz.

56
Figure 41: Calculated Von Mises stress for the Ti cladding of the HOPG/Ti fins in the integrated panel with ten Ver. 7 modules for Falcon Heavy at 5, 25, and 50 Hz.

57
Figure 42: Plots of calculated Von Mises stresses along the Ti cladding of the HOPG/Ti fins for the radiator panel of ten Ver. 7 modules subject to lateral sinusoidal acceleration loads of the Falcon Heavy launch vehicle at 5, 25, and 50 Hz.

58
Figure 43: Comparison of the highest calculated Von Mises stress in the Ti heat pipe walls and the tensile stress in the HOPG heat spreading fins for ten Ver. 7 modules integrated radiator panel subject to the lateral launch loads of the Falcon Heavy launch vehicle at 5 -100 Hz.

59

List of Tables

Table 1: Comparison of reported operation parameters of selected nuclear reactor systems with static and dynamic energy conversion for space exploration and lunar surface power [2,4-17].	6
Table 2: Operation parameters of heat pipe heat rejection radiators for nuclear reactor systems with static and dynamic energy conversion for space exploration and lunar surface power. [2,4-17]	7
Table 3. NASA operation requirements for developing a lightweight heat rejection radiator.	10
Table 5. Estimates of the C-C armor thicknesses of the Ti-Cs heat pipe in the radiator modules (Fig. 6) for perforation probabilities of 1%, 5%, and 10% for 10 years on lunar surface [51].	33
Table 6. Comparison of the mass estimates of C-C armor of the Ti-Cs heat pipes in the radiator modules (Fig. 6) for proliferation probabilities of 1%, 5%, and 10% in 10 years on lunar surface with particle densities of 1.0 and 2.5 g/cm ³ [51].	35
Table 7. C-C composite armor thickness the heat spreading fins in radiator modules (Fig. 6) for 10 years on lunar surface and penetration probabilities of 2%, 5%, and 10% [51].	37
Table 8. Mass estimates of the C-C armor of the heat spreading fins of radiator modules in Fig. 6 for 10-year on the lunar surface and penetration probabilities of 2, 5, and 10% [51].	38
Table 9. Numerical Mesh Parameters for Mesh Sensitivity Analysis of Ver. 7 Heat Pipe Module.	44
Table 10. Estimates comparison of the total rejected power (kW), total mass (kg), specific power (kW/kg), areal density (kg/m ²) and power density (kW/m ²) of C-C composite armored radiator panels, each of ten Ver. 4, 5, 6, 7, and 8 designs of Cs-Ti heat pipe radiator modules (Figs. 6, 7, and 15).	62

Executive Summary

Nuclear power and propulsion systems will enable future NASA human exploration and settlement on the Moon and Mars. These systems' radiators for rejecting waste heat into space could be large and massive. Therefore, it is desirable to develop much lighter heat rejection radiators than the current State-of-the-Art (SOA). This NASA Early Stages Innovation Phase 1 project developed a lightweight foldable radiator panel design with a specific mass $< 3 \text{ kg/m}^2$ for waste heat rejection into space on the lunar surface at an average temperature of 600 K. The novel and modular radiator panel design developed by the University of New Mexico's Institute for Space and Nuclear Power Studies (UNM-ISNPS) comprise ten modules of Cesium (Cs)-Titanium (Ti) heat pipes and lightweight Highly Oriented Pyrolytic Graphite (HOPG) / Ti fins heat spreading fins. The heat pipes provide almost isothermal thermal power transport and rejection into space and are adequately armored using C-C composite fabric to protect against impact by space debris and micrometeoroids, for a perforation probability of $\leq 10\%$ over a service life of 10 years on the lunar surface.

The 10-cm long evaporator sections of the Cs-Ti heat pipes are integrated into specially designed flow ducts. The ducts increase the interfacial area for thermal coupling with the circulating liquid NaK-78 through the duct at $> 625 \text{ K}$. In addition, the assembled modules into the radiator panel are thermal-hydraulically coupled in parallel. The performance of the Cs-Ti heat pipe modules is calculated using a comprehensive 2-D Heat Pipe Transient Analysis Model (HPTTrAM™) including the determinations of the prevailing operation limits and of Cs vapor and liquid pressure distributions. The HPTTrAM™ is thermally coupled with a 3-D Computational Fluid Dynamics (CFD) code to analyze the performance of the integrated Cs-Ti radiator modules with HOPG/Ti heat spreading fins. Performed analyses investigated the effects of changing the Cs vapor flow area in the heat pipes and the lengths of the evaporator and condenser sections, and the NaK-78 flow duct to evaporator section.

The performed micrometeoroid protection analysis for the heat pipe radiator modules determined the thicknesses of the applied C-C composite armor on the outer surfaces of the Cs-Ti heat pipes and the HOPG/Ti fins for a 10-year service lifetime on the lunar surface. The results show that C-C composite armor 0.78-0.58 mm thick on the Cs-Ti heat pipes reduces the *perforation* probability by a micrometeoroid to $\leq 10\%$ for 10 years' service. The C-C armor needed for the HOPG/Ti heat spreading fins is much less, being $< 0.1 \text{ mm}$ for a *penetration* probability of $\leq 10\%$ for the same service life.

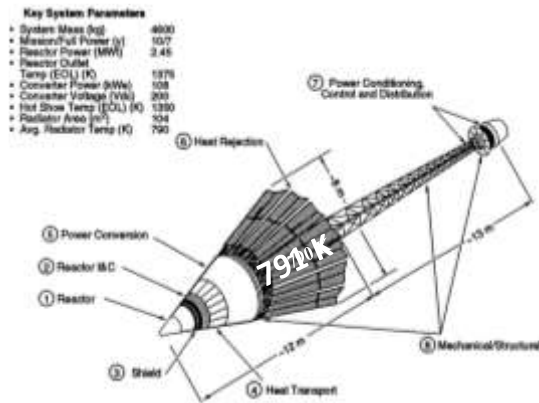
The performed Finite Element solid stress Analysis (FEA) simulations of a radiator panel with ten Cs-Ti HP modules estimate the induced structural stresses due to the low frequency vibration loads of 5-100 Hz during launch from Earth. The analysis modeled the lateral vibration loads for the Falcon Heavy and Delta IV Heavy launch vehicles. The induced highest Von Mises stresses for the Cs-Ti heat pipes and in the wall of the NaK-78 flow ducts in the radiator panel are less than 10.9% of the yield strength of the Grade 5 titanium alloy (Ti-6Al-4V). The highest induced tensile stress in the HOPG/Ti fins is below the bending failure criteria for the HOPG within the Ti casing.

The bonding at the interface of the HOPG with Ti in the heat spreading fins and of Ti with C-C composite armor has also been investigated using Transmission Electron Microscopy (TEM) and Scanning Electron Microscopy (SEM) techniques and methods. These investigations yielded satisfactory results confirming sound bonding at the interfaces. The investigations used 1-2 μm thick deposited Ti layers using Magnetron sputtering onto HOPG and C-C composite samples. The coated samples were exposed to hard vacuum ($\sim 2\text{-}1.5 \times 10^{-7}$ torr) in the UNM-ISNPS vacuum test facility for many weeks prior to the characterization of the interfaces. Characterization using TEM and Energy Dispersive X-ray analysis shows a clean, continuous C-Ti interface without the formation of carbides.

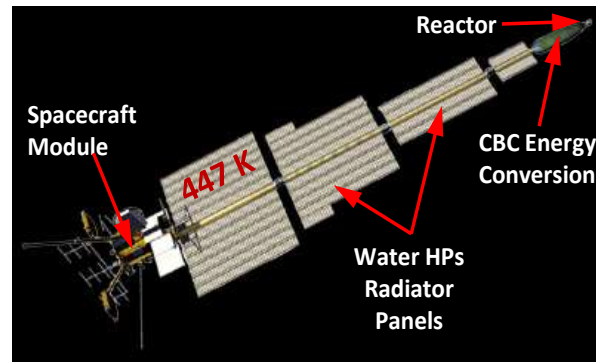
The developed C-C composite armored lightweight heat rejection radiator panel of ten modulus of Cs-Ti heat pipes and HOPG/Ti heat spreading fins, by UNM-ISONPS in this project, has an areal density $\leq 3.0 \text{ kg/m}^2$ and specific heat rejection power $\geq 3.8 \text{ kW/kg}$. These values are considerable improvements over those reported for SOA radiators of $5.24 - 12.7 \text{ kg/m}^2$ and $0.1 - 2.68 \text{ kW/kg}$, respectively. This innovative design developed in this project of a lightweight heat pipe radiator panel for fission surface power system on the lunar surface would reduce launch mass and cost. The design concept would also be applicable to nuclear reactor power systems for space exploration and nuclear electric propulsion systems to support NASA's future missions for the Moon, Mars, and throughout the solar system.

15. Background

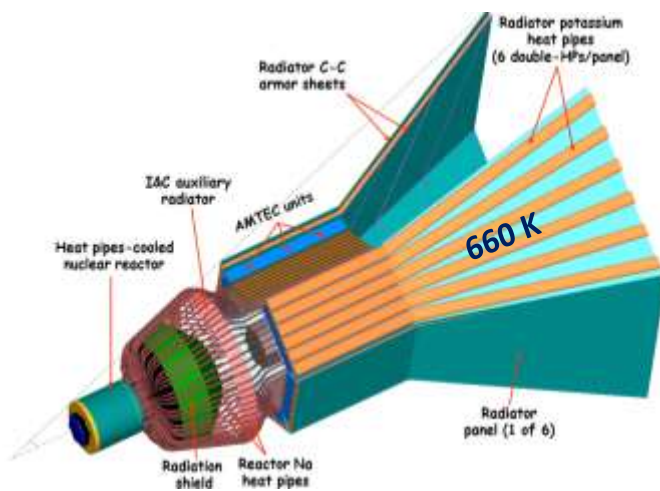
Nuclear reactor systems are enabling future space exploration in the solar system and human exploration of the Earth Moon, Mars and the icy moons of Jupiter and Saturn, and beyond [1-2]. These compact and lightweight power systems can continuously supply tens to 1000's kW of electrical power 24/7, independent of the sun, for 7-10 years or even longer [1-3]. Images of some of the developed nuclear reactor power systems for space exploration mission are presented in Fig. 1 and those for lunar surface power are presented in Fig. 2.



(a) GE SP-100 Generic Flight System 110 kW_e [Ref. 4]



(b) Prometheus JIMO CBC Power System 208 kW_e [Refs. 12,13]



(c) UNM-ISNPS SAIRS AMTEC Power System 111 kW_e [Ref. 7]

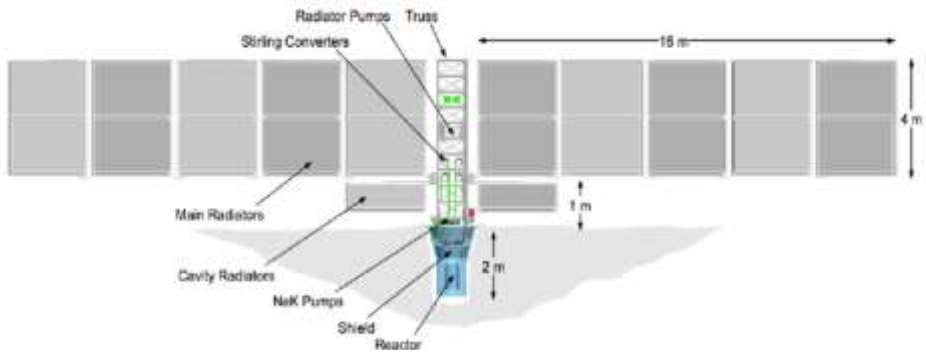


(d) NASA Kilopower Space Power System 1 kW_e [Ref. 9]

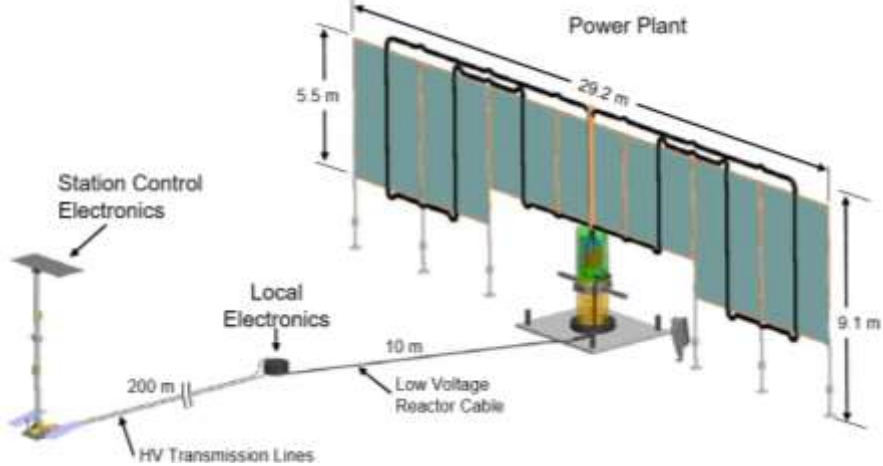
Figure 1: Conceptual layouts and surface temperatures of heat pipe heat rejection radiators for space nuclear reactor power systems with different energy conversion options.

Nuclear reactor power systems for space exploration comprise a compact reactor at one end, followed by a truncated cone radiation shadow shield for protecting the electronics of the payload. The payload is located a distance away from the reactor to further reduce the radiation dose to the payload from the neutrons and gamma photons emanating from the reactor during operation. The truncated cone radiator for rejecting waste heat from the energy

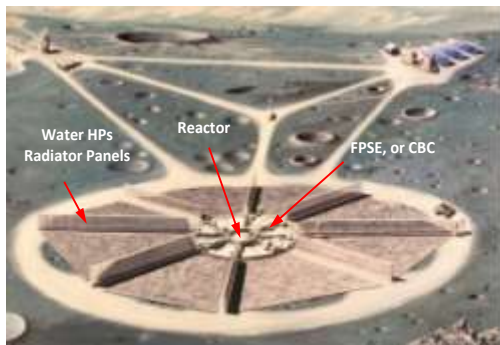
conversion subsystem into space is placed behind the radiation shadow shield. The reactor control element drives, the Power Management and Distribution (PMD) subsystem, the stowed boom of the payload, and the payload are placed behind the radiation shadow shield within the radiator cavity during launch. The waste heat rejection radiator is the most voluminous and could be the most massive component of a space nuclear reactor power system, depending on the surface average temperature for heat rejection, the reactor thermal power and the power system efficiency (Tables 1 and 2) [4-17].



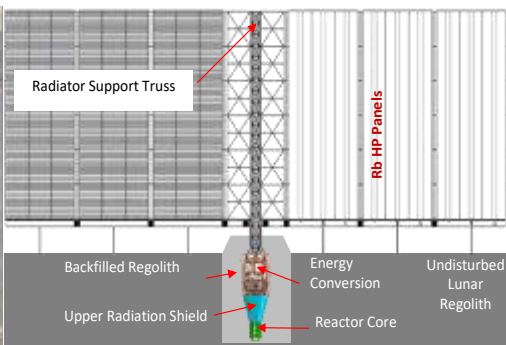
(a) LANL/NASA FPSE Affordable Fission Surface Power System 55 kW_e [Ref. 8]



(b) NASA Prometheus CBC Fission Surface Power System 50 kW_e [Ref. 14]



(c) SP-100 CBC Lunar Power System 550 kW_e [Ref. 11]



(d) UNM-ISNPS SCoRe TE Lunar Power System 50 kW_e [Ref. 5]

Figure 2: Conceptual layout of heat pipe heat rejection radiators of select nuclear reactor systems with TE and CBC energy conversion for lunar surface power.

The thermal efficiency of the nuclear reactor power systems with Free Piston Stirling Engine (FPSE) and Closed Brayton Cycle (CBC) energy conversion could be 20% -30%, however, the surface average temperature of the waste heat rejection radiators will be quite low, ranging from 400 – 500 K. These radiators typically use water heat pipes to spread the waste heat along the surface. Conversely, with static energy conversion such as Thermolectric (TE) and Thermionic (TI) the thermal efficiency of the system is low, < 10% but the radiator average surface temperatures are much higher ranging from 700 – 800 K [3-6]. At these temperatures alkali metals heat pipes are used to spread waste heat along the radiator surface (Tables 1, 2). Nuclear reactor power systems with Alkali Metal Thermal-to-Electric (AMTEC) static energy conversion [7, 18] with thermal efficiency of 20-30% operate at the highest fraction of Carnot compared all static and dynamic energy conversion options and reject the waste heat at 650 K.

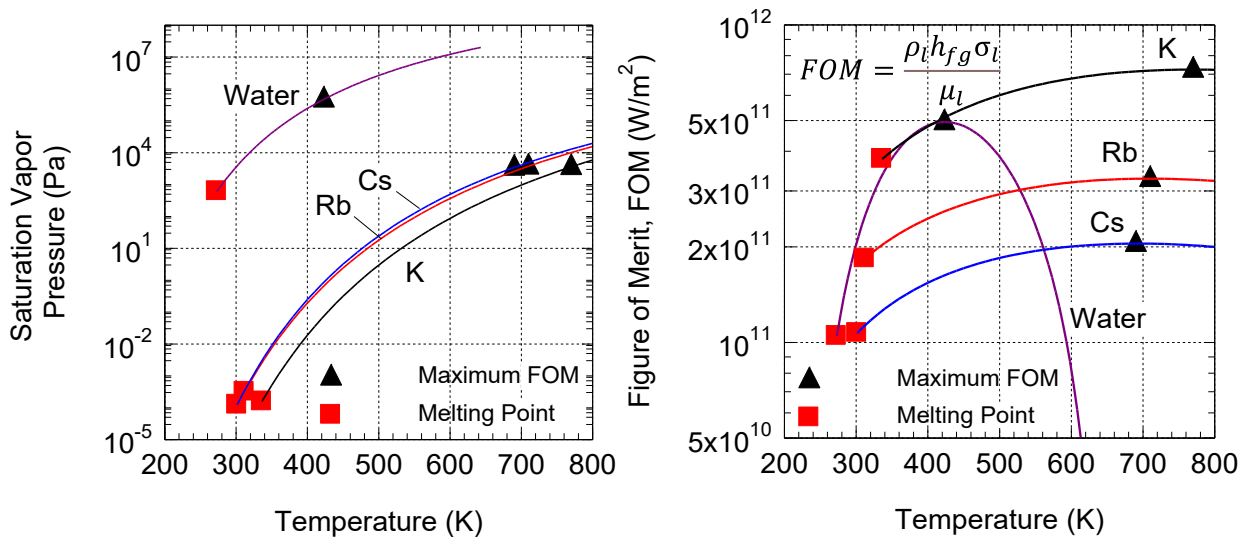


Figure 3: Comparisons of the saturation vapor pressures and Figure of Merit (FOM) curves of candidate heat pipe working fluids as function of operating temperature [24].

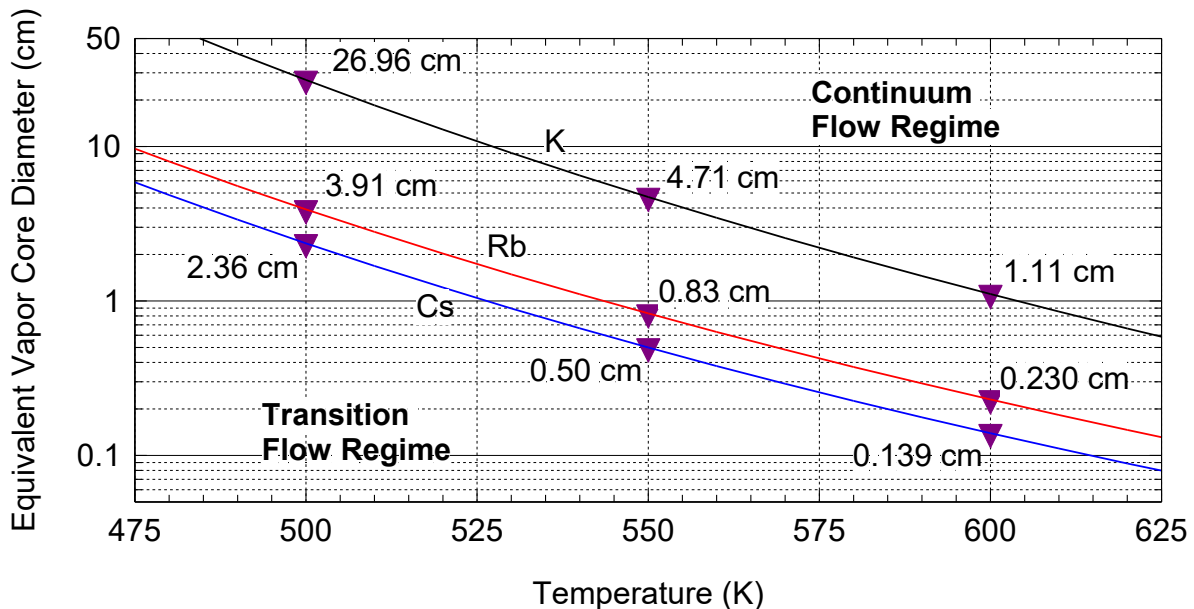


Figure 4: Heat pipe equivalent diameters for operating in continuum and transition flow regimes of Cs, Rb, and K working fluids versus temperature [24].

The reported estimates of the areal density, or the mass per unit projected area, of the heat rejection radiators for nuclear reactor power system with different energy conversion options and for space exploration and lunar surface power ranges from 5.24 to 12.76 kg/m² (Table 2) [4-17]. However, a desirable objective by NASA is to develop lighter radiator designs with areal density ≤ 3 kg/m² for waste heat rejection into space at a surface average temperature of 600 K [19], which is the focus of the present work.

At this temperature, Cesium (Cs) is the most suitable heat pipe working fluid in terms of the Figure-of-Merit and its larger design margin from the prevailing operation limit (Figs. 3 and 4) [20]. The working fluid figure of merit (FOM), defined as $\sigma_L \rho_L h_{fg} / \mu_L$, where σ_L is the liquid surface tension, ρ_L the liquid density, h_{fg} is the liquid latent heat of vaporization, and μ_L is the liquid viscosity (Fig. 3). The performance of a heat pipe is highest at or near the temperature corresponding to the maximum FOM of the working fluid (Fig. 3). The FOM curves for the alkali metals are flat near their maximum values which allow their use for wide range of temperatures near the maximum FOM, with only a slight decrease in performance. Alkali metals heat pipes also have the advantage of only needing thin walls because of their low vapor pressures (Fig. 3), which translate into lower areal density.

Table 1: Comparison of reported operation parameters of selected nuclear reactor systems with static and dynamic energy conversion for space exploration and lunar surface power [2, 4-17].

Nuclear Reactor Power System	Rx Power (kW _{th})	Energy Conversion	System Thermal Efficiency (%)	System Power (kW _e)	Energy Transport (Primary/ Secondary)	Ref.
Thermoelectric (TI) Conversion						
SP-100	2400	SiGe TE	4.58	110	Li / Li	4
SCoRe-TE	2893	SiGe TE	4.3	124	Li / Li	5
HP-STMC	1641	Segmented TE	11.8	194	Li HP / none	6
Alkali Metals Thermal-to-Electric Conversion (AMTEC)						
SAIRS-A	488	Na	22.7	111	Na HP / K HP	7
SAIRS-B	412	Na	26.9	111	Na HP / K HP	7
SAIRS-C	407	Na	27.3	111	Na HP / K HP	7
Free Piston Stirling Engine (FPSE) Conversion						
*AFSPS	175	FPSE	31.4	55	NaK-78 / Water	8
Kilopower	4	FPSE	25	1	Na HP / none	9
*HOMER-15	11.5	FPSE	26	3	Na HP / none	10
*Kilopower Surface Power	43	FPSE	23.3	10	Na HP / none	2, 9
*SP-100 FPSE	455	FPSE	22	100	Li / NaK-78	11
Closed Brayton Cycle (CBC) Conversion						
JIMO	900	CBC	23.1	208	He-Xe / Water	12, 13
*Prometheus FSPS	222	CBC	25.4	56	He-Xe / Water	14
S ⁴ -CBC	471	CBC	31.2	147	He-Xe / NaK-78	15, 16
SAFE	473	CBC	21.1	100	He-Xe / NaK-78	17
*SP-100 CBC	464	CBC	21.6	100	Li / He / NaK-78	11

*Lunar surface power

Although the FOM for Cs is lower than for Rb or K in the 500 – 600 K temperature range of interest, its higher vapor pressure reduces the vapor flow diameter for the heat pipe to operate in the continuum flow regime for effective thermal power transport (Figs. 3 and 4). For these working fluids and temperatures, the heat pipe operation is typically sonic limited because of the low vapor densities. The vapor pressure for Cs is slightly higher than those of rubidium (Rb) and potassium (K). The vapor cross-section area for continuum flow is the smallest for a Cs heat pipe and decreases exponentially with increased heat pipe evaporator temperature. At an evaporator temperature of 600 K, the heat pipe equivalent diameter for continuum vapor flow in the Cs heat pipe is only 13.9 mm compared to 23.0 mm and 111.0 mm with Rb and K working fluids, respectively (Fig. 4).

Table 2: Operation parameters of HP heat rejection radiators for nuclear reactor systems with static and dynamic energy conversion for space exploration and lunar surface power. [2,4-17]

Power System	HP Working Fluid	Surface Area (m ²)	Rejected Power (kW)	Surface Av. Temp. T _s (K)	Sp. Power (kW/m ²)	Areal Density (kg/m ²)	Sp. Mass (kW/kg)	Effective Emissivity ε	Ref.
Thermoelectric (TE) Conversion									
SP-100	K	107	2290	791	21.40	8.00	2.68	0.85	4
S _{CoRe} -TE	Rb	169	2566	780	15.18	6.82	2.23	0.85	5
HP-STMC	K	47.1	1449	756	30.76	11.80	2.61	0.85	6
Alkali Metal Thermal-to-Electric Conversion (AMTEC)									
SAIRS-A	K	29.3	377	662.3	12.87	12.76	1.01	0.85	7
SAIRS-B	K	23.2	301	662.8	12.98	11.90	1.09	0.85	7
SAIRS-C	K	23.05	296	661.9	12.84	11.71	1.10	0.85	7
Free Piston Stirling Engines (FPSEs) Conversion									
*AFSPS	Water	175	120	385	0.69	7.00	0.10	0.86	8
Kilopower	Water	2.3	3	400	1.30	5.24	0.25	0.86	9
*HOMER-15	Ammonia	7.58	8.51	400	1.12	9.50	0.12	-	10
*Kilopower	Water	20	33	400	1.65	5.24	0.31	0.86	2,9
*SP-100 FPSE	K	41	355	665	8.66	11.59	0.75	-	11
Closed Brayton Cycle (CBC) Conversion									
JIMO	Water	590	422	447	0.72	7.16	0.10	0.86	12, 13
*Prometheus-FSPS	Water	131	154	443	1.18	5.89	0.20	0.9	14
S ⁴	Water	169	324	463	1.92	5.88	0.33	0.85	15, 16
SAFE	Water	216	373	440	1.73	6.00	0.29	-	17
*SP-100 CBC	Water	93	364	527	3.91	8.82	0.44	-	11

*Lunar surface power

Tables 1 and 2 compare the reported performance parameters of some conceptual designs of nuclear reactor power systems with static and dynamic energy conversion and heat pipe radiators for waste heat rejection at different temperatures [2,4-17]. Most radiator designs assume a surface average emissivity of 0.85 - 0.9 and use either water or potassium heat pipes to spread the dissipated waste heat along the surface of the radiator. Waste heat rejection radiators on the lunar surface employ vertically erected heat pipe panels to reduce the

accumulation of the lunar dust, potentially decreasing the surface emissions for the radiative rejection of the waste.

On the lunar surface, the nuclear reactors and the shadow shields are placed below grade and surrounded by lunar regolith for radiation shielding. The lunar regolith has also been shown to be an effective supplemental neutron reflector for increasing the reactor operation life and reducing the launch mass and cost of the system to the lunar surface [21]. This placement is suitable for safe end-of-life temporary storage of the nuclear reactor until the radioactivity of the accumulated fission products in the reactor core drops to an acceptable level for safe handling and recovery of nuclear reactors with spent nuclear fuel [22].

As shown in Fig. 1, nuclear reactor power systems for space exploration missions have either conical or flat heat pipe radiator panels erected within the solid angle of the radiation shadow shield. The residual heat from the energy conversion subsystem is transported by the circulating fluid in the secondary loops of water, alkali metal sodium-potassium eutectic (NaK-78), or lithium to the heat pipe radiator panels (Table 1) [4,5,8,11,12-17].

The SP-100 Generic Flight System with SiGe TE energy conversion circulates liquid lithium for cooling the nuclear reactor and transporting the thermal power to the TE elements. The circulating liquid lithium in the secondary loops removes the waste heat rejected by the TE elements and transports it to the potassium heat pipe in the radiator panels, which radiatively rejects the waste heat into space at a surface average temperature of 791 K (Fig. 1a) [4]. Thermoelectric Electromagnetic DC (TE-EM) pumps passively circulate the liquid lithium working fluids in the primary and the secondary loops.

The nuclear reactor power system for the Prometheus Jupiter Icy Moons Orbiter (JIMO) uses CBC energy conversion units and rejects waste heat into space using water heat pipe radiator panels at a surface average temperature of 447 K (Fig. 1b) [12,13]. The Scalable AMTEC Integrated Reactor space power System (SAIRS) developed at the University of New Mexico's Institute for Space and Nuclear Power Studies (UNM-ISNPS) operates fully passive. It uses sodium heat pipes to transport the reactor thermal power to arrays of AMTEC energy conversion units, which reject the waste heat into space using potassium heat pipes radiator panels (Fig. 1c) [7,18]. The Kilopower space nuclear power system developed at Los Alamos National Laboratory removes the waste heat from multiple FPSE units using water heat pipes for heat rejection into space (Fig. 1d) [9]. The Affordable Fission Surface Power System (AFSPS) concept uses FPSE energy conversion and rejects residual heat using two foldable wings of rectangular water heat pipe radiator panels thermally coupled to a secondary pumped water loop (Fig. 2a) [8]. The Prometheus Lunar Fission Surface Power System (FSPS) uses CBC energy conversion and rejects waste heat into space using water heat pipe radiator panels coupled to a pumped secondary water loop (Fig. 2b) [14].

A lunar surface power SP-100 reactor is coupled to multiple helium CBC energy conversion units and features water heat pipes rectangular radiator panels erected vertically around the reactor like spokes [11]. Tertiary liquid sodium-potassium eutectic (NaK-78) loops transport the residual heat from the gas cooler in the CBC helium loop to water heat pipes radiator panels (Fig. 2c). The Sectored Compact Reactor lunar surface power system (SCoRe-TE) uses SiGe TE energy conversion and vertically erected rubidium (Rb) heat pipe radiator panels for waste heat rejection (Fig. 2d) [5]. The Rb heat pipe radiator panels are hydraulically coupled in parallel to a pumped NaK-78 heat rejection loop for the avoidance of a single point failure.

The heat pipes radiator panels of nuclear reactor power systems for space exploration and planetary surface power are preferably connected hydraulically in parallel. This enhances performance, reliability, decreases specific mass and avoids single point failures in operation [22]. In addition, the exposed radiator surfaces would be armored to protect against impacts by micrometeors and space debris. The black coated surface of the radiator panels can achieve an emissivity of 0.8 - 0.9 (Table 2) [4-9,13,16].

16. Research Objectives and Summary of Accomplishments

Decreasing the mass of waste heat rejection radiators decreases the total launch mass and cost for future fission reactor systems for space exploration and planetary surface power. State of the Art (SOA) radiator designs for fission surface power systems have estimated areal densities from 5.24 – 12.76 kg/m² (Table 2) [4-17]. The outlined design goals in the NASA 21-ESI award, which is the focus of the present work, are to develop an advanced, lightweight heat pipe radiator, much lighter than current State-of-the-Art (SOA) with areal density ≤ 3.0 kg/m² and for rejecting waste heat into space on the lunar surface at a radiator surface average temperature of 500 - 600 K for up to 10 years (Table 3) [19].

In addition, the advanced radiator panels should operate both in microgravity and in low gravity environments, such as on the surface of the Moon, be sufficiently strong to survive launch vibration loads and survive space environmental hazards including micrometeoroids, atomic oxygen erosion, energetic ionizing solar radiation, and high energy gamma and neutrons emanated from nuclear reactor.

The research effort performed at the University of New Mexico's Institute for Space and Nuclear Power Studies (UNM-ISNPS): (a) selected an appropriate working fluid of the Cs-Ti heat pipes and structure material of the heat spreading fins, (b) performed thermal and structural modeling and simulation analyses to optimized the design of an advanced lightweight heat pipes radiator panel concept with ten heat pipe modules, (c) Characterized the bonding at the interfaces for the composite structures of radiator modules, (d) performed impact analysis for armoring the radiator surface with C-C composite, and (e) performed stress and vibration analysis of a radiator panel comprising ten heat pipes radiator modules during launch on board of two different heavy launch vehicles.

Table 3. NASA operation requirements for developing a lightweight heat rejection radiator.

• Nominal heat rejection temperatures:	500-600 K
• Integrated radiator aerial density including all major components:	≤ 3 kg/m ²
• Operate in microgravity, low gravity, and high thrust environments.	
• Operation service life:	≥ 10 years.
• Modular, deployable, and capable of surviving vibration loading during launch, landing, and deployment.	
• Survive environmental hazards such as micrometeoroid impacts, solar UV radiation, ionizing radiation from the nuclear reactor, and atomic oxygen erosion in Earth orbit.	

During the first two years of the project, we developed preliminary designs for the heat pipe radiator panel to achieve the project objective areal density of ≤ 3.0 kg/m². The developed Versions 1-6 heat pipe radiator designs progressively improved the performance and reduced the areal density of the lightweight heat pipe radiator modules [19,23-27]. The results for these years are detailed in the project's previous two annual reports [20, 23].

At the end of the 2nd year, the integrated radiator panel with six Version 6 (Ver. 6) heat pipe modules has an estimated areal density near the target of ≤ 3.0 kg/m². The research effort for the final year of the project aims to improve the heat pipe radiator modules' design to further decrease the areal density of the integrated radiator panel. The 2nd year report details the analysis for the Ver 4-6 heat pipe radiator modules [23]. The performed analyses for the Ver. 7 and 8 heat pipe module concepts estimate the performance, mass and areal density of the integrated radiator panel to determine if either design option can reduce the areal density to ≤ 3.0 kg/m². The performed analyses with the Heat Pipe Transient Analysis Model (HPTrAMTM) are thermally coupled with the STAR-CCM+ commercial multiphysics code to determine the

heat pipe operation limit and the length of the condenser, L_{cd} , for an average surface temperature of heat rejection $T_s = 600$ K.

The micrometeoroid armor analysis calculates the thicknesses of the C-C composite armor for the Cs-Ti heat pipe and the 10 cm wide composite fins of Highly Oriented Pyrolytic Graphite/Titanium (HOPG/Ti). The analyses estimate the perforation probability for the heat pipe wall and the penetration probability for the heat spreading fins for 10 years' service on the Moon for 1 g/cm^3 incident particles on the lunar surface. The next section presents results of the heat pipe performance and 3-D thermal analyses for the Ver. 7 and 8 heat pipe radiator modules. This effort:

- (1) improved the thermal coupling of the flowing NaK-78 duct to the HP's evaporator section and performed 3-D Computational Fluid Dynamics (CFD) thermal analyses of the integrated radiator panel [23,24],
- (2) performed micrometeoroid protection analyses to determine the thickness and mass of the C-C composite armors of the Cs heat pipes and of the HOPG/Ti heat spreading fins for protection against micrometeoroids on the lunar surface [23,27], and
- (3) performed Finite Element solid stress Analysis (FEA) of the developed heat pipe radiator module and an integrated radiator panel of ten modules to estimate the induced stresses due to vibrations experienced during launch.

The UNM-ISNPS' research accomplishments during this three-year research award [19,23-27]:

- Showed that HOPG layers, encased in Ti, in the heat spreading fins are effective in spreading the rejected waste heat radiatively rejected into space, and decreasing the areal density and increasing the power density of the radiator panel. Adding HOPG fillets has been shown to enhance the thermal conduction coupling of the heat pipes to the HOPG/Ti heat spreading fins by decreasing the thickness of the HOPG layer in the fins. They also help enhance the structural rigidity of the radiator panels but slightly increase the areal density of the radiator model [20].
- Identified that for operating at average surface temperatures for heat rejection of 600 K, the Cs and Rb heat pipe working fluids as the only viable choices. However, Cs is preferable based on the lower temperature and equivalent heat pipe diameter needed to operate in the continuum flow regime. In addition, the lower Cs vapor pressure needs thinner Ti heat pipe wall, hence decreasing the areal density of the radiator [20, 24].
- Performed analyses using a lumped parameter model to investigate the effects on heat pipe power throughput, and the areal density, dimensions, and specific power of the radiator module of the following parameters, namely: (a) the width and length of the HOPG/Ti heat spreading fins (the length of the fins equals that of the condenser of the Cs heat pipes in the modular); the equivalent diameter or the flow area of the Cs vapor in the heat pipes; (c) the inlet temperature of the NaK-78 in the header flow duct thermally conductively coupled to the evaporator section of the heat pipes, and (d) the average surface temperature for waste heat rejection into space [20].
- Performed 3-D CFD analyses of a heat pipe radiator module that effectively identified needed improvements to enhance thermal conduction coupling of the Cs heat pipes to the HOPG/Ti heat spreading fins. The addition of HOPG fillets helps decrease the thickness of the HOPG layer in the heat spreading fins and the overall areal density of the heat pipe radiator module [20].

- Used a comprehensive HPT_{RAM}TM that existed at the UNM-ISNPS to investigate the performance of the Cs-Ti heat pipes in the radiator modules. This includes the operation limits of the heat pipe and that prevailing at the desired surface average temperature of 600 K for heat rejection into space, the axial distributions of the Cs vapor and liquid pressures, and the power throughput. Also investigated is the effect of changing the dimensions and design of the liquid NaK-78 flow duct thermally coupled to the evaporator section of the Cs-Ti heat pipes on the HP power throughput and heat rejection power, the module/heat pipe condenser total length, the 2-D spatial distribution of surface temperature for waste heat rejection into space. These investigations employed HPT_{RAM}TM coupled to the STAR-CCM+ commercial code to perform 3-D thermal analysis of the Cs-Ti HP modules and size the HP condenser length for operating at a surface average temperature, $T_s = 600$ K [23,24].
- Developed seven designs of Cs-Ti heat pipe radiator modules with 10 cm wide HOPG/Ti heat spreading fins for waste heat rejection into space at $T_s = 600$. Versions 5, 6, and 7 design of the modules with increasingly lower areal density systematically and gradually reduced the Cs vapor flow area in the titanium-Cs heat pipes by 30%, 50%, and 70%, compared to that of the Ver. 4 design [24].
- Performed detailed analyses for armoring the Cs-Ti heat pipe and the HOPG/Ti heat spreading fins in the radiator modules using C-C composite against impact by micrometeoroid particles having densities of 1.0 and 2.5 g/cm³. Results determined the thicknesses of the C-C composite armors to protect the Cs-Ti heat pipes and the HOPG/Ti fins for > 10-year service life of vertically erected radiator panel on the lunar surface. The C-C armor thickness for the lightest Ver. 7 Cs-Ti heat pipe is 0.58 mm for 10% perforation probability over the 10-year life. For 10% penetration probability of the heat spreading fins the C-C armor is ≤ 0.2 mm thick [23,27].
- Successfully Characterized the Ti-HOPG interface using SEM/FIB and TEM methods. Performed experiments to demonstrate the soundness of the bonding at the interfaces between the Ti casing in the heat spreading fins with both the HOPG and the C-C composite armor. Magnetron sputtering of Ti on graphite and C-C specimens has been effective in producing continuous 1-2 μm thick Ti layers. These layers are deposited onto the surface of the HOPG sample using magnetron sputtering and the sample is outgassed in ambient temperature in hard vacuum for extended period (~2-1.5x10⁻⁷ torr) at UNM-ISNPS. Results show clean and continuous interface between the Ti and HOPG layers without formation of carbides [20,23].
- Performed stress and vibration analyses (FEA) for the lightest Ver. 7 heat pipe radiator module and an assembled panel of 10 modules with the STAR-CCM+ Multiphysics commercial code [28]. The analyses for the Ver. 7 heat pipes module simulate the lateral 5-100 Hz frequency vibration loads for both the Falcon Heavy and Delta IV Heavy launch vehicles. The solid stress analysis for the heat pipe module shows that the maximum displacement occurs at 100 Hz frequency with the calculated stress below the failure limit for the Ti alloy wall and HOPG fins. FEA analysis for the 10-module panel for the vibration loads of the Falcon Heavy launch vehicle shows that the highest displacement is for a frequency of 25 Hz. The calculated peak stresses for the Ti alloy walls of the Cs HPs and the NaK-78 ducts and HOPG fins are all below the failure stress limits for the materials.

- Demonstrated that the estimated areal density for an integrated radiator panel comprised of ten, Ver. 7 HP modules, which are hydraulically connected in parallel, is 2.97 kg/m^2 , which is consistent with NASA's target of $< 3 \text{ kg/m}^2$ [24].

Section 3 below describes the designs of the improved heat pipe radiator modules and the panel. Section 4 presents the results of the heat pipe performance and CFD thermal analyses of the improved designs of the heat pipe radiator modules. Section 5 presents the results of the micrometeoroid protection analysis to determine the armor thicknesses of the Cs-Ti heat pipes and the HOPG/Ti heat spreading fins for ten years' service on the lunar surface as function of the heat pipe perforation probability and the perforation probability of the fins. Section 6 describes the performed FEA structural simulations of the panel of ten lightest radiator modules (Ver. 7) subject to the launch vibration acceleration loads for two heavy lift launch vehicles. Finally, Section 7 presents the estimates of the areal density and performance for the improved advanced designs of the lightweight radiator panel and modules.

17. Lightweight Heat Pipe Radiator Design Concepts

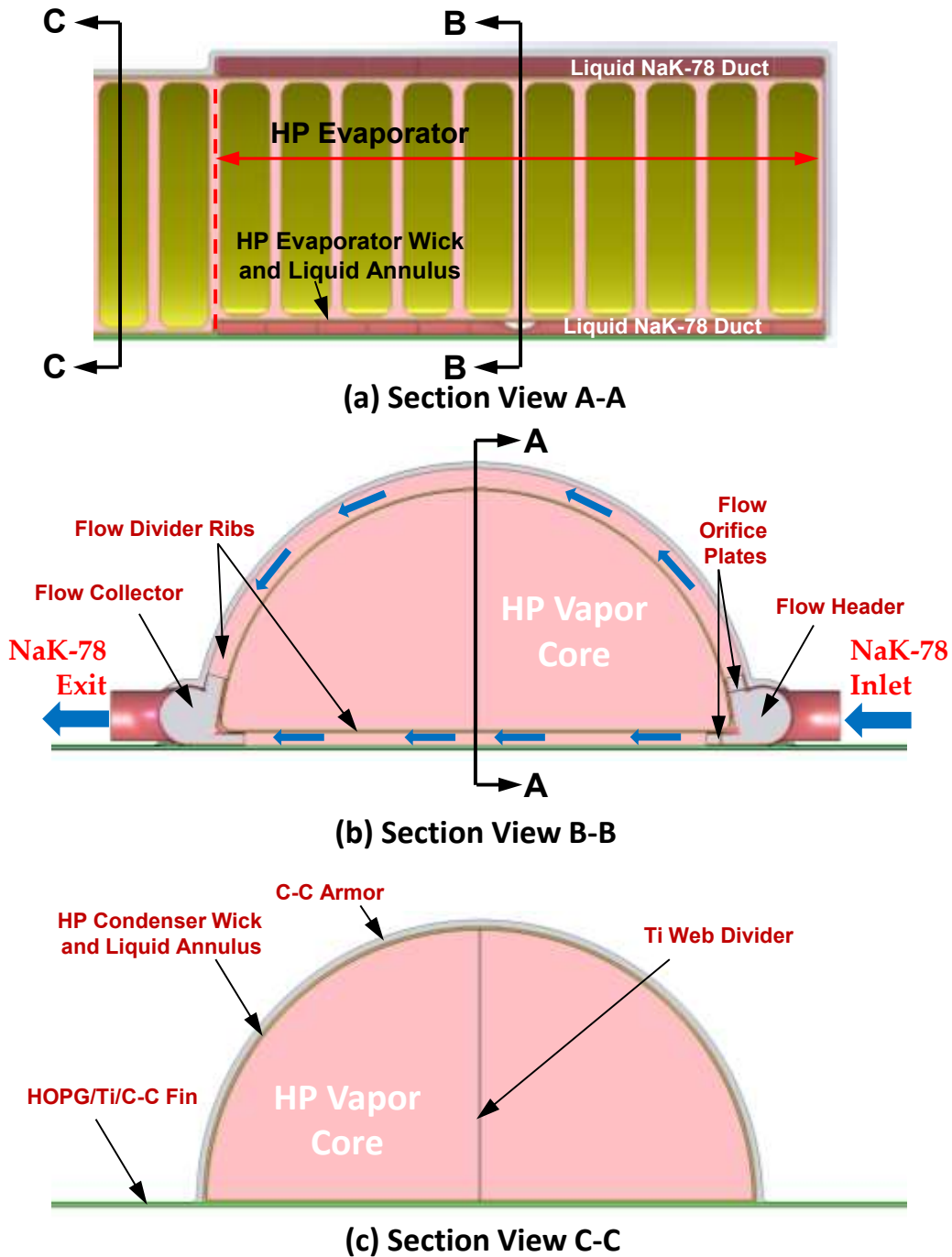


Figure 5. Section views of the evaporator and condenser of the Version 4 heat pipe module with redesigned NaK-78 flow duct [24].

The Version 4 (Ver. 4) heat pipe radiator module developed during the 2nd year of the project has improved performance over the previous designs (Fig. 5) [23,24,26]. The cross section of the Cs-Ti heat pipe in the radiator module is semi-cylindrical on top and with a flat bottom, for structural strength and good conductive coupling of the heat pipe wall to the

HOPG/Ti heat spreading fins (Fig. 5b-c). The Ti wall of the heat pipe is 0.2 mm thick, and the porous sintered Ti wick is 0.1 mm thick, and the Ti walls of the HOPG/Ti fins are 0.1 mm thick. The HOPG has high in-plane thermal conductivity of 1,800 - 2,000 W/m-K for efficiently spreading heat along the fins and a low off-plane thermal conductivity of 8 W/m-K [30]. The Ti divider in the heat pipe (Fig. 5a, c) structurally supports the thin Ti wall and helps accommodate acoustic vibrations during launch.

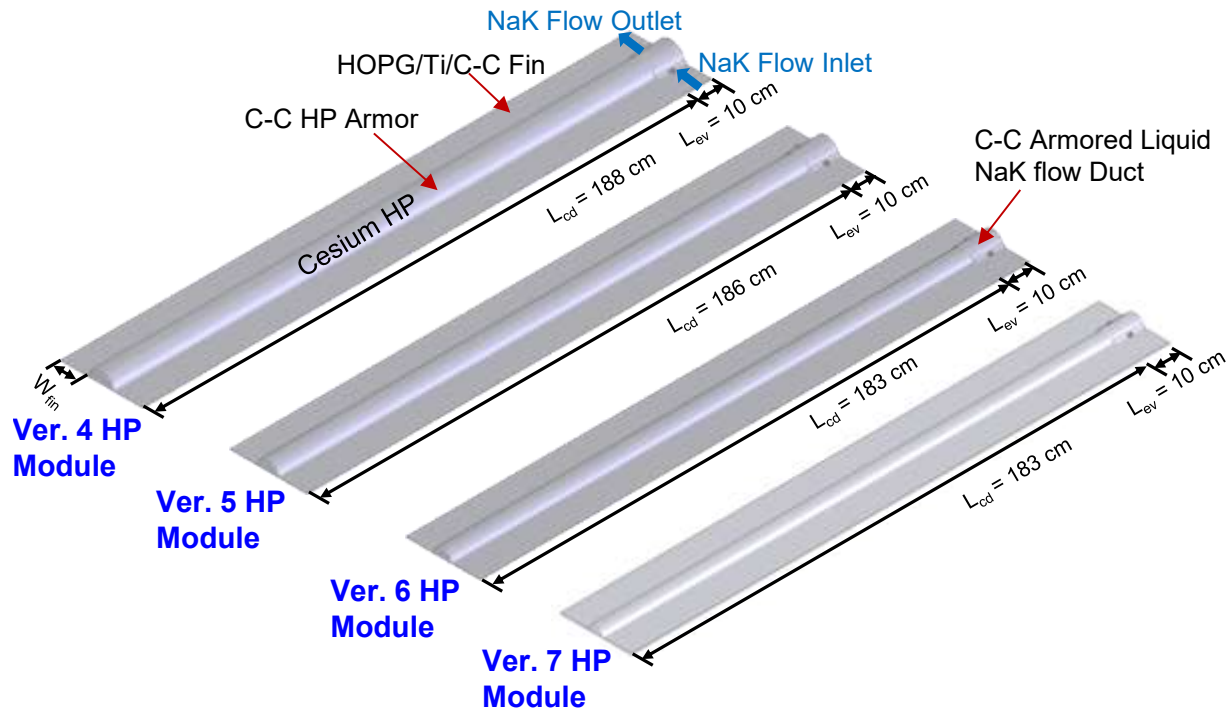


Figure 6: Developed lightweight Cs-Ti heat pipe radiator modules armored C-C composite fibers and with 10 cm wide HOPG/Ti heat spreading fins for rejecting waste heat at surface average temperature of 600 K into space [24].

The thin liquid annulus between the sintered Ti wick and the Ti heat pipe wall decreases the friction pressure losses of the returning liquid Cs from the condenser section to the evaporator section of the heat pipe. This raises the wicking limit of the heat pipe for heat rejection at a surface average temperature of 600 K. The Cs-Ti heat pipe in the radiator module is conductively coupled to the lightweight HOPG/Ti heat spreading fins, each comprised of a layer of HOPG encased in thin Ti. The width of the HOPG/Ti fins, W_{fin} , is 10 cm along the heat pipe (Figs. 6 and 7).

The exposed surfaces of the heat spreading fins and the Cs-Ti heat pipe are armored with thin layers of C-C composite to protect against impacts by micrometeoroids and space debris. The C-C composite armor also protects the liquid NaK-78 flow duct surrounding the evaporator section of the Cs-Ti heat pipe. The waste heat removed from the nuclear reactor power system is transported to the heat pipe radiator panels by circulating liquid NaK-78 through ducts which are conductively coupled to the evaporator section of the Cs-Ti heat pipe in the radiator module (Fig. 5a and b). The liquid NaK-78 flow duct (Fig. 8) wrapped around the evaporator section of the Cs-Ti heat pipe, increases the interfacial area for heat transfer from the flowing NaK-78 in the duct to the heat pipe evaporator section, and hence the heat pipe power throughput.

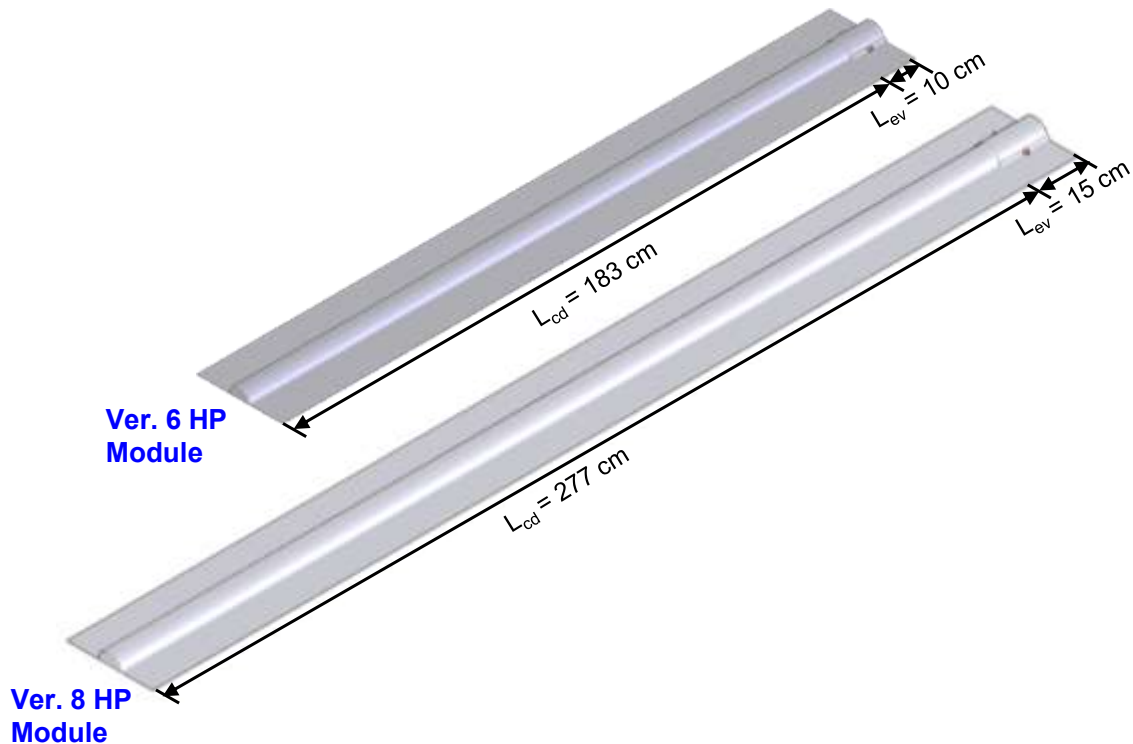


Figure 7: Developed designs of Ver. 6 and Ver. 8 lightweight Cs-Ti heat pipe radiator modules with 10 cm wide HOPG/Ti heat spreading fins.

3.1. NaK-78 flow duct design and thermal analysis

Figure 8a shows an isometric 3-D view of the NaK-78 flow duct and the cross-section view in Fig. 5b shows the interior details of the duct design. The liquid NaK-78 coolant enters the flow duct from a cylindrical-shaped header running along the base of the evaporator. The entering liquid splits into two flow paths; an upper path along the curved hemi-cylindrical surface of the heat pipe evaporator, and a second path along the flat bottom surface of the heat pipe evaporator, which is conductively coupled to the HOPG/Ti heat spreading fins.

The liquid NaK-78 flows through circular orifices at the entrance to the upper and lower flow paths to laterally distribute the flow uniformly (Fig. 5a and b, 8b). The added ribs along the width of the flow duct provide structural support and guide the NaK-78 flow within the upper and bottom flow paths of the heat pipe evaporator duct. The liquid NaK-78 exits the duct to a cylindrical header before returning to the secondary loop of the nuclear reactor power system. This loop transports the residual thermal power from the energy conversion subsystem to the heat rejection radiator panels.

The performance analyses of the Cs-Ti heat pipe in the Ver. 4 design of the heat rejection radiator module used the 2-D HPTTrAM™. Results show that the Cs-Ti heat pipe in this module operates far from the sonic limit. Therefore, the vapor flow cross-section area in the Cs-Ti heat pipe can be decreased with little or no effect on performance or power throughput. This is investigated in subsequent designs, Versions 5 – 7 of the radiator modules. The Ver. 5 heat pipe module is like Ver. 4, but the diameter of the Cs heat pipe decreased from 8.73 cm to 7.34 cm. Consequently, the Cs vapor flow area in the Cs-Ti heat pipe decreased by 30%. The Ver. 6 design of the Cs-Ti heat pipe module decreased the heat pipe diameter to 5.94 cm and the Cs vapor flow area in the heat pipe to 50% of that in Ver. 4.

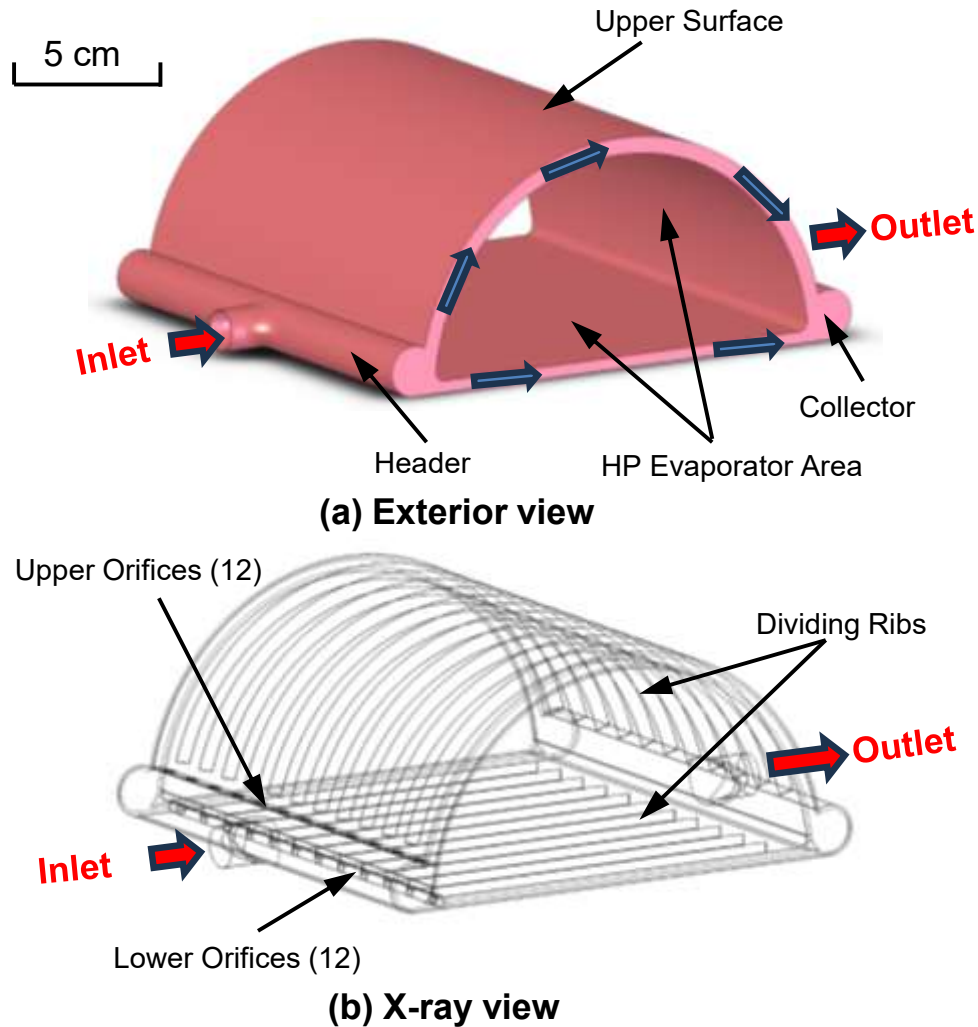


Figure 8. Exterior and x-ray views of the liquid NaK-78 flow duct of the developed Cs-Ti heat pipe module showing the orifice plates and the dividing ribs.

The Ver. 7 design of the heat pipe module further decreased the heat pipe diameter to 4.60 cm, which corresponds to a Cs vapor flow area that is only 30% of that in the Ver. 4 module. Fig. 6 presents Ver. 4, 5, 6, and 7 designs of the Cs-Ti heat pipe radiator modules with the same heat pipe evaporator length, $L_{ev} = 10$ cm. However, the lengths of heat pipe condensers and those of the module, L_{cd} , are sized for operating at the same the surface average temperature for radiative heat rejection, $T_s = 600$ K, and space sink temperature of 250 K [24].

The Ver. 8 design of Cs-Ti heat pipe radiator module design has the same heat pipe diameter as the Ver. 6 module, but the length of the heat pipe evaporator section is 50% longer for $L_{ev} = 15$ cm (Fig. 7). The longer evaporator increases the heat transfer area for the circulating liquid NaK-78 in the evaporator's flow duct and hence, the heat pipe power throughput, as well as the total length of the module and its areal density and specific power.

3.2 Radiator panel design

The developed Cs-Ti heat pipe radiator modules are assembled into rectangular panels with a metal support frame. The number of assembled modules in the radiator panels can vary from six to ten (Fig. 9), or even more, depending on the stowed volume in the launch vehicle of

choice. The rectangular panels are readily foldable during launch and deployable in a scissor-arrangement on the lunar surface prior to startup of the nuclear reactor power system (Fig. 2a). The parallel hydraulic coupling of the heat pipe modules in the radiator panels ensure that all modules operate at the same power throughput and heat pipe evaporator temperature.

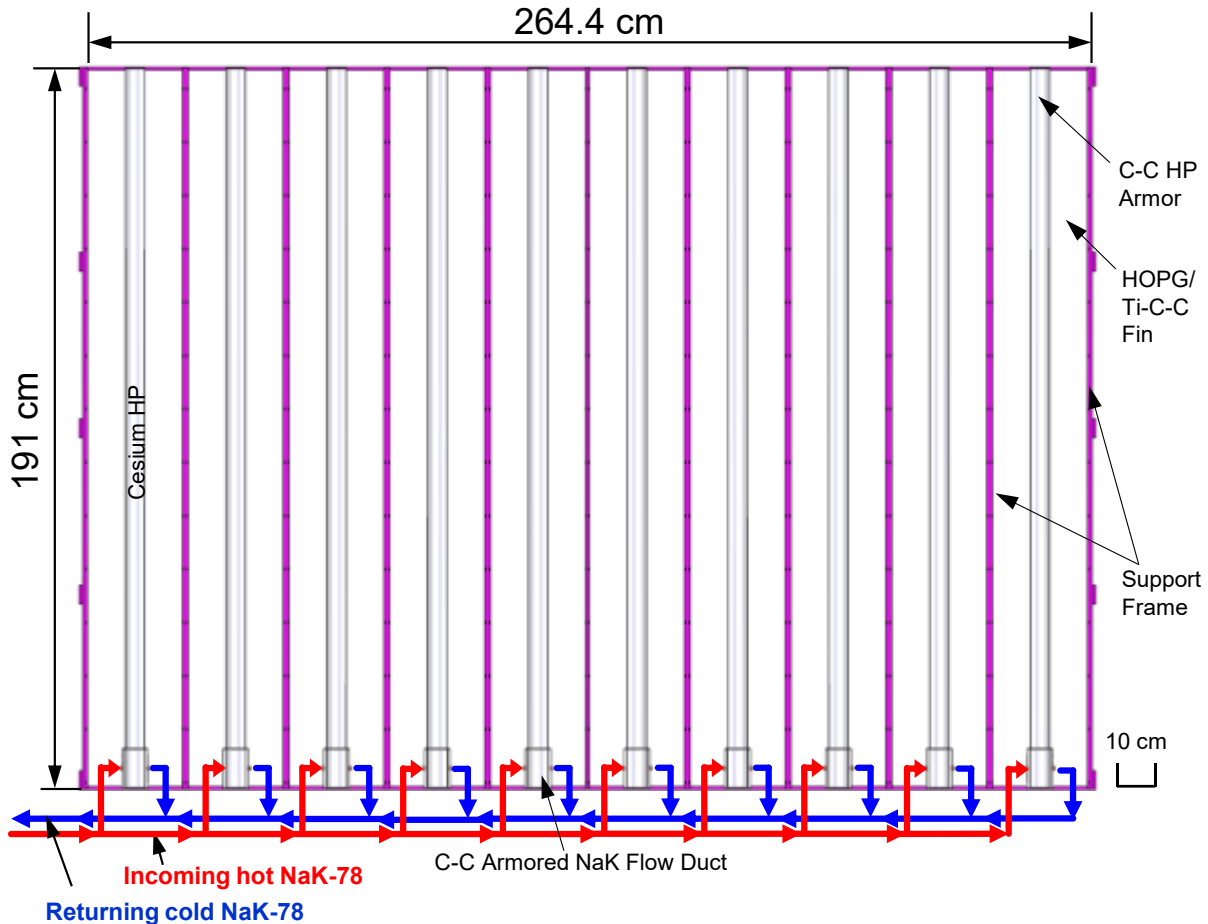


Figure 9: A radiator panel comprised of ten, Ver. 7 Cs-Ti heat pipe modules which are hydraulically coupled in parallel and mounted within aluminum frame for structural support.

On the lunar surface, the radiator panels with the NaK-78 flow ducts will be erected vertically with the condenser sections and the heat spreading fins oriented vertically upwards. This orientation limits the lunar dust accumulation onto the surface of the heat rejection radiator modules which decreases the effective surface emissivity. The vertically mounted radiator panels with the heat pipe evaporator sections lower than the condenser section also enhance heat pipe operation by the lunar gravity assisting the flow of the Cs liquid condensate from the condenser section to the evaporator section of Cs-Ti heat pipes in the radiator panel.

The present performance analyses, however, do not take credit for any performance enhancement due to the Lunar gravity when determining the heat pipes power throughput. Figure 9 presents a rectangular radiator panel with an aluminum frame, enclosing ten Ver. 7 Cs-Ti heat pipe radiator modules. On the lunar surface, the radiator panels with the NaK-78 ducts will be erected vertically near the surface with the condenser sections and the heat spreading fins are erected vertically upwards.

18. Thermal Analysis of Advanced Lightweight Radiator Modular Designs

The design and performance analyses of the advanced designs of the Cs-Ti heat pipe radiator modules couple the 2-D heat pipe performance analysis model HPTrAM™ to 3-D CFD thermal analyses. The Heat Pipe Transient Analyses Model is a steady state and transient 2-D model builds upon the Heat Pipe Transient Analysis Model (HPTAM) developed earlier at the UNM-ISNPS [30-31]. The HPTAM code has been successfully validated for reported experimental results for sodium and lithium heat pipes, including the startup from a frozen state [30-33]. The HPTrAM™ solves the coupled energy, momentum, and mass balance in the liquid and vapor phases and incorporates the momentum and enthalpy jump conditions at the liquid-vapor interface along the porous wick surface within the heat pipe.

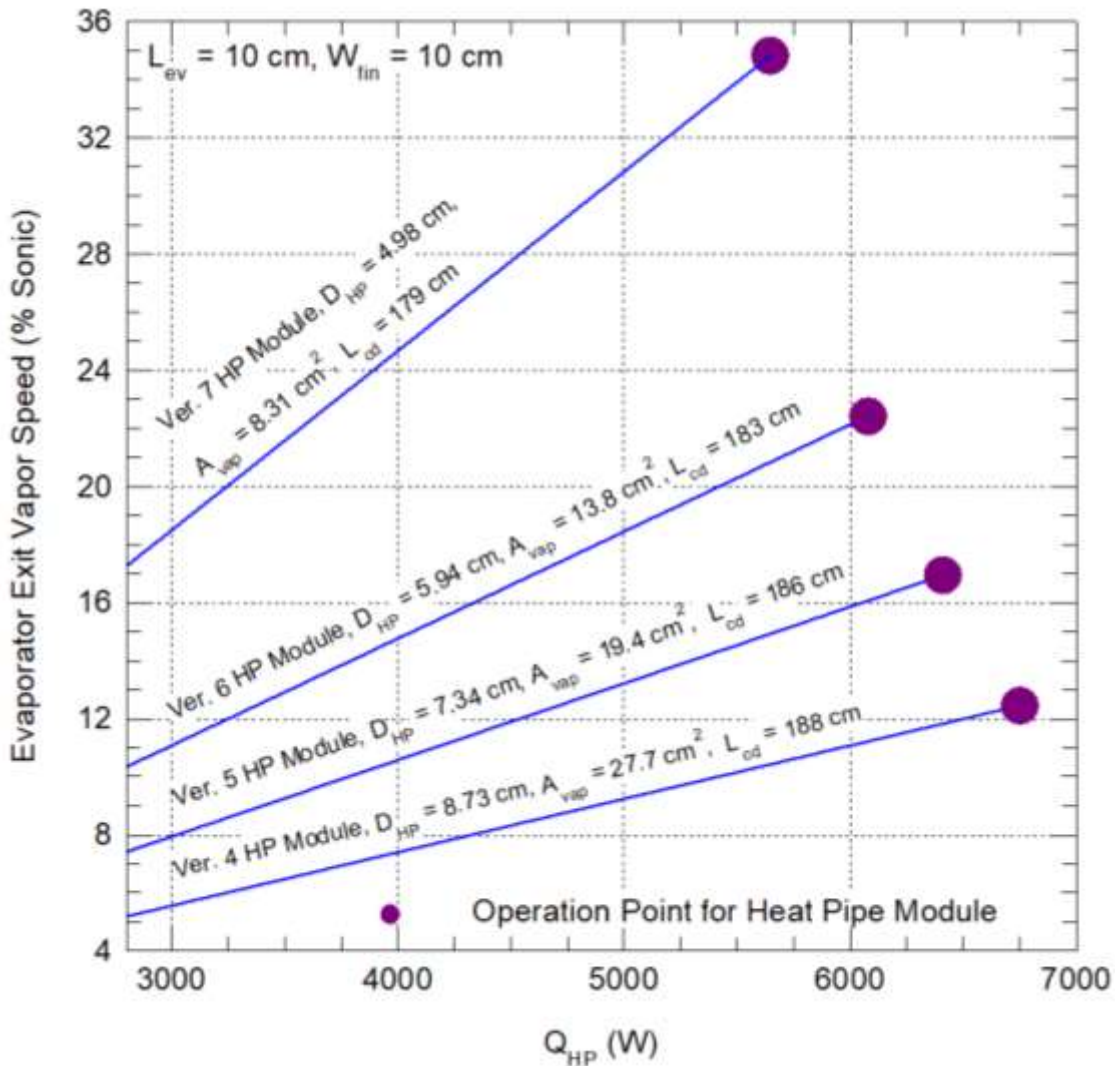


Figure 10: Comparison of the speed of Cs vapor exiting the evaporator sections of the Cs-Ti heat pipes in Versions 4, 5, 6, and 7 radiator modules, with the same evaporator section length, $L_{ev} = 10$ cm and width of heat spreading fins, $W_{fin} = 10$ cm, versus the heat pipe power throughput.

The model divides the heat pipe into four regions: the wall, the liquid annulus, the liquid saturated porous wick, and vapor [24,30]. It calculates the spatial and temporal distributions in the wall, and the temperatures, pressures, and mass fluxes distributions of the liquid (L) and the

vapor (V) along the heat pipe. In addition, it thermally and hydrodynamically couples the liquid and vapor phase and calculates the local radii of curvature of liquid meniscus at the wick-vapor interface. The Ver. 4 heat pipe module has a diameter of 8.73 cm for a vapor flow area of 27.7 cm². The HPT_{RAM}TM simulations of the Ver. 4 modules indicated that the Cs vapor exiting the evaporator section of the heat pipe is a small fraction of the sonic limit (<12.4%). Therefore, the vapor flow area in the heat pipe can be decreased with little or no effect on the power throughput (Fig. 10). The Ver. 5 heat pipe module is like the Ver. 4 design, but the smaller diameter of the Cs-Ti heat pipe of 7.34 cm decreased the Cs vapor flow area by 30%.

The Ver. 6 module design decreased the heat pipe diameter to 5.94 cm, which corresponds to a 50% decrease in the Cs vapor flow area compared to that in the Ver. 4 module. At a power throughput of 6.0 kW, the speed of the Cs vapor exiting the heat pipe evaporator section, which is 11.1% of the sonic speed for the Ver. 4 heat pipe module, increases to 15.8% of the sonic speed for heat pipe in Ver. 5 module, and 22.1% of the sonic speed for the Ver. 6 heat pipe module (Fig. 10). Despite the increased speeds of the Cs vapor exiting the evaporator section of the heat pipes in Ver. 5 and 6 radiator modules, the heat pipes in these modules are not sonic limited.

During the thaw of the heat pipe from a frozen state, HPT_{RAM}TM calculates the volume fractions of working fluid in the annulus and the wick as a function of time. It accounts for the increase in the liquid volume during melting and heating up and its eventual accumulation at the end of the condenser section. The liquid volumes in the interfacial wick computational cells are calculated as functions of the radius of curvature of the liquid meniscus at the liquid-vapor interface and of the radial location of the solid or liquid portions in the wick. Thus, HPT_{RAM}TM can simulate partial liquid recession in the evaporator wick and pooling of excess liquid into the vapor core at the end of the condenser section. This transient heat pipe model identifies, and flags incipience boiling in the evaporator section and drying the wick due to liquid recession.

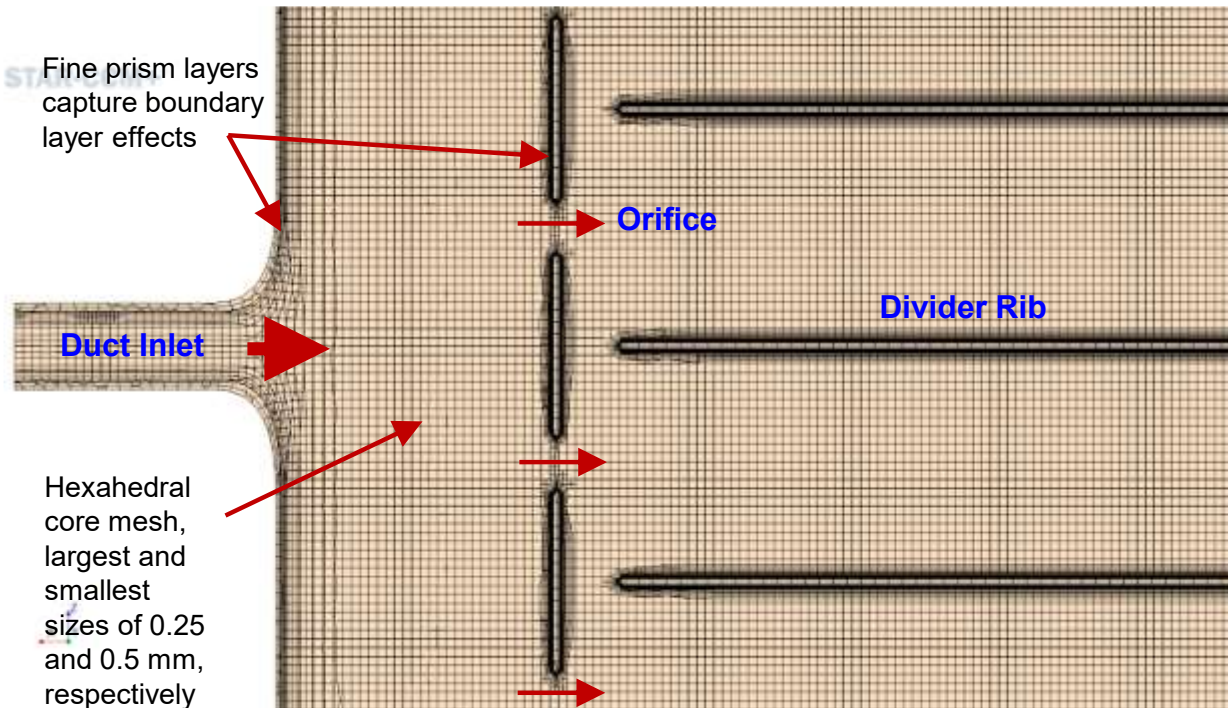


Figure 11: Section view of the computational numerical mesh grid within the straight section of the liquid NaK-78 flow duct [24].

The new Ver. 7 radiator module, (Fig. 6) with Cs vapor cross flow area in the Cs-Ti heat pipe is only 30% of that of the Ver. 4 module, has the highest sonic speed of the Cs vapor existing the evaporator section of the Cs-Ti heat pipe (Fig. 10). At a power throughput of 5.5 kW the speed of the Cs vapor exiting the heat pipe evaporator section in Ver. 7 module is 34.19% of the sonic speed (Fig. 10). The sonic speed for a given power throughput for the latest Ver. 8 heat pipe radiator module with longer evaporator section is the same as that for the Ver. 6 heat pipe module design. This is because both have the same Cs vapor cross section flow area (Figs. 7 and 10).

4.1 3-D CFD thermal analyses of heat pipe radiator modules

The conducted STAR-CCM+ 3-D CFD and thermal analyses of the Ver. 7 and 8 radiator module designs calculated the surface temperature spatial distributions of the radiator modules, including the Cs-Ti heat pipe and the HOPG/Ti/C-C heat spreading fins [24]. They determine the condenser length, L_{cd} , of the Cs-Ti heat pipes in the developed designs of the Vers. 7 and 8 heat pipe modules with 10 cm wide heat spreading fins (Figs. 6 and 7) to operate at $T_s = 600$ K for heat rejection into space. The performed CFD analyses of the heat pipe radiator modules applied the boundary conditions of: (a) constant inlet mass flow rate, (b) constant exit pressure, (3) uniform wall heat flux to the evaporator section of the Cs-Ti heat pipe, (4) radiative heat rejection with a surface emissivity of 0.85 into space, and (5) space sink temperature of 250 K.

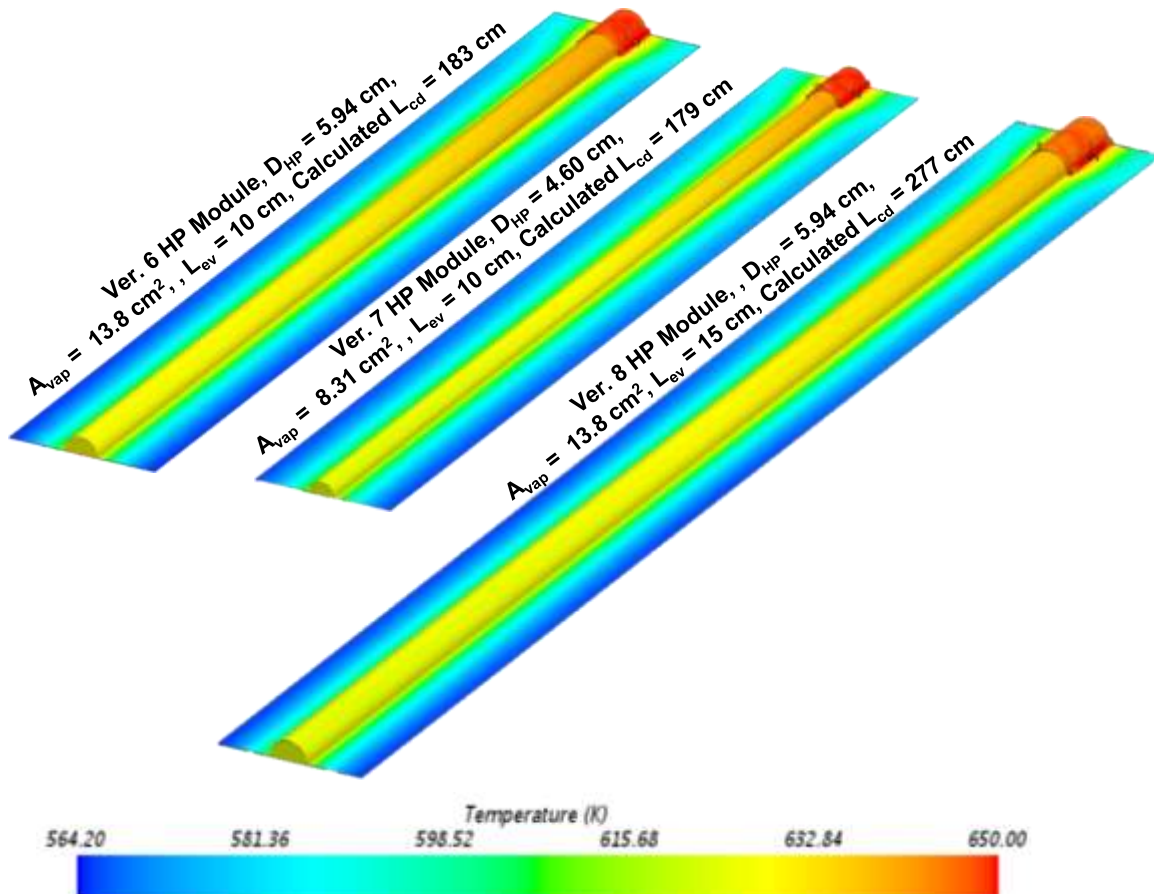


Figure 12: Spatial distributions of the surface temperatures for Ver. 6, 7, and 8 radiator modules for $W_{fin} = 10$ cm, NaK-78 $T_{in} = 650$ K and $\dot{m} = 1.56$ kg/s [24].

Figure 11 shows a section view of the applied numerical mesh grid in the NaK-78 flow duct. The Ti wall of the duct is meshed using the polyhedral mesher with imbedded thin mesher in the STAR-CCM+ code [28]. The numerical mesh cell size varied between 0.05 and 1.5 mm. The thin mesher ensures having at least three prismatic layers across the width of the thin Ti wall. The hexahedral trimmer mesher generates the numerical mesh grid elements in the core of the liquid NaK-78 flow region. The smallest and largest mesh sizes varied between 0.25 mm and 0.5 mm. The prism layer mesher generates fine prismatic layers which decrease exponentially in size as they get closer to the Ti wall of the flow duct to accurately capture the hydrodynamic and thermal boundary layer for the flow (Fig. 11). This mesher generates 12 prism layers with a total thickness of 1.0 mm and an exponential stretching factor of 1.2.

The performed 3-D CFD analyses of the circulating liquid NaK-78 flow duct used the Reynolds Averaged Navier Stokes (RANS) Shear Stress Transport (SST) $k-\omega$ turbulence model for the liquid metal flow. The selected SST $k-\omega$ model includes a second order upwind convection scheme, the Durbin Scale limiter realizability, and the All- y^+ wall treatment model. The RANS turbulence model employs a turbulent Prandtl number, Pr_t , which is the ratio of the eddy viscosity and the eddy heat diffusivity. This number calculated using the Reynolds equation [34] accounts for the high thermal diffusivity and the low momentum diffusivity of the NaK-78 liquid flow in the duct in the Cs-Ti heat pipe's evaporator section.

The performed 3-D thermal analyses for the developed designs of the Cs-Ti heat pipe radiator modules determine the heat pipe condenser length for the same surface average temperature for radiative heat rejection into space, $T_s = 600$ K with a surface emissivity of 0.85 and the same width of the HOPG/Ti heat spreading fins, $W_{fin} = 10$ cm. The results of the Ver. 7 design determined the condenser length, L_{cd} , varying from 150 - 180 cm. For the longer evaporator Ver. 8 heat pipe module with the same HOPG/Ti/C-C heat spreading fins width, $W_{fin} = 10$ cm and condenser length $L_{cd} = 275$ cm. The inlet temperature and flow rate of the liquid NaK-78 in the duct are 650 K and 1.56 kg/s, respectively.

4.2 Results and discussion

The calculated surface temperature images (Fig. 12) show considerable variation across the heat pipe radiator module. The results presented for the Ver. 7 and 8 heat pipe modules in Fig. 12 are compared with those obtained for the Ver. 6 heat pipe module developed in the 2nd year of the project (Figs. 6 and 7) [23,24]. The temperature of the C-C armor on the upper surface of the heat pipe evaporator drops slightly by $\sim 9 - 11$ K along the length of the heat pipe condenser. The temperature also drops steadily along the thin 10 cm wide HOPG/Ti heat spreading fins (Fig. 12). Although the HOPG has a high lateral thermal conductivity, a small layer thickness of only 0.45 mm experiences a large drop in surface temperature along the fin width. The mean surface temperature for heat rejection for the Ver. 6 and 7 radiator modules with $L_{cd} = 180$ cm is 603 K and 598.9 K, respectively (Fig. 12). Based on these results the heat pipe condenser length to radiatively reject waste heat at a surface average temperature, $T_s = 600$ K are determined to be 179 cm for the Ver. 7 module. With this condenser length, NaK-78 inlet temperature of 650 K in the flow duct, and $T_s = 600$ K, the heat pipe module rejects a total of 5.64 kW.

Figure 12 also shows images of the surface temperature for the Ver. 8 heat pipe module with 50% longer evaporator length, $L_{ev} = 15$ cm. Increasing the length of both the HP evaporator section and the liquid NaK-78 flow duct increases the input thermal power to the heat pipe, requiring a larger surface area for heat rejection to space for the same surface average of 600 K. The power throughput of the Ver. 8 heat pipe module increases to 9.63 kW from the 6.08 kW transported by the Ver. 6 heat pipe module, both with the same Cs vapor flow area. The decrease in temperature along the 275 cm long condenser for the Ver. 8 heat pipe module remains low, at only ~ 15 K. This decrease in temperature across the 10 cm wide HOPG/Ti heat spreading fins

is similar for the two designs (Fig. 12). The average surface temperature for the Ver. 8 heat pipe module with $L_{cd} = 275$ cm is 601.1 K. For the same surface average temperature of 600 K the determined condenser length of the Ver. 8 heat pipe module is 277 cm.

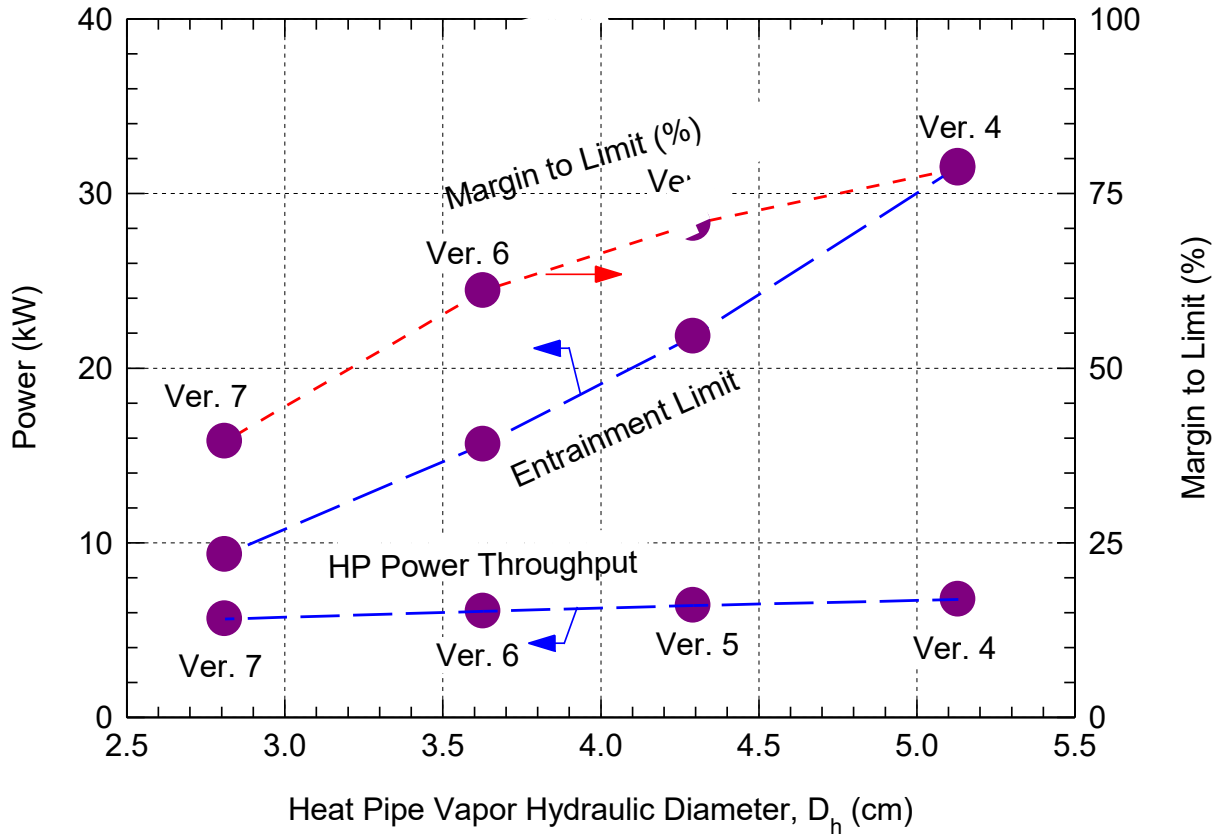


Figure 13: Estimates of the HP entrainment limit and the Power throughput Ver. 4, 5, 6, 7, and 8 of the Cs-Ti heat pipe radiator modules calculated using HPTrAM™ at NaK-78 inlet temperature of 650 K, versus equivalent hydraulic diameter of Cs vapor flow [24].

As shown in Fig. 13, the prevailing HP operation limit in the assorted designs of the Cs-Ti heat pipe radiator modules is the entrainment limit, which is calculated in HPTrAM™ as [35]:

$$Q_{ent} = A_{vap} h_{fg}(T_{ev}) \sqrt{\frac{\rho_v \sigma_l}{2R_p}} \quad (1)$$

In this expression, Q_{ent} is the heat pipe power throughput, A_v is the vapor cross section flow area in the Cs-Ti heat pipe, h_{fg} is the latent heat of evaporation of liquid Cs working fluid at the vapor pressure exiting the evaporator section, T_{ev} is temperature of the Cs vapor exiting the evaporator section of the heat pipe and ρ_v is the Cs vapor density, σ_l is surface tension of liquid Cs, and R_p is the average pore radius in the sintered Ti wick in the heat pipe, taken equal to 25 microns.

The HPTrAM™ calculated the power throughput corresponding to the entrainment limit of the Cs-Ti heat pipes in the radiator modules Ver. 4, 5, 6, and 7 at evaporator section temperature of 639 K. This corresponds to a liquid NaK-78 inlet temperature to the evaporator section's flow duct of 650 K. Decreasing the diameter of the Cs-Ti heat pipe, which in turn decreases the Cs vapor cross sectional flow area, increases the exit velocity of the Cs vapor in the evaporator section of the heat pipe. In the Ver. 7 radiator module, with the smallest vapor flow area in the

Cs-Ti heat pipe, the entrainment limit power throughput of ~ 9.3 kW is the lowest (Fig. 13). Decreasing the Cs vapor flow area or the equivalent hydraulic diameter of the vapor flow, D_h , in the heat pipes of the Ver. 4, 5, 6, and 7 radiator modules slightly decreases the heat pipe power throughput, which it equals that rejected into space.

Despite the lower power throughput for the Ver. 7 radiator module, the Cs-Ti heat pipe has a 40% operation margin from the prevailing entrainment limit (Fig. 13). This means that a radiator panel with multiple Ver. 7 modules can operate nominally with 40% failed modules (Fig. 13). This high redundancy confirms the avoidance of single point failures of the radiator panels on the lunar surface. The Ver. 8 heat pipe radiator module with power throughput of 9.63 kW operates at 61% of the entrainment limit (Fig. 13). However, the Ver. 6 design with the same vapor flow area only operates at 29% of the prevailing limit. These results show that increasing the lengths of the heat pipe evaporator and condenser sections increases the power throughput but decreases the operation margin of the Cs-Ti heat pipes for the radiator panel.

The performed operation and thermal analyses determined the dimensions of the heat pipe modules. These dimensions are then used to conduct micrometeoroid impact analyses. These analyses estimate the thicknesses of the C-C composite armors for Cs-Ti heat pipes and HOPG/Ti heat spreading fins as functions of the heat pipe perforation probability and the fins penetration probability.

5. Micrometeoroid Protection Analyses of Radiator Panel on Lunar Surface

The exposed surfaces of the heat spreading fins and the Cs-Ti heat pipes in the various radiator modules in Fig. 6 are armored with C-C composite for protection against impacts by micrometeoroids and space debris for more than 10 years of service life [19,20,23]. The C-C composite armor also protects the flow duct of the NaK-78 liquid. It transports the waste heat from the energy conversion subsystem to the evaporator section of the Cs-Ti heat pipes in the radiator panels (Figs. 8, 9).

A micrometeoroid impact that perforates both the C-C armor and Ti wall of the Cs heat pipe would cease its operation and vent the Cs working fluid into space. For redundancy, the Cs-Ti heat pipes in the radiator modules and panel in Figs. 6 and 9, are designed with 40% - 61% margin from the prevailing entrainment limit [24]. Thus, with 40% - 61% failing heat pipes in the radiator panels, the remaining radiator modules would reject the waste heat total thermal load into space.

A micrometeoroid impact that penetrates the HOPG/Ti heat spreading fins is of a lower consequence on the performance of the radiator modules and the panel. Micrometeorite penetrations through the fins slightly reduce the available surface area for waste heat rejection and the structural integrity of the fins. The obtained estimates of the areal density of the developed designs of the lightweight heat pipe radiator modules and panel incorporate the thicknesses and masses of the C-C armor for protecting the Cs-Ti heat pipes and the heat spreading fins on the lunar surface.

The objective of the work described in this section is to perform micrometeor protection analyses to estimate the thickness and mass of the C-C composite armors needed to protect the Cs heat pipes and the heat spreading fins of vertically erected radiator panels on the lunar surface (Fig. 9). These analyses determine the armor thicknesses to reduce the probabilities of perforating the heat pipes and penetrating the heat spreading fins to $\leq 10\%$ for 10 years' service on the lunar surface. The obtained results compare the effect of using a NASA and two European Space Agency (ESA) micrometeoroid environmental models on the estimates of the perforation probability of the Cs-Ti heat pipes and the penetration probabilities of the HOPG/Ti fins as functions of the C-C armor thicknesses. The determined C-C armor thicknesses and masses for the Vers. 4 - 7 Cs-Ti heat pipe radiator modules (Fig. 6) are incorporated into the estimates of the areal densities of the modules and of the integrated radiator panels (Fig. 9).

5.1 Micrometeoroid and orbital debris environmental models

The performed armor analyses used the NASA's Meteoroid Engineering Model (MEM) [36] and the two ESA Interplanetary Micrometeoroid Environmental Models, IMEM1 and IMEM2 [37,38], to estimate the thickness of the C-C armor for protecting exposed surfaces of the heat rejection radiator modules and panels from impacts by Micrometeoroid and Orbital Debris (MMOD). The implementation methodology involves the following steps:

- (1) define the average density and the size distributions of the incident micrometeors onto the exposed surface of the radiator modules, and
- (2) estimate the thickness of the C-C composite armor to protect against MMOD incident fluxes as a function of the perforation probability of the Cs-Ti heat pipe and the penetration probability of the HOPG/Ti heat spreading fins [23,27].

NASA's MEM is based on direct measurements and reported data from multiple sources:

- (a) radar observations of meteors from the Canadian Meteor Orbit Radar (CMOR),

- (b) micro-cratering rate on the Moon from analyses of meteor impacts on the Moon rocks returned during the Apollo missions, and
- (c) zodiacal brightness measurements for estimating the meteoroids population [39-40].

The MEM is the best fit for the direct measurements and the reported data sets [36]. It incorporates the equation reported by Gruen et al [41] for the cumulative interplanetary micrometeor flux, F_{ip} , of incident particles of mass $\geq m_p$, given as:

$$F_{ip}(m_p) = c_0 \left[(c_1 m_p^{0.306} + c_2)^{-4.38} + c_3 (m_p + c_4 m_p^2 + c_5 m_p^4)^{-0.36} + c_6 (m_p + c_7 m_p^2)^{-0.85} \right]. \quad (2)$$

In this expression, the coefficients $c_0 = 3.156 \times 10^7$, $c_1 = 2.2 \times 10^3$, $c_2 = 15$, $c_3 = 1.3 \times 10^{-9}$, $c_4 = 10^{11}$, $c_5 = 10^{27}$, $c_6 = 1.3 \times 10^{-16}$, $c_7 = 10^6$. The MEM is most accurate for spacecraft operating ~ 1.0 AU from the Sun but has greater uncertainty in estimating the micrometeor flux at distances close or further away from the Sun [40].

The IMEM1 and IMEM2 models for interplanetary particles from comets and asteroids are based on orbital collision modeling [37,38]. They are calibrated using: (a) thermal radiation measurements, (b) in situ dust measurements by the Galileo and Ulysses spacecraft, and (c) observations of the micro-cratering rate on the lunar surface [37,38]. Earlier IMEM1 divides the interplanetary dust populations into two components:

- (i) lighter mass particles with mass $< \sim 10^{-5}$ g, for which the Poynting-Robertson effect due to solar radiation drag is dominant, and
- (ii) higher mass particles, for which collisional dynamics dominate [37].

In addition to interplanetary sources, the IMEM1 accounts for interstellar particles, which are modeled as a mono-directional stream.

The IMEM2 [38] incorporates major revisions of the collision dynamics models for the interactions of the interplanetary dust. This model is based on simulations of meteor and cometary particle motion over a period of one-million years. It estimates the population evolution of the particles in the solar system for determining the interplanetary particle flux distribution. The collision dynamics models calculate the production of new dust particles from collisions and the removal of particles exhausting their collisional lifetime. The particle lifetime is determined from the rate of catastrophic collisions of sufficient magnitude to reduce the particle mass by at least half [38].

The empirical coefficients in the IMEM2 are adjusted according to the best fit of the results of the reported observations. These include:

- (a) infrared dust measurements by the Cosmic Background Explorer (CORE) mission,
- (b) observations of the micro-cratering rate on the lunar surface,
- (c) ground-based radar measurements of meteors, and
- (d) in-situ dust measurements by spacecraft.

Fig. 14 compares the predictions of the micrometeoroid cumulative interplanetary flux distributions using NASA's MEM, the ESA's IMEM1 and IMEM2 and the Gruen et al. [41] lunar flux model for micrometeor particle masses, m_p , from 10^{-18} to $\sim 5 \times 10^{-6}$ g. The compared micrometeor environment models in Fig. 14 show major differences in the predictions of the micrometeoroid cumulative fluxes. The MEM, IMEM1, and IMEM2 predict comparable fluxes for small mass particles, $m_p < 10^{-6}$ g. However, for large particles, $m_p > \sim 10^{-6}$ g, the IMEM1 consistently predicts lower fluxes than the MEM [40]. The IMEM2 cumulative fluxes predictions

are comparable to that of the MEM for particle mass $< \sim 10^{-6}$ g. However, for larger mass particles between 10^{-6} and 5×10^{-4} g, the shape of the cumulative flux predicted by the IMEM2 has a 'knee' and is higher than the MEM predictions [40]. The predictions of the cumulative flux by the IMEM2 drop below those of the MEM for particles mass $> 5 \times 10^{-4}$ g but are higher than those of the IMEM1.

Gruen et al [41] proposed a lunar micrometeor model based on micro-cratering analyses of Apollo Moon rocks. The cumulative flux predictions of this model are close to those of the interplanetary flux curves of the MEM for $m_p > 10^{-10}$ g but much higher for lower particle masses (Fig. 14). The difference is attributed to the formation of additional dust particles of ejecta material by micrometeor impacts on the lunar surface [41,42]. The close agreement between the lunar [41] and the interplanetary flux models supports the use of the latter in the present analyses for predicting the micrometeor environment fluxes of the incident particles with masses $> 10^{-10}$ g on the lunar surface.

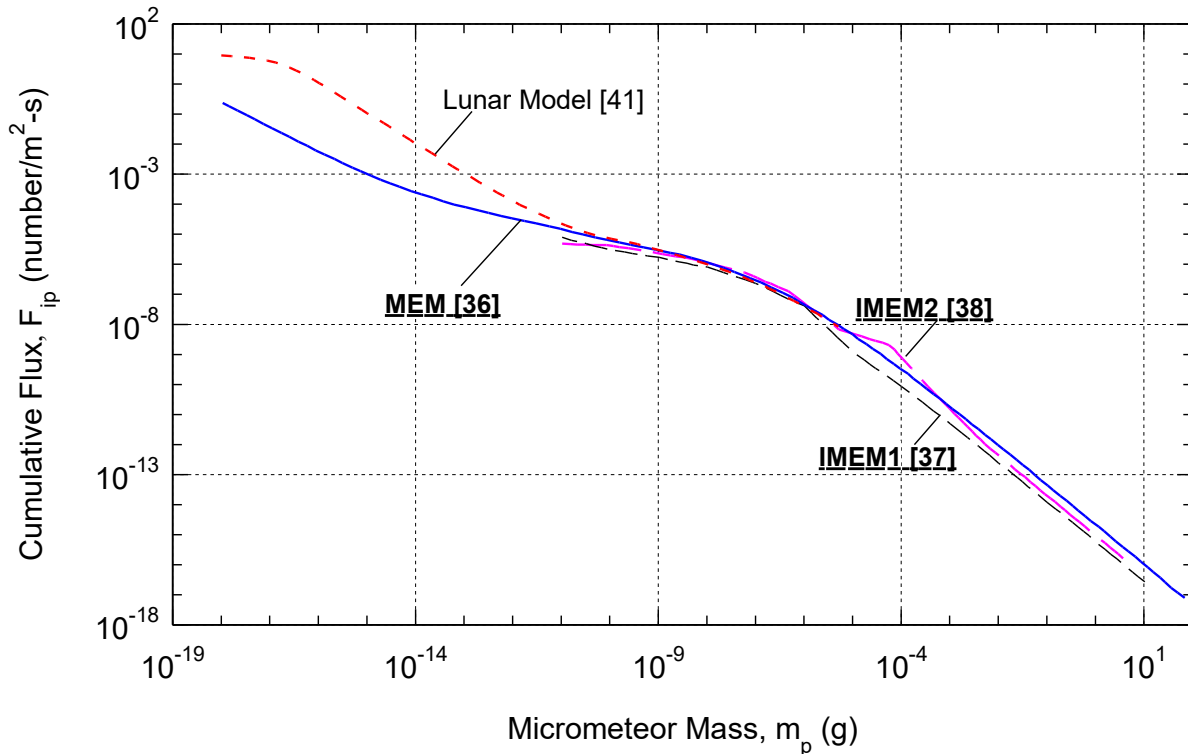


Figure 14: Comparison of the micrometeoroid cumulative interplanetary flux distributions for NASA’s MEM [36], ESA’s IMEM1 [37] and IMEM2 [38] and the micrometeoroid model of Gruen et al. [41] versus the micrometeor mass in grams [27].

Detailed simulation of the impacts of hypervelocity particles onto spacecraft structure using hydrodynamic shock codes is complex and computationally expensive [43,44]. Instead, spacecraft risk assessment has historically used semi-empirical Ballistic Limit Equations (BLEs). These equations developed based on experimental testing results [36,45] estimate the penetration probabilities by incident micrometeors or orbital debris through a spacecraft structure. They are derived from laboratory high velocity impact experiments using aluminum or steel spheres on flat plate targets of varied materials [43,46-48]. The BLEs determine the particle size to penetrate through to the back of the exposed target as a function of the impact parameters. These are the incident particle impact velocity and angle, and the particle and

target material densities. The BLEs assume that incident particles produce hemispherical craters in the surface of the armor or the target material.

Experimental results in the 1960's and 70's supported the development of NASA's first generation BLEs for spacecraft design [46]. The Modified Cour-Palais semi-infinite penetration equations by Johnson Space Center (JSC) are subsequently developed based on high velocity impact experiments using flat single layer plates of varied materials [46,48]. Results show that armor arrangements, with a 'bumper' or Whipple shield in front, could cause incoming micrometeorites to fracture into smaller particles, which are more easily stopped by underlying armor layers [46,48]. The BLEs for layered armor, developed by Boeing and NASA, supported the development of the protection design for the International Space Station.

The NASA Bumper family of micrometeoroid protection analysis software incorporates the BLEs for both single layer and multi-layer walls [48]. This software incorporates the JSC Modified Cour-Palais semi-infinite BLEs for a wide range of spacecraft materials. Schonberg [49] recently reported that the results of the JSC BLEs applied to the Russian Soyuz spacecraft for particle velocities greater than 10 km/s were conservative compared to the those of the experimental tests performed using representative Soyuz walls. However, these results demonstrated that the models could produce satisfactory predictions for analyses of real multi-layer spacecraft structures. The implemented approach for estimating the thickness of the C-C composite armor for the present designs of the lightweight Cs-Ti heat pipe radiator modules (Fig. 13) are detailed and discussed next.

5.2 Methodology and approach

The performed analyses determined the thicknesses of the C-C composite armors for the Cs-Ti heat pipes and the HOPG/Ti heat spreading fins of the radiator modules based on the NASA's MEM and ESA's IMEM1 and IMEM2 predictions of the cumulative flux distributions of the incident micrometeoroids. Calculated is the impact probability of micrometeoroids with a mass $> m_p$ and a specified impact velocity, V , onto the exposed surfaces of the Cs-Ti heat pipe and the heat spreading fins in the radiator modules (Figs. 5 and 6). The determined impact probabilities are for the heat rejection radiator panel (Fig. 9) erected vertically on the lunar surface with no specific orientation relative to the Moon's orbit. The determined impact probabilities estimate the penetration depths of the impacting flux of micrometeoroids using the Modified Cour-Palais semi-infinite penetration equations by NASA Johnson Space Center (JSC). The probabilities of perforating the Cs-Ti heat pipes and of penetrating the HOPG/Ti heat spreading fins are calculated as functions of the C-C armor thicknesses.

The estimate of the incident micrometeors flux of particle mass $\geq m_p$ onto the lunar surface, F_r , is calculated using the following equation by Anderson and Smith [36], as:

$$F_r(m_p) = F_{ip}(m_p) s_f G_p \quad (3)$$

In this equation, F_{ip} is the interplanetary micrometeor flux in particles/m²-yr. The factor, s_f , on the right-hand side accounts for the solid angle of the incoming isotropic micrometeor particles, and the factor G_p accounts for the focusing effect of a planetary body's gravity to draw in nearby meteoroids. The value of F_{ip} depends on the choice of the micrometeoroid environmental model. The present analyses obtain the values of F_{ip} from the cumulative flux distributions using NASA's MEM and ESA's IMEM1 and IMEM2 models (Fig. 14). The value of s_f in Eq. (3) is taken equal to 0.5 since the Moon's surface will block half the solid angle of incoming meteorites flux onto the vertically erected radiator panels.

The performed analysis estimates the number N , of impacting micrometeors of particles with masses $\geq m_p$ over a ten-year duration, t , using the calculated F_r from Eq. (3) as:

$$N(m_p) = k F_r(m_p) A T \quad (4)$$

In this expression, A is the projected area of the Cs-Ti heat pipe or of the HOPG/Ti heat spreading fins (Fig. 6).

The probability, P , that a single incident particle of mass $\geq m_p$ will impact vertically erected radiator module (Fig. 6) or panel (Fig. 9) on the lunar surface [36], depends on the calculated number of impacts using Eq. (4) and is expressed as:

$$P(m_p) = N(m_p) e^{-N(m_p)}. \quad (5)$$

The performed ballistic analyses of the Cs-heat pipe rejection radiator modules estimate the C-C composite armor thicknesses needed to prevent perforation of the heat pipe and penetration of the heat spreading fins by an incoming micrometeor particles with mass $\leq m_p$.

The present analysis also calculates the depths of the produced craters in semi-infinite layers of the target materials as functions of the meteorite particle diameter and impact velocity. The current NASA models include the JSC Cour-Palais equations for a wide range of materials, such as aluminum, titanium, stainless steel, ceramic tiles, and carbon fiber reinforced composites [48]. For structures of multiple joined layers of dissimilar materials, the analyses convert the different layers into equivalent thicknesses of aluminum [48].

Corderley, et al. [50] have experimentally investigated the impacts of hypervelocity particles on reinforced carbon fiber/titanium laminated composites. The results for composite laminate panels impacted by an explosively formed metal penetrator suggested that the equivalent aluminum thickness of layers of dissimilar materials for ballistic limit analyses may be calculated as:

$$\delta_{al} = \left(\rho_{al}/\rho_{mat}\right)^{-0.159} \left(UTS_{al}/UTS_{mat}\right)^{0.236} \quad (6)$$

In this expression, δ_{al} is the equivalent aluminum thickness, ρ_{al} and ρ_{mat} are the densities of aluminum and the composite layers materials, respectively, and UTS_{al} and UTS_{mat} are the ultimate tensile strengths of aluminum and the composite layers of various materials, respectively. The present armor analyses of the Cs-Ti heat pipe radiator modules account for the thicknesses of titanium wall, the HOPG layer and Ti casings in the fins, and the C-C composite armor layers in equivalent thicknesses of aluminum. The analysis of the C-C composite armor for the Cs-Ti heat pipe uses an equivalent aluminum thickness of the Ti wall and the C-C composite armor.

The estimated penetration depth based on the BLEs conservatively assumes that the incident particles have an impact angle of 90° onto the surface, or a normal orientation. This is because the vertically erected radiator panels on the lunar surface are assumed not to have a preferential orientation relative to the incident micrometeor flux particle. The Cour-Palais semi-infinite plate equation for impacted aluminum with a normal incident particle estimates the penetration depth [48], is given as:

$$\delta_\infty = 5.24 HB^{-0.25} \left(\rho_p/\rho_{al}\right)^{0.5} (V/C)^{2/3} d_p^{19/18} \quad (7)$$

In this expression, δ_{∞} is the depth of penetration for the hemispherical impact crater created by the incident particle, HB is the Brinell hardness of aluminum, d_p is the diameter of the incident particle, ρ_p and ρ_{al} are the particle and aluminum densities, respectively; V is the impact velocity of the incident particle, and C is the speed of sound for aluminum.

The force of impact by micrometeorite particles can cause fractures or spalling from the back surface of the target structure. A resulting perforation of the Cs-Ti heat pipe would vent the Cs working fluid to vent into space [48]. Therefore, the penetration depth, δ_{∞} , using Eq. (7) is that of the micrometeor impact crater in the target material, referred to as the penetration depth. This depth determines the thickness of the C-C composite armor needed to stop an incident particle from passing completely through the structure.

The NASA Bumper code recommends that the calculated value of δ_{∞} , using Eq. (7) be increased by a factor of 1.8 to determine the perforation depth of a hermetically sealed barrier like the C-C armored Ti wall of the Cs heat pipes in the heat rejection radiator modules in Fig. 9. This depth represents the armor thickness required to avoid perforation of a hermetic boundary by an impacting hypervelocity particle. Rearranging the Cour-Palais semi-infinite plate BLE (Eq. 7), the micrometeor diameter in terms of the equivalent aluminum thickness, δ_{al} , to guard against penetration (Eq. 8a) and perforation (Eq. 8b), is expressed, as:

$$d_p = \left[\frac{\delta_{al}}{5.24 \text{ HB}^{-0.25} \left(\frac{\rho_p}{\rho_{al}} \right)^{0.5} \left(\frac{V}{C} \right)^{2/3}} \right]^{18/19}, \text{ for penetration} \quad (8a)$$

$$d_p = \left[\frac{\delta_{al}/1.8}{5.24 \text{ HB}^{-0.25} \left(\frac{\rho_p}{\rho_{al}} \right)^{0.5} \left(\frac{V}{C} \right)^{2/3}} \right]^{18/19}, \text{ for perforation.} \quad (8b)$$

The present analyses use Eq. (8a) in the armor analysis of the HOPG/Ti heat spreading fins where impacting micrometeor may pass completely through the fins. The armor analysis of the C-C armored Cs-Ti heat pipes, however, uses Eq. (8b) for perforating the C-C composite armor and the underlying Ti wall. For a spherical particle, the diameter is related to its mass, m_p , as:

$$m_p = \frac{4\pi\rho_p}{3} d_p^3 \quad (9)$$

The use of Eq. (8a) and Eq. (8b) together with Eq. (9) determines the lowest mass, m_p , and impact velocity, V, of an incident micrometeoroid particle to perforate an equivalent thickness of aluminum. The obtained value of m_p is used in Eq. (5) to determine the corresponding perforation probability, P, of C-C armored the Cs-Ti heat pipe and the penetration probability of the armored heat spreading fins.

5.3 Armor analysis results

This section presents the results for the armoring analyses of the heat rejection radiator modules (Fig. 6) and the panel (Fig. 9) using C-C composite fibers for > 10-year service on the lunar surface. As the orientation of the incoming interplanetary flux relative to the vertically erected radiator panels on the Moon is not known, the incident meteorites source is conservatively assumed isotropic. Thus, in Eq. (3) for determining incident particles flux, $k_f = 1$. The performed armoring analyses use a planetary shielding factor = 0.5 because the vertically erected radiator panels on the lunar surface would on average encounter half of the incident

particles flux from interplanetary space. The planetary body of the Moon will block the other half of the incident source particles.

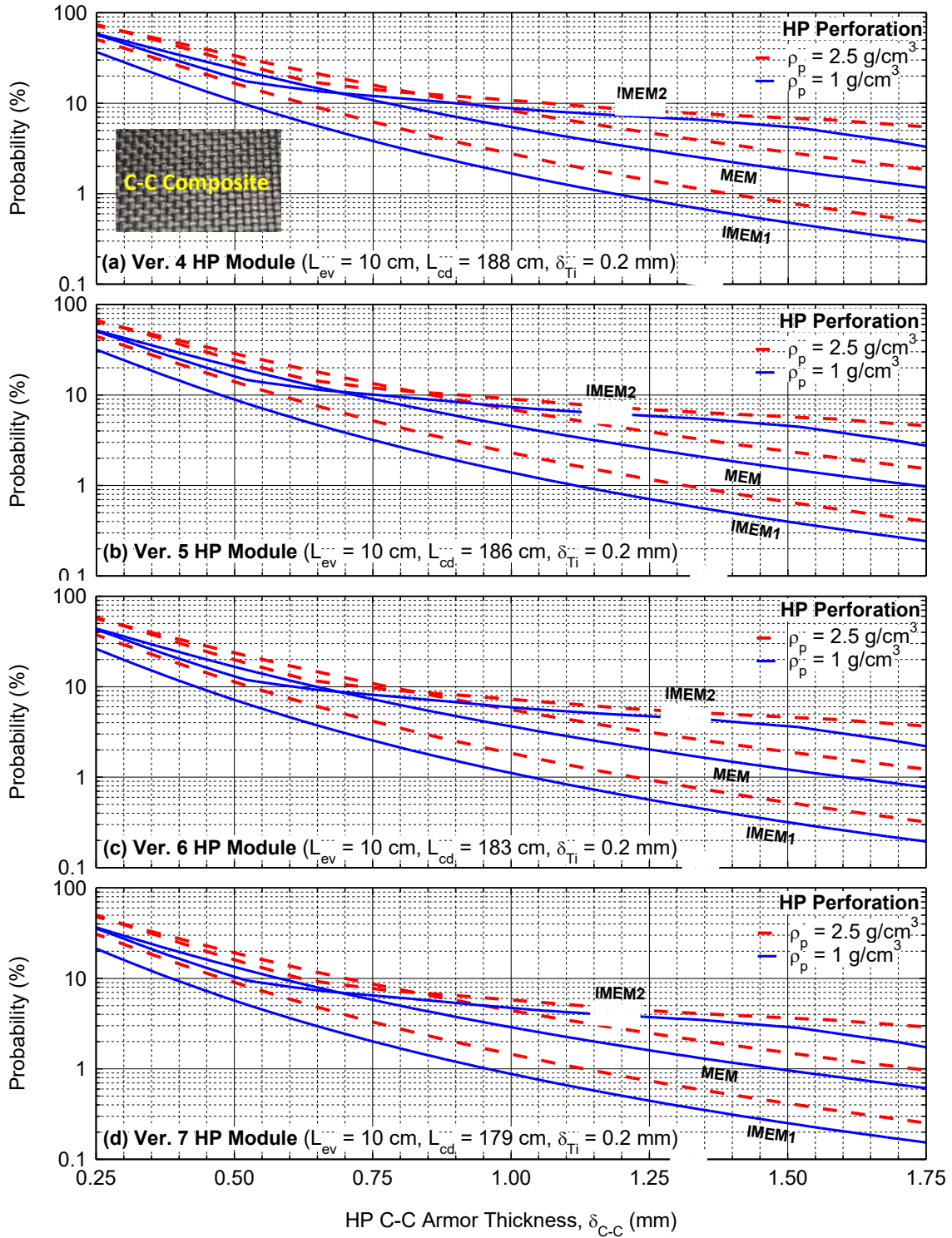


Figure 15: Comparisons of perforation probabilities of Cs-Ti heat pipes with C-C composite armor in radiator modules in Fig. 6, using MEM, IMEM1, and IMEM2 for incident particles densities of 1.0 and 2.5 g/cm³ [51].

According to Gruen, et al. [41] the interplanetary flux for particles $> \sim 10^{-9}$ g in mass is the same as that on the lunar surface, therefore, the present analyses use $G_p = 1.0$ in Eq. (3). The particles for defeating an equivalent thickness of aluminum depends on their mass, density, impact velocity and incident angle. The present analyses conservatively assume that incident particles perpendicularly impact the surface of the C-C armor at a mean velocity of 17 km/s, as suggested by Anderson and Smith [36] for NASA's MEM

The performed analyses estimate the perforation and penetration probabilities of the Cs-Ti heat pipe and the Ti/ HOPG heat spreading fins, respectively, of the lightweight radiator modules in Fig. 6 using the MEM, IMEM1 and IMEM2 micrometeor environmental models [36-38]. The NASA MEM recommends using a particle density of 1.0 g/cm^3 , which represents a porous rock of cometary origin [36,42]. Gruen et al. [41] have reported that in-situ collection of interplanetary dust particles by spacecraft supports a particle density close to 1.0 g/cm^3 . However, they determined that the micro-cratering Moon rocks, returned during the Apollo missions, suggest a higher density of 2.5 g/cm^3 for micrometeors impacting the lunar surface.

The impact of the high-density particles will cause deep penetration requiring thicker armor for protection. The present analysis investigated the effect of incident particles densities of 1.0 and 2.5 g/cm^3 on the needed thicknesses of the C-C composite armor as functions of the perforation and penetration probabilities of the Cs-Ti heat pipe and the Ti / HOPG heat spreading fins of the radiator modules (Fig. 6) on the lunar surface.

5.3.1 Estimates of C-C armor for Cs-Ti heat pipes

The performed armor analyses of the radiator modules in Fig. 6 estimate the perforation probability of the Cs-Ti heat pipe by a micrometeor impact during a 10-year service on the lunar surface. The target is the projected area for the Cs-Ti heat pipe. As indicated earlier, the Cs-Ti heat pipe diameter in the modules in Fig. 6 decreases from 8.73 cm for Ver. 4 design to 4.60 cm in Ver. 7, and the heat pipe condenser length decreases with decreased heat pipe diameter or power throughput. The projected area of the Cs-Ti heat pipe is $1,728.5 \text{ cm}^2$ in Ver. 4 module and 869.4 cm^2 for the smallest diameter Ver. 7 module. The projected areas of the heat pipe in Ver. 5, 6, and 7 modules are 83.2%, 66.3%, and 50.3% of that of Ver. 4 module, respectively. The smaller projected area of heat pipe decreases the probability that the impact of an incident particle of a given density can perforate the heat pipe wall while it is protected by a specified thickness of the C-C composite armor.

The estimated perforation probability of the Cs-Ti heat pipe in Ver. 4 radiator module (Fig. 6) decreases rapidly to 10% as the C-C armor thickness increases to 0.92 mm (Fig. 15a and Table 5). Based on NASA's MEM, with 0.78 mm thick C-C armor the perforation probability of the Cs-Ti heat pipe by incident particles with a mean density of 1.0 g/cm^3 , is 10%. This C-C composite armor thickness is larger than that (0.51 mm) determined using the IMEM1, and slightly smaller (0.90 mm) than that determined using the IMEM2 (Fig. 15a and Table 5). These thicknesses of the C-C composite armor increase to 1.03 mm, 0.68 mm, and 1.55 mm, respectively, for halve the perforation probability of the Cs-Ti heat pipe of 5%, for 10-year service on the lunar surface. Further decrease in the heat pipe perforation probability requires much thicker C-C armor (Table 5). Results in Figs. 15a-d show that the estimates of the C-C composite armor thicknesses for the Cs-Ti heat pipes using NASA's MEM fall between those using ESA's IMEM1 and IMEM2, with the latter being the most conservative.

For a 5% perforation probability of the Cs-Ti heat pipe with incident particles having a density of 1.0 g/cm^3 , the estimates of the C-C composite armor thicknesses in the Ver. 7 radiator module using the NASA MEM are 22% lower than that in the Ver. 4 module (Fig. 15). For a perforation probability of 1%, the NASA MEM estimate of the C-C armor thickness of the Cs-Ti heat pipe in the Ver. 7 module is 19% lower than that in Ver. 4 module. For the same

thicknesses of the C-C composite armor, the perforation probabilities of the Cs-Ti heat pipe with a particle density of 2.5 g/cm^3 are higher than with a particle density of 1.0 g/cm^3 . For the same probability, the high-density particles require 10% - 23% thicker C-C composite armor to protect the Cs-Ti heat pipes in the radiator modules (Figs. 15, 16). The perforation probabilities for the armored Cs-Ti heat pipes in Ver. 4 - 7 radiator modules (Fig. 6) are compared in Figs. 15a-d as functions of the C-C composite armor thickness, δ_{c-c} .

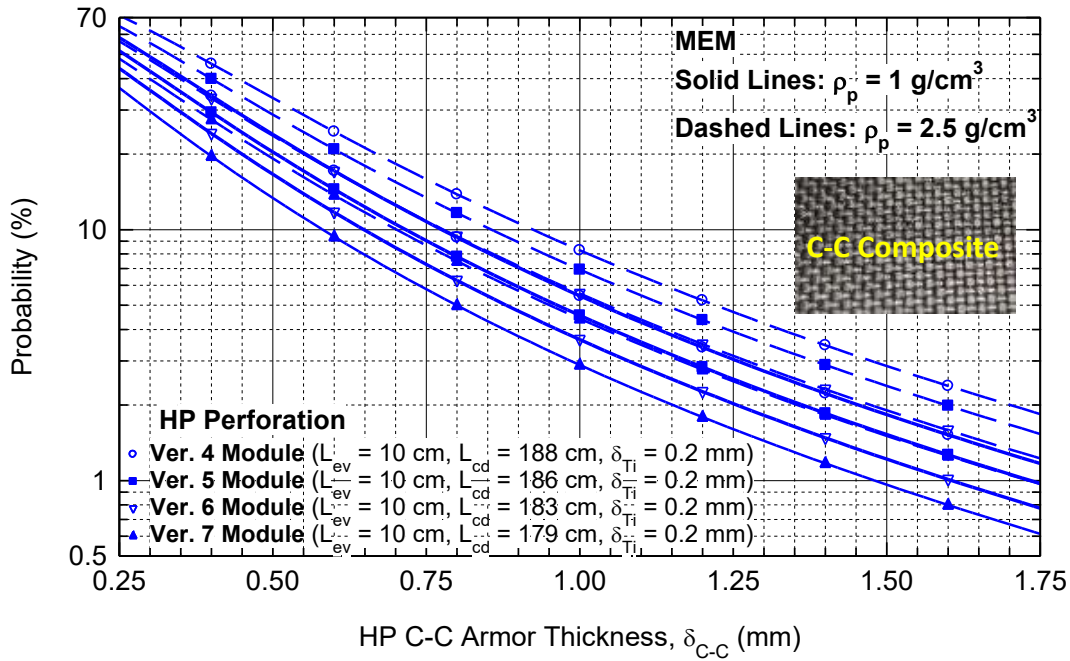


Figure 16: Perforation probability estimates of Cs-Ti heat pipes with C-C composite armor in Ver. 4-7 radiator modules (Fig. 6) for incident particle densities of 1.0 and 2.5 g/cm^3 [51].

Table 5. Estimates of the C-C armor thicknesses of the Ti-Cs heat pipe in the radiator modules (Fig. 6) for perforation probabilities of 1%, 5%, and 10% for 10 years on lunar surface [51].

Incident Particle Density, ρ_p (g/cm^3)	Version of Radiator Module (Fig. 6), L_{cd} (cm)	HP C-C Armor Thickness, δ_{c-c} (mm) for 10 years operation								
		MEM - Perforation Probability, P			IMEM1- Perforation Probability, P			IMEM2- Perforation Probability, P		
		1%	5%	10%	1%	5%	10%	1%	5%	10%
1	4, 188	1.84	1.03	0.78	1.19	0.68	0.51	2.18	1.55	0.90
	5, 186	1.73	0.96	0.72	1.12	0.63	0.48	2.14	1.42	0.76
	6, 183	1.61	0.88	0.65	1.04	0.58	0.43	2.07	1.18	0.61
	7, 179	1.48	0.80	0.58	0.96	0.53	0.39	1.97	0.95	0.51
2.5	4, 188	2.12	1.22	0.92	1.39	0.81	0.62	2.38	1.81	1.07
	5, 186	2.02	1.14	0.86	1.31	0.76	0.58	2.35	1.66	0.91
	6, 183	1.88	1.04	0.78	1.22	0.70	0.53	2.31	1.38	0.73
	7, 179	1.73	0.95	0.70	1.13	0.64	0.48	2.24	1.13	0.62

These results are for a heat pipe Ti wall thickness of 0.2 mm and C-C composite armor on the surfaces exposed to space. In Figs. 15a-d the results for mean particle density of 1.0 g/cm³ recommended by NASA’s MEM are plotted using solid lines, while those for the incident 2.5 g/cm³ particles recommended by the model by Gruen et al. [41] are plotted using dashed lines.

The range of interest in the present investigations starts at the beginning of the ‘knee’ in the cumulative flux curve of ESA’s IMEM2 (Fig. 14). NASA’s MEM predicts the highest perforation probability of the Cs-Ti heat pipes with C-C composite armor thicknesses < ~ 0.6 mm followed by ESA’s IMEM2, then the IMEM1 (Fig. 15a-d). The calculated perforation probabilities using IMEM2 for thicker C-C armors are much higher than those calculated using both NASA’s MEM and ESA’s IMEM1. For a 10% perforation probability with incident particle density of 2.5 g/cm³, the NASA MEM estimate of the C-C composite armor thickness is 0.92 mm in the Ver. 4 radiator module (Fig. 6). This is ~18% higher than the determined thickness of 0.78 mm for lower particle density of 1.0 g/cm³ (Table 6). With ESA’s IMEM1, these estimates of the C-C composite armor thickness are 0.62 and 0.51 mm, for incident particle densities of 2.5 g/cm³ and 1.0 g/cm³, respectively. For the same perforation probability of 10% with incident particle densities of 2.5 g/cm³ and 1.0 g/cm³ and based on ESA’s IMEM2 the estimates of the C-C composite armor thicknesses of the Ti-Cs heat pipe in the Ver. 4 module are 1.07 mm and 0.90 mm, respectively (Table 5).

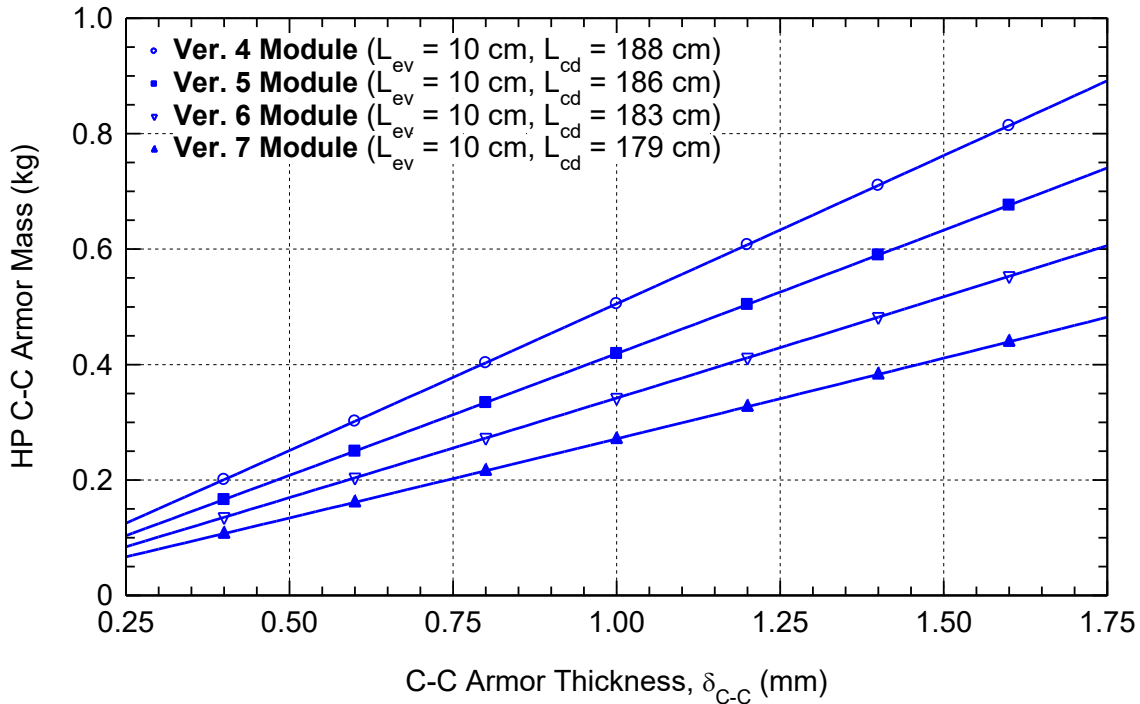


Figure 17: Mass estimates of the C-C composite armor of the Cs-Ti heat pipes C-C in the Vers. 4 - 7 modules (Fig. 6) using NASA’s MEM [51].

Increasing the thickness of the C-C composite armor decreases the perforation probability of the Cs-Ti heat pipe, but at the expense of increasing the armor mass. Fig. 17 and Table 6 compare the mass estimates of C-C armor of the Cs-Ti heat pipes in Ver 4 - 7 radiator modules in Fig. 6. These masses are for 1.0 and 2.5 g/cm³ incident particles. The mass estimate of the C-C heat pipe armor using NASA’s MEM for a heat pipe perforation probability of 5% by 1.0 g/cm³ incident particles is 0.495 kg for the Ver. 4 module compared to 0.40 kg, 0.308 kg, and 0.216 kg for Ver. 5, 6, and 7 modules, respectively (Table 6). For a higher perforation probability of 10%, the mass of the C-C armor for the Cs-Ti heat pipes in the radiator modules

decreases by 25%-28%. Conversely, increasing the armor thickness to decrease the perforation probability from 5% to 1% using NASA's MEM increases the mass of the heat pipe's C-C armor by 80% - 88%. The lower masses of the C-C composite armor in the modules with the smaller diameter heat pipes is due to a combination of a reduced armor thickness and a smaller projected surface area.

Table 6. Comparison of the mass estimates of C-C armor of the Ti-Cs heat pipes in the radiator modules (Fig. 6) for proliferation probabilities of 1%, 5%, and 10% in 10 years on lunar surface with particle densities of 1.0 and 2.5 g/cm³ [51].

Incident Particle Density, ρ_p (g/cm ³)	Radiator Module Version (Fig. 6), L_{cd} (cm)	Mass Estimates of the Radiator Module C-C composite Armor (kg)								
		MEM - Perforation Probability, P			IMEM1- Perforation Probability, P			IMEM2- Perforation Probability, P		
		1%	5%	10%	1%	5%	10%	1%	5%	10%
1	4, 188	0.892	0.495	0.369	0.569	0.323	0.244	1.067	0.749	0.422
	5, 186	0.728	0.400	0.297	0.465	0.262	0.196	0.903	0.593	0.374
	6, 183	0.568	0.308	0.226	0.363	0.202	0.150	0.736	0.417	0.213
	7, 179	0.405	0.216	0.156	0.260	0.142	0.103	0.548	0.258	0.137
2.5	4, 188	1.032	0.585	0.441	0.671	0.388	0.296	1.170	0.878	0.502
	5, 186	0.822	0.474	0.355	0.549	0.315	0.239	0.997	0.697	0.374
	6, 183	0.667	0.366	0.272	0.430	0.244	0.184	0.823	0.492	0.257
	7, 179	0.476	0.258	0.189	0.308	0.173	0.128	0.626	0.307	0.167

5.3.2 C-C Arming HOPG/Ti heat spreading fins

The four versions of the heat rejection radiator modules in Fig. 6 employ 10 cm wide HOPG/Ti heat spreading fins. The fins run the full length of the Cs heat pipe, including the condenser and evaporator sections. The estimates of the C-C composite armor thickness of the fins are based on the equivalent aluminum thickness of both the 0.45 mm thick HOPG layer and the 0.1 mm thick Ti encasing the HOPG (Fig. 5c). The analyses calculate the penetration probability of the HOPG/Ti fins as a function of the thickness of the applied C-C composite armor. Figs. 18a-d and 19 show that the estimates of the C-C armor thickness of the heat spreading fins based on the IMEM2 model are the highest, followed by those using MEM and IMEM1, respectively. For a specified C-C armor thickness the estimates of the penetration probabilities based on ESA's IMEM1 are the lowest, followed by those based on NASA's MEM, with the IMEM2 predicting the highest penetration probabilities (Figs. 18a - d, 19). The penetration probabilities with an incident particle density of 2.5 g/cm³ are consistently higher than those with a particle density of 1.0 g/cm³. For the same mass, m_p , the higher density particles penetrate further.

The analyses estimate a C-C composite armor thickness, $\delta_{C-C,f}$, of only 0.12 mm for the heat spreading fins based on the ESA's IMEM1 and a penetration probability < 4% with incident particle density of 1.0 g/cm³ (Figs. 18, 19). For higher penetration probabilities, no C-C composite armor will be needed for HOPG/Ti the heat spreading fins. For a 5% penetration probability, the thickness estimates of the C-C composite armor for the fins using ESA's IMEM2

is 2.3 times that based on NASA's MEM (Figs. 18a-c, 19). Owing to the small difference in the estimates of the C-C composite armor thickness for the HOPG/Ti fins in the Ver. 4, 5, and 6 radiator modules (Fig. 19 and Table 7), the total mass of the armor for the fins is small and varies only slightly among modules (Fig. 20 and Table 8).

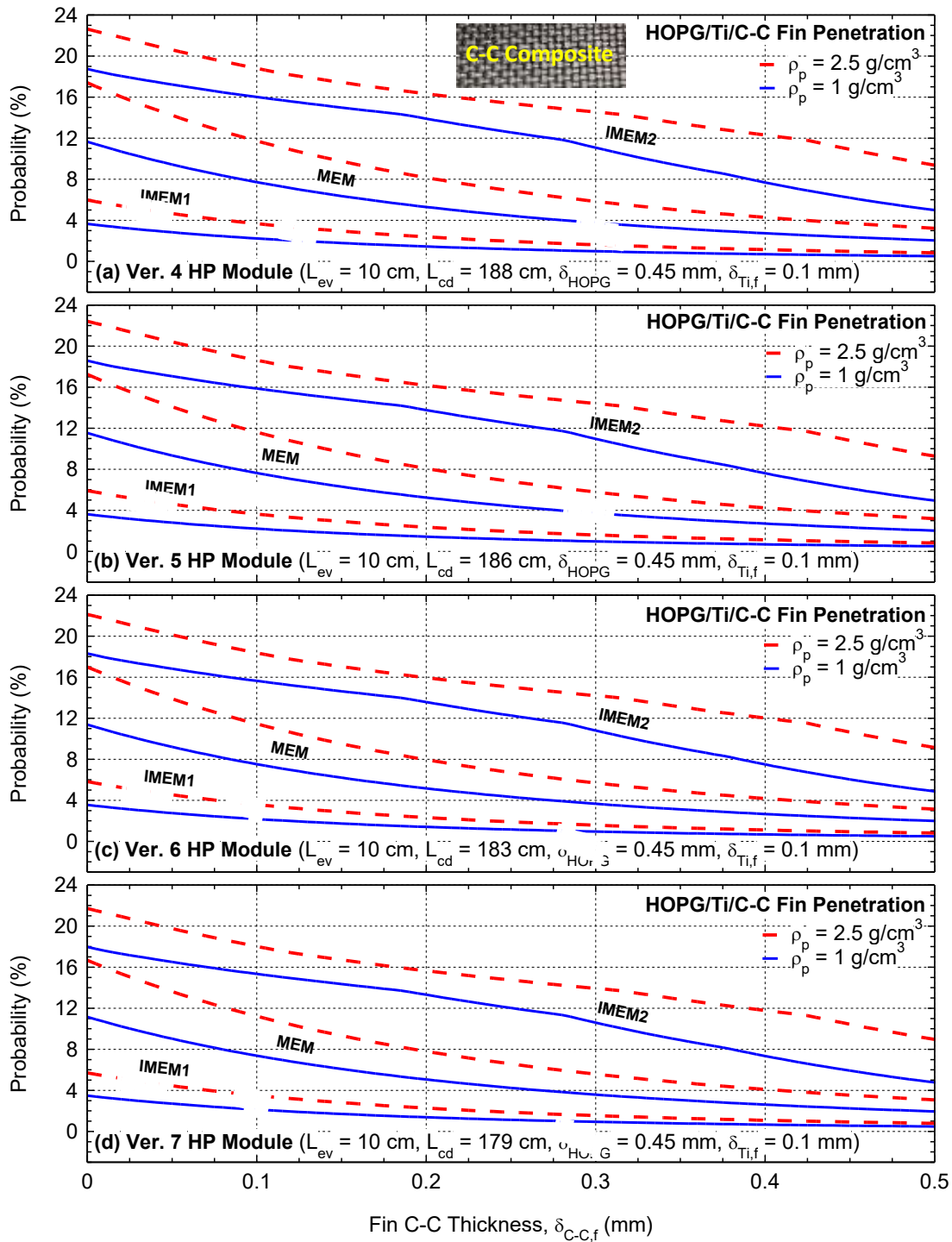


Figure 18: Comparison of the estimated penetration probabilities of the 10 cm-wide HOPG/Ti heat spreading fins in Vers. 4-7 radiator modules (Fig. 6), using ESA IMEM1, NASA MEM and ESA IMEM2 for 1.0 and 2.5 g/cm³ incident particle densities [51].

Table 7. C-C composite armor thickness the heat spreading fins in radiator modules (Fig. 6) for 10-year on lunar surface and penetration probabilities of 2%, 5%, and 10% [51].

Incident Particle Density, ρ_p (g/cm ³)	Radiator Module Version (Fig. 6), L_{cd} (cm)	Estimates of C-C composite armor thickness, $\delta_{C-C,f}$ (mm) of heat spreading fins for 10 years on Lunar Surface								
		MEM - Penetration Probability, P			IMEM1- Penetration Probability, P			IMEM2- Penetration Probability, P		
		2%	5%	10%	2%	5%	10%	2%	5%	10%
1	4, 188	0.507	0.216	0.036	0.124	None	None	0.744	0.500	0.329
	5, 186	0.503	0.213	0.034	0.122	None	None	0.741	0.498	0.326
	6, 183	0.498	0.209	0.030	0.120	None	None	0.737	0.494	0.322
	7, 179	0.491	0.203	0.026	0.114	None	None	0.731	0.489	0.316
2.5	4, 188	0.682	0.349	0.143	0.244	0.035	None	0.885	0.674	0.479
	5, 186	0.678	0.346	0.140	0.241	0.032	None	0.884	0.672	0.475
	6, 183	0.672	0.341	0.136	0.237	0.030	None	0.882	0.667	0.471
	7, 179	0.664	0.335	0.131	0.232	None	None	0.878	0.662	0.464

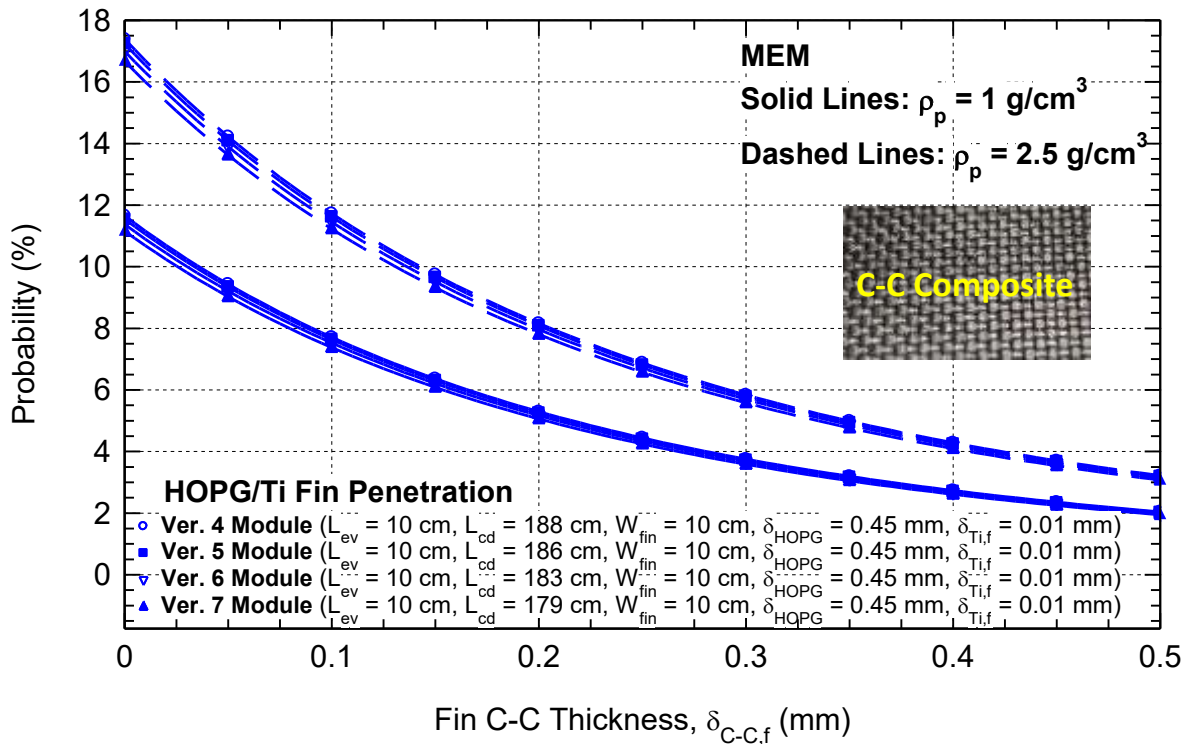


Figure 19: Estimates based on NASA’s MEM of the penetration probability of the HOPG/Ti heat spreading fins of Vers. 4-7 radiator modules in Fig. 6, for particle densities of 1.0 and 2.5 g/cm³ [51].

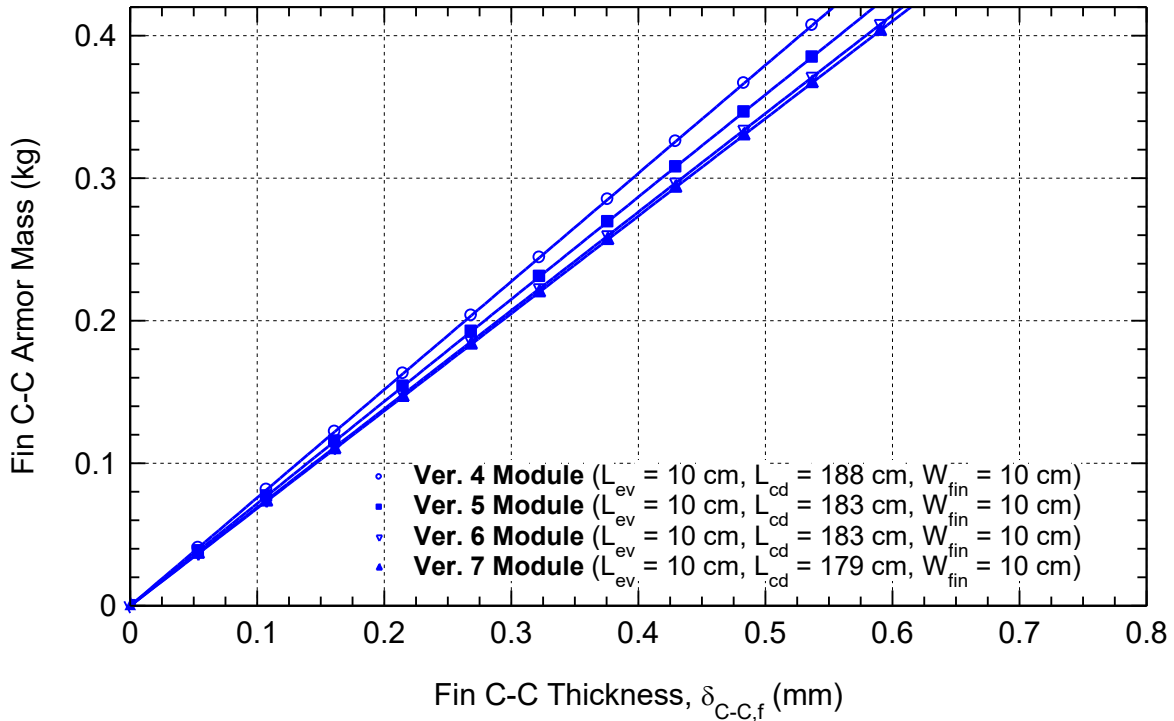


Figure 20: Mass estimates of the C-C composite armor of the HOPG/Ti heat spreading fins in Vers. 4-7 radiator modules in Fig. 6 [51].

Table 8. Mass estimates of the C-C armor of the heat spreading fins of radiator modules in Fig. 6 for 10-year on the lunar surface and penetration probabilities of 2, 5, and 10% [51].

Incident Particle Density, ρ_p (g/cm^3)	Radiator Module Version (Fig. 6), L_{cd} (cm)	Mass estimates of C-C composite armor of heat spreading fins for 10 years on the lunar surface (kg)								
		MEM - Penetration Probability, P			IMEM1- Penetration Probability, P			IMEM2- Penetration Probability, P		
		2%	5%	10%	2%	5%	10%	2%	5%	10%
1	4, 188	0.385	0.164	0.027	0.094	0	0	0.565	0.379	0.250
	5, 186	0.361	0.153	0.024	0.087	0	0	0.532	0.357	0.234
	6, 183	0.340	0.143	0.021	0.082	0	0	0.504	0.338	0.220
	7, 179	0.339	0.140	0.018	0.078	0	0	0.505	0.338	0.219
2.5	4, 188	0.518	0.265	0.108	0.185	0.027	0	0.672	0.511	0.363
	5, 186	0.486	0.248	0.101	0.173	0.024	0	0.634	0.482	0.341
	6, 183	0.459	0.233	0.093	0.162	0.021	0	0.603	0.456	0.322
	7, 179	0.458	0.231	0.090	0.160	0	0	0.607	0.457	0.321

Presented results in Fig. 20 and listed in Table 8 compare the calculated mass estimates of the C-C composite armor of the fins in the heat pipe modules (Fig. 6) using NASA's MEM. For a penetration probability of 5% for 10 years on the lunar surface and meteoroids particle density of 1.0 g/cm^3 the estimated mass of the C-C composite armor of the fins in the Ver. 4 module is only 23 gm higher than for the Ver. 7 module (Fig. 20). Although the projected areas of the heat spreading fins are larger than those of the Cs-Ti heat pipes, the mass estimates of the C-C armor of the fins are much lower than for the heat pipe due to the smaller armor thickness of the fins (Tables 6 and 8). For a 5% perforation probability of the Cs-Ti heat pipe impacted with 1.0 g/cm^3 micrometeoroids, the mass estimate based on NASA's MEM of the C-C composite armor for Cs-Ti heat pipe in Ver. 4 radiator module (Fig. 6) is 0.495 kg (Fig. 17). This mass is ~3 times the 0.164 kg of the C-C composite armor of HOPG/Ti heat spreading fins for a 5% penetration probability of (Fig. 20).

5.4. Summary

The performed armor analyses determined the thickness of the C-C composite armor of the Vers. 4-7 lightweight Cs-Ti heat pipe modules assembled in the vertically erected heat rejection radiator panels on the lunar surface. Investigated are the effect of incident particle density of 1.0 and 2.5 g/cm^3 on the perforation probability of the Cs-Ti heat pipe and the penetration probability of the heat spreading fins and the corresponding thicknesses of the C-C composite armor. The determinations of the armor thicknesses are based on three different micrometeoroid flux distributions models: NASA's MEM and ESA's IMEM1 and IMEM2.

For a 5% perforation probability of the Cs-Ti heat pipes by incident particles with a density of 1.0 g/cm^3 , the estimated thickness of the heat pipe C-C armor varies from 0.8 mm in the Ver. 7 module to 1.48 mm in Ver. 4 module. For a 5% penetration probability of the heat spreading fins by incident micrometeorite particles, the estimated armor thickness is $< 0.2 \text{ mm}$. For the same penetration probability, the thickness of the C-C composite armor for incident particles with a higher mean density of 2.5 g/cm^3 increases by 18% - 20%.

Doubling the perforation and penetration probabilities to 10% decreases the thickness and mass of the C-C composite armor of the Cs-Ti heat pipes by 25% - 28% and those of the heat spreading fins by 83 - 87%. A 10% perforation probability of the Cs-Ti heat pipes during 10 years' service on the lunar surface is acceptable because of the large operation design margin of the heat pipes (Fig. 13). The estimates of the C-C composite armor are incorporated in those of the total masses of the radiator modules as well as the areal density and specific power of a foldable radiator panel in Section 7.

6. Finite Element Stress Analyses of Heat Pipe Module and Panel During Launch

Spacecraft hardware or payload needs to survive the experienced stresses during launch from Earth, maneuvering in space, and landing on a target planetary body. A rocket launch exposes the payload to static and dynamic loads, both in the axial and lateral directions [52]. The upward motion of the launch vehicle as it climbs towards space transmits a static acceleration load in the axial direction. In addition, vibrations within the rocket transmit dynamic loads with low frequency sinusoidal oscillations and high frequency random vibrations in both the axial and lateral directions. These low frequency vibration loads are due to the transients during flight and impart acceleration to the payload [52, 53]. These low frequency acceleration loads have a sinusoidal profile with frequencies between 5 to 100 Hz and could cause the payload to bend and flex, inducing tensile and compressive stresses within its structure. The frequencies between 5 -100 Hz cover the first few vibration modes for most hardware and are typically associated with the greatest level of deformation and highest induced stress [54].

The high frequency random vibration loads are imparted both directly through the launch vehicle's payload interface. These loads are caused by acoustic pressure waves within the payload fairing [52]. These impart acceleration loads to the payload with random frequencies from 120 Hz and up to 8000 Hz. These loads typically produce lower displacements than the low frequency vibration loads, and hence lower induced stresses within the structure [52, 54]. The lower induced stresses make the high frequency loads of lower concern for most space hardware [54]. The high frequency vibrations, however, may be of concern to some components such as delicate scientific instruments.

The acceleration load profile for a given launch vehicle indicates how the load varies with the vibration frequency. Fig. 21 plots the reported low frequency vibration loads in the lateral direction for two heavy lift launch vehicles: the SpaceX Falcon Heavy [55] and the United Launch Alliance Delta IV Heavy [56]. These Heavy lift launch vehicles are representative of the class of rockets that would be used to launch future space nuclear power systems. They can launch payloads of up to 14,222 - 26,700 kg into orbit [55-56]. The acceleration load reported for the Falcon Heavy is 0.5 g, at a frequency from 5 Hz up to 85 Hz, and could increase to up to 0.6 g at 100 Hz [55]. The oscillatory load reported for Delta IV Heavy is greater than that for the Falcon Heavy, with constant load amplitude of 0.7 g at frequencies from 5 to 100 Hz [56].

Designers investigate the structural integrity of a spacecraft and its components for launch conditions using two primary methods: (a) experimental testing of hardware using vibration table tests, and (b) modeling and simulation using 3-D solid stress analysis and statistical failure models. The experimental testing method involves attaching the hardware to a vibration table with a platform that replicates the acceleration loads and frequencies for the chosen launch vehicle. Vibration testing for the low frequency loads involves gradually increasing the frequency of the oscillations from 5 Hz up to 100 Hz. The table's motion is controlled to match the acceleration load for the launch vehicle as the frequency is increased. Success is determined by whether the hardware survives vibration testing without damage or degradation [52, 53]. Degradation is measured by comparing the performance of electronic and mechanical components before and after vibration testing.

Simulations of launch vibration loads use 3-D Finite Element solid stress Analysis (FEA) methods and stochastic statistical energy analysis models, depending on the frequency range of the modeled vibrations [52]. FEA methods simulate the motion and displacement of the structure in response to applied loads [52, 57]. The calculated displacement is then used to calculate the stress tensor over the discretized mesh from which the induced tensile, compressive, and Von Mises stresses are determined. The calculated stresses are then compared to failure criteria for the structural materials to determine if damage could potentially occur. FEA methods have been proven to accurately predict the structural behavior for low

frequency (5-100 Hz) launch vibration loads [52]. However, they do not perform well for predicting structural response to high frequency launch vibration and acoustic loads. Instead, Statistical Energy Analysis (SEA) models are preferred for estimating the effects of the high frequency launch vibration loads on spacecraft components [52, 58]. These SEA models do not solve the detailed equations of motion across a discretized mesh but instead use a simplified approach for analyzing the average flow of energy through the structure using sets of linear equations. The SEA methods estimate the average structural response to the calculated average energy distributions using statistical assumptions based on prior experimental results for similar structures [58]. As the 5 -100 Hz frequency launch vibration loads are the most significant sources of induced stress for most spacecraft components during launch. The present work uses FEA methods to evaluate induced stresses in the developed heat pipe radiator panel in Fig. 9 during launch.

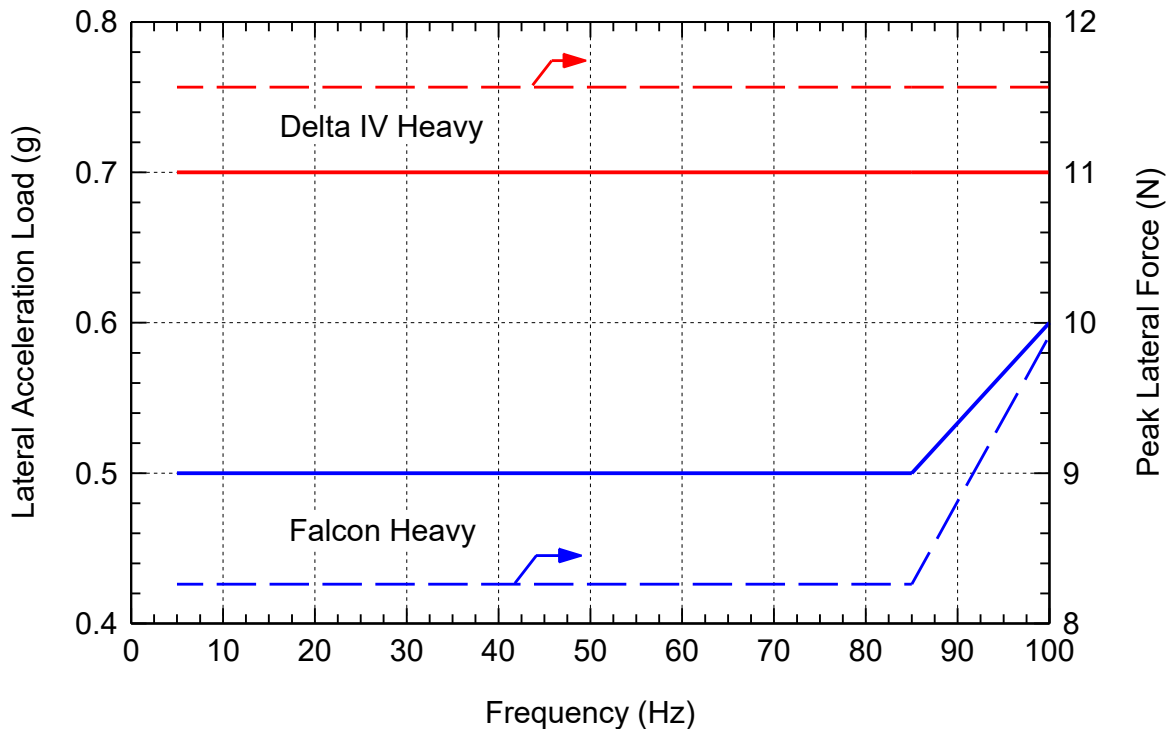


Figure 21: Lateral sinusoidal acceleration loads experienced by payloads onboard the Falcon Heavy and Delta IV Heavy launch vehicles [55, 56].

6.1 Approach

The performed vibrational stress analyses for a radiator panel comprising ten of the lightest Ver. 7 Cs-Ti heat pipe radiator modules (Fig. 6) evaluate the induced stresses at low frequency launch vibration loads during launch. The FEA simulates these acceleration loads with frequencies between 5 and 100 Hz for the Falcon Heavy and Delta IV Heavy launch vehicles (Fig. 21) [55, 56]. The performed simulations use the finite element solid stress modeling capability in the STAR-CCM+ commercial multiphysics code [28]. They calculate the induced tensile, compressive, and Von Mises stresses in the alloy walls of the Cs-Ti heat pipes and the liquid NaK-78 flow duct (Figs. 5, 8), the Ti-clad HOPG heat spreading fins, and the C-C composite armor. The estimated stresses are compared to the failure criteria of the materials to determine if they are within safe limits. The performed sensitivity analysis determines the numerical mesh refinement needed for convergence of the calculated values of the

displacement and stresses. The launch vibration analyses using the selected mesh grid refinement simulate the launch loads for a single heat pipe radiator module and an integrated radiator panel of ten heat pipe modules. The next section describes the methodology used for the performed FEA simulations to estimate induced stresses for the Ver. 7 heat pipe radiator module and panel during launch.

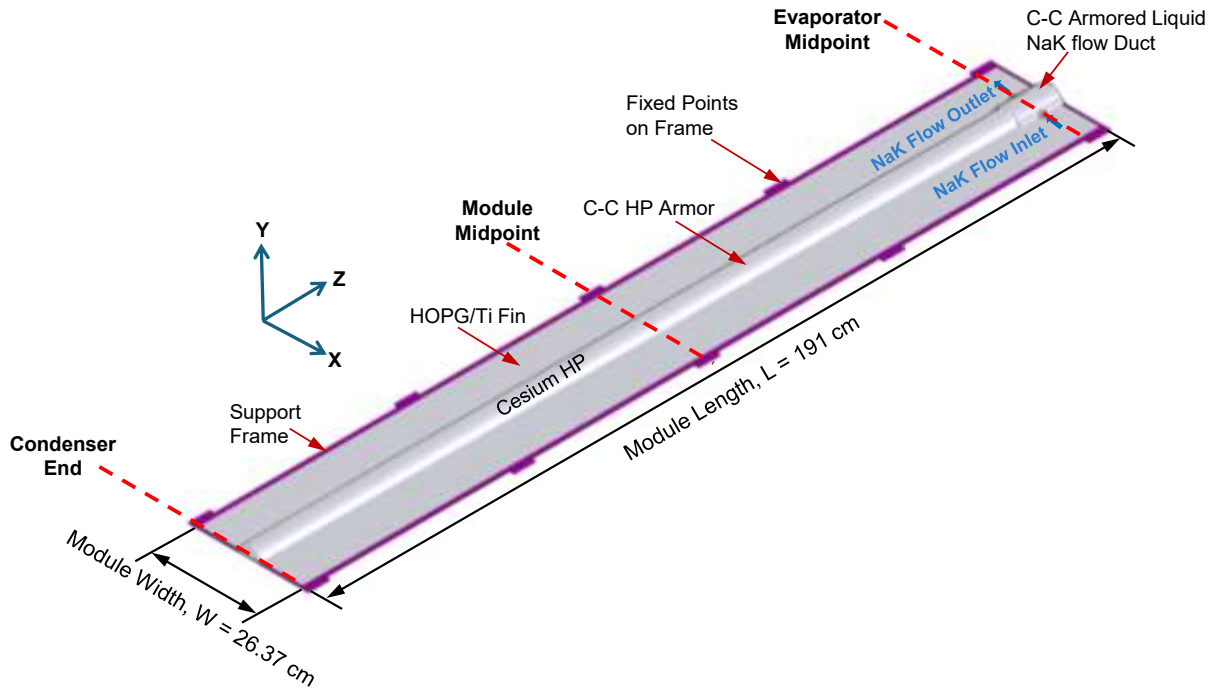


Figure 22: Single Ver. 7 heat pipe module in metal support frame used in the performed FEA of the induced solid stresses.

6.2 Analyses Methodology

The performed solid stress analyses use the STAR-CCM+ Multiphysics commercial code [28] to simulate the responses of Ver. 7 heat pipe radiator module and the radiator panel of ten modules with metal support frames during launch. These structures would be stowed within the payload bay of the launch vehicle in the vertical orientation with the heat pipe condenser section pointing downward (in the $-Z$ direction in Fig. 22) and both the evaporator section and the liquid NaK-78 flow duct pointing upward (In the $+Z$ direction in Fig. 22). The simulations model the effects of the low frequency (5-100 Hz) vibration loads reported for the Falcon Heavy [55] and the Delta IV Heavy [56] heavy launch vehicles (Fig. 21).

The vibration acceleration loads are input into the STAR-CCM+ code simulations as sinusoidal functions of time with the load applied to the body of the heat pipe radiator modules. The loads are applied in the normal direction to the vertically oriented rectangular heat pipe radiator modules (The Y-axis in Fig. 22). This orientation is selected as the resulting lateral force vector will produce the greatest displacements of the modules within the radiator panel.

The heat pipe modules are fixed at attachment points along the edges of the support frame (Fig. 22) of the panel (Fig. 9). These points represent the locations where the radiator panel will be tied down when folded and stowed during launch. The simulations neglect the effects of the surrounding air within the payload fairings of the launch vehicles of interest. This is a conservative assumption as the presence of air would dampen induced vibrations in the

lightweight structure of the radiator modules and panel [52]. The performed transient simulations use a time step of 0.5 ms with 10 inner iterations per timestep.

The material properties of the high strength Grade 5 titanium alloy (Ti-6Al-4V) of the Cs heat pipe wall, the NaK-78 flow duct walls, and the metal support frame and casing of the HOPG heat spreading fins, and C-C composite armor are input into the STAR-CCM+ simulation [58-59]. These properties are evaluated at room temperature as the heat pipe radiator panels would be launched with the fission reactor power system shut down in a cold state. The finite element solid stress model calculates the displacement of the structure during sinusoidal oscillations of the simulated transient loading, as well as the induced tensile, compressive, and Von Mises stresses. The tensile stresses have positive values and are determined from the λ_0 eigenvalue of the calculated stress tensor by the STAR-CCM+ commercial code [28]. The compressive stresses have negative values and are determined from the λ_2 eigenvalue of the calculated stress tensor.

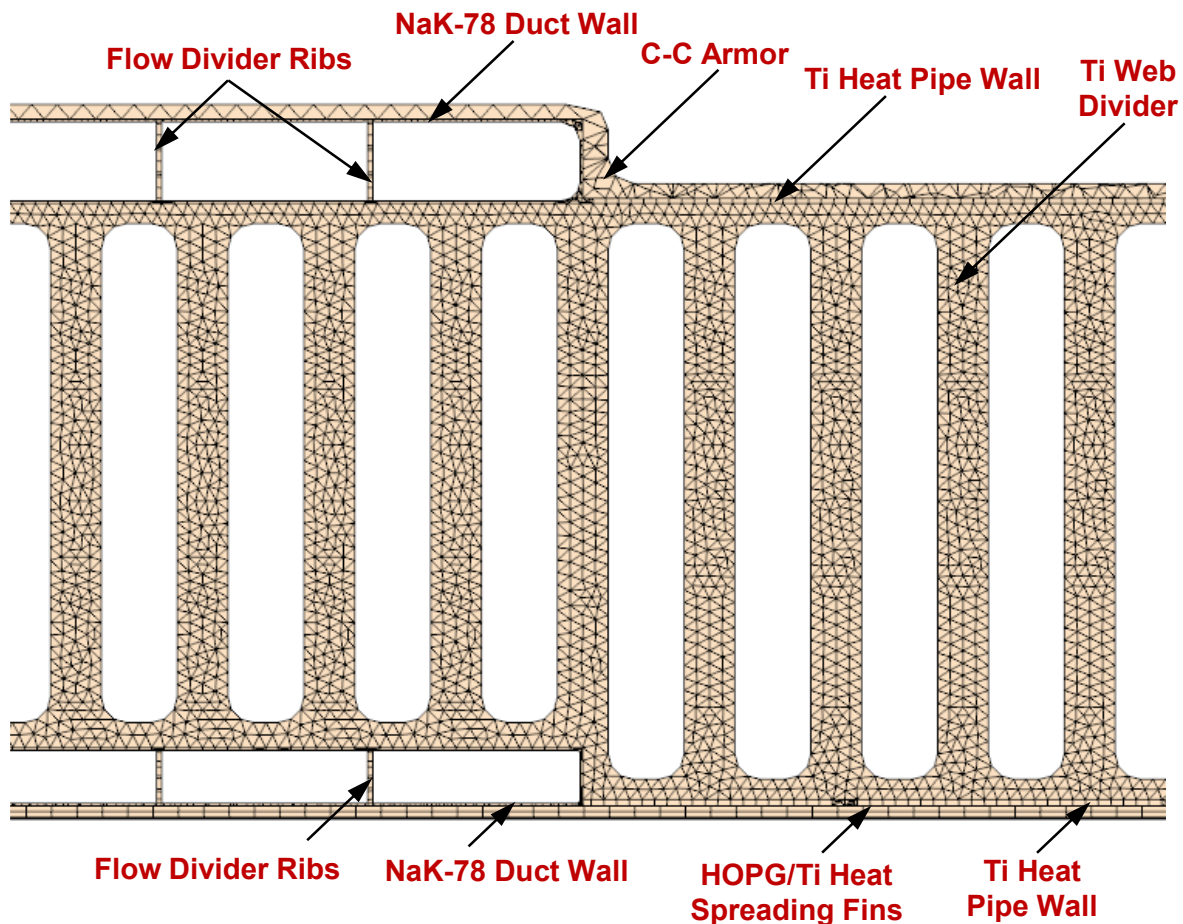


Figure 23: Section view of the numerical mesh grid used in performed sensitivity analysis for Ver. 7 heat pipe module (Fig. 5a).

6.3. Numerical Meshing and Sensitivity Analysis

The numerical mesh grid for the heat pipe radiator modules and panel uses the tetrahedral mesher with the thin mesher option. The thin mesher generates a single prismatic layer in the thin-walled geometries within the heat pipe radiator module. Fig. 23 shows a close-up view of the numerical mesh grid used for performed stress analysis of the heat pipe radiator

modules. The meshing utility in STAR-CCM+ independently meshes each part within the heat pipe radiator panel. The bonded boundaries of the meshed parts use mapped contact interfaces. The STAR-CCM+ code converts the generated finite volume mesh cells to a finite element cell with a maximum tetrahedral size of 4×10^{-4} m to perform the solid stress analyses.

A mesh sensitivity analysis investigates the effect of the numerical mesh refinement on the calculated induced stresses within a single Ver. 7 heat pipe radiator module and the corresponding computation cost. Table 9 lists the numerical mesh parameters for the four refinements considered, labeled Meshes 1 to 4. The finest Mesh 1 has a base cell surface size of 0.01 m, while the coarsest Mesh 4 has a base surface cell size of 0.025 m. The tetrahedral mesher in STAR-CCM+ code is allowed to vary the surface cell size of the tetrahedral elements from the maximum base size down to a minimum of 5% of the base size. Table 9 lists the number of mesh elements generated using these four mesh cell sizes for the Ti alloy frame, the walls of the Cs-Ti heat pipe, the HOPG layer in the heat spreading fins, and in the C-C composite armor.

The total number of mesh elements for the finest Mesh 1, is 13.45 million, including 0.39 million elements in the Ti frame, 7.23 million elements in the Ti HP wall, 0.95 million elements in the HOPG layer, and 4.88 million elements in the C-C composite armor. The generated finite element mesh of the radiator panel includes 0.18 million vertices in the Ti frame, 7.17 million vertices in the Ti HP wall and fins, 0.95 million vertices in the HOPG layer, and 2.26 million vertices in the C-C composite armor.

Meshes 2, 3, and 4 increase the base surface cell size to 0.015, 0.02, and 0.025 m, respectively. The larger base cell size reduces the total number of cell elements in the numerical mesh gride (Table 9). The total number of mesh cells or elements decreases from 13.45 million for Mesh 1 down to 4.81 million, 2.80 million, and 1.86 million for Meshes 2, 3, and 4, respectively. Consequently, the density of the numerical mesh elements increases rapidly with increased mesh refinement (Table 9).

Table 9. Numerical Mesh Parameters for Mesh Sensitivity Analysis of Ver. 7 Heat Pipe Module.

Region	Numerical Mesh Elements Tally			
	Finest: 1	Fine: 2	Coarse: 3	Coarsest: 4
Base Cell Size (m)	0.01	0.015	0.02	0.025
Frame Cells	0.39m	1.35m	0.069m	0.046m
Ti HP Cells	7.24m	3.25m	1.86m	1.26m
HOPG Cells	0.94m	0.42m	0.24m	0.15m
C-C Armor Cells	4.88m	1.01m	0.60m	0.40m
Total Cells	13.45m	4.81m	2.80m	1.86m

The implemented FEA model of the lateral vibration load in the Y-direction (Fig. 22) is for the Falcon Heavy launch vehicle at a frequency of 5 Hz (Figs. 24 and 25). At this frequency, the lateral acceleration load for the heat pipe modules is 0.5 g. The results in Figs. 24 and 25 show side images of the calculated Von Mises stresses along the inner surface of the Ti wall of the Cs heat pipe and the liquid NaK-78 flow ducts surrounding the heat pipe evaporator (Figs. 5 and 8).

The images of the stresses displayed in these figures are those at the time when the induced stress and displacement are highest. The highest induced stresses within the Ti walls of the heat pipe and NaK-78 flow duct concentrate at the ends of the heat pipe sections and

the NaK-78 flow duct around the evaporator (Figs. 24 and 25). The highest induced stresses also occur along the bottom of the heat pipe condenser where the titanium cross support bars in the frame of the radiator panel are in contact with the bottom of the heat pipe module during the simulated launch oscillations.

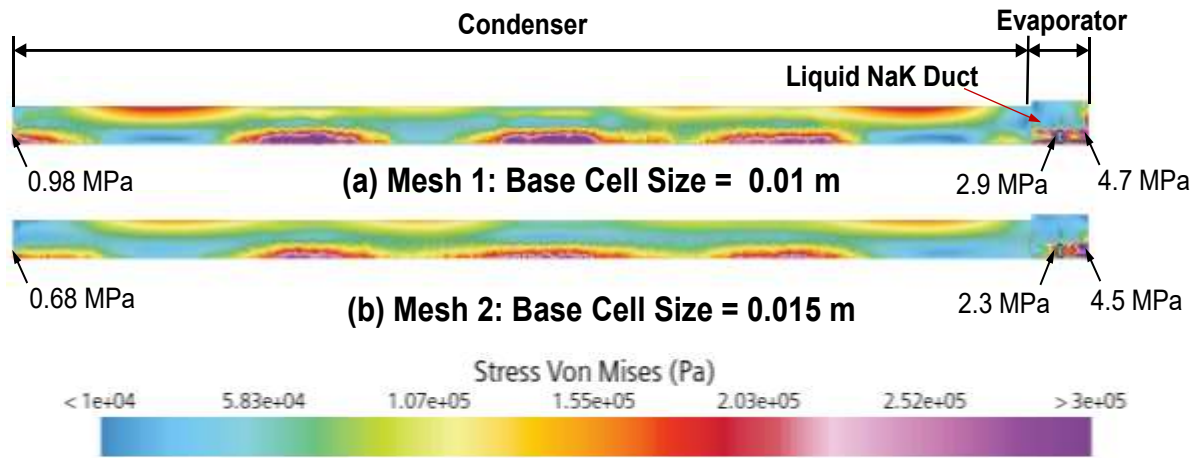


Figure 24: Images of the induced Von Mises stress along the inner surface of the Ti wall of the Cs-Ti heat pipe and NaK-78 flow duct of Ver. 7 module with Meshes 1 and 2 and for 5 Hz lateral vibration load.

Figures 26 and 27 show enlarged images of the calculated Von Mises stress along the inner surface of the Ti walls of the Cs heat pipe, at the ends of the heat pipe evaporator and condenser sections. The highest stress in the heat pipe condenser wall occurs at the lower corners of the half-cylindrical heat pipe. The highest stresses in the liquid NaK-78 flow duct occur where the circular flow header joins the flat surface at the end of the heat pipe (Figs. 8, 26 and 27). High stress also concentrates where the inlet and outlet flow of the ducts join with the circular flow headers on either side of the duct (Fig. 8). The calculated Von Mises stresses for the rest of the Ti heat pipe wall are much lower than the high stresses at these locations (Figs. 24-27).

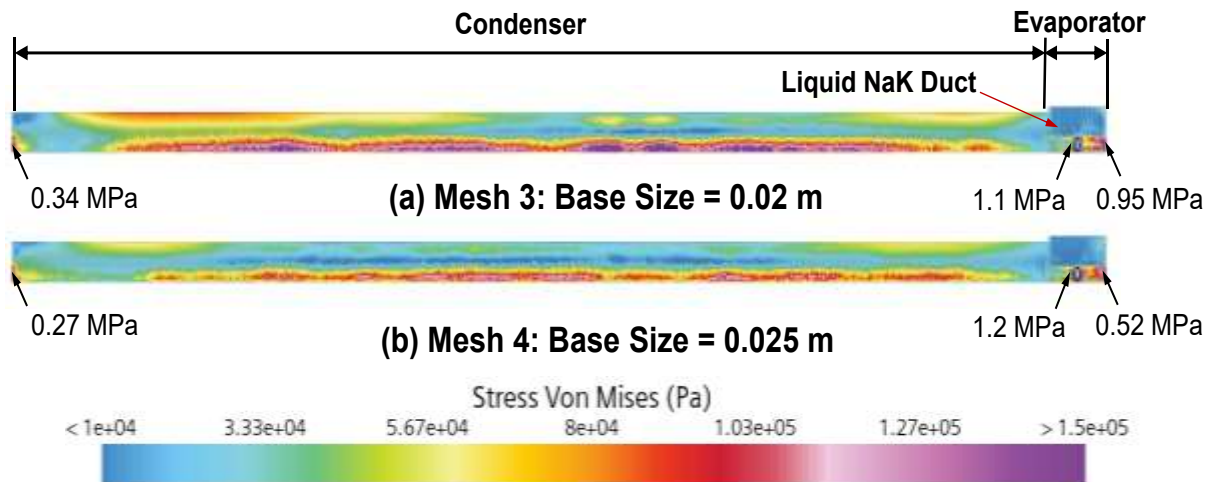


Figure 25: Images of the calculated Von Mises stresses along the inner surface of the Ti wall of the Cs-Ti heat pipe and NaK-78 flow duct of Ver. 7 module with Meshes 3 and 4 and for 5 Hz lateral vibration load.

The calculated highest stress for the heat pipe module using the finest Mesh 1 reaches 4.7 MPa at the end of the circular header for the NaK-78 flow duct (Figs. 24a and 26a). The highest stress calculated with Mesh 2 is 4.5 MPa at the same location (Figs. 24b and 26b). The highest Von Mises stress for the heat pipe modules of 1.1 MPa is calculated using the coarse Mesh 3 (Figs. 25a and 27a) compared to 1.2 MPa using the coarsest Mesh 4 (Figs. 25b and 27b). The stresses calculated at the end of the heat pipe condenser are lower than those at the end of the evaporator, reaching 0.98 MPa for Mesh 1, 0.68 MPa for Mesh 2, 0.34 MPa for Mesh 3, and 0.27 MPa for Mesh 4 (Figs. 24-27).

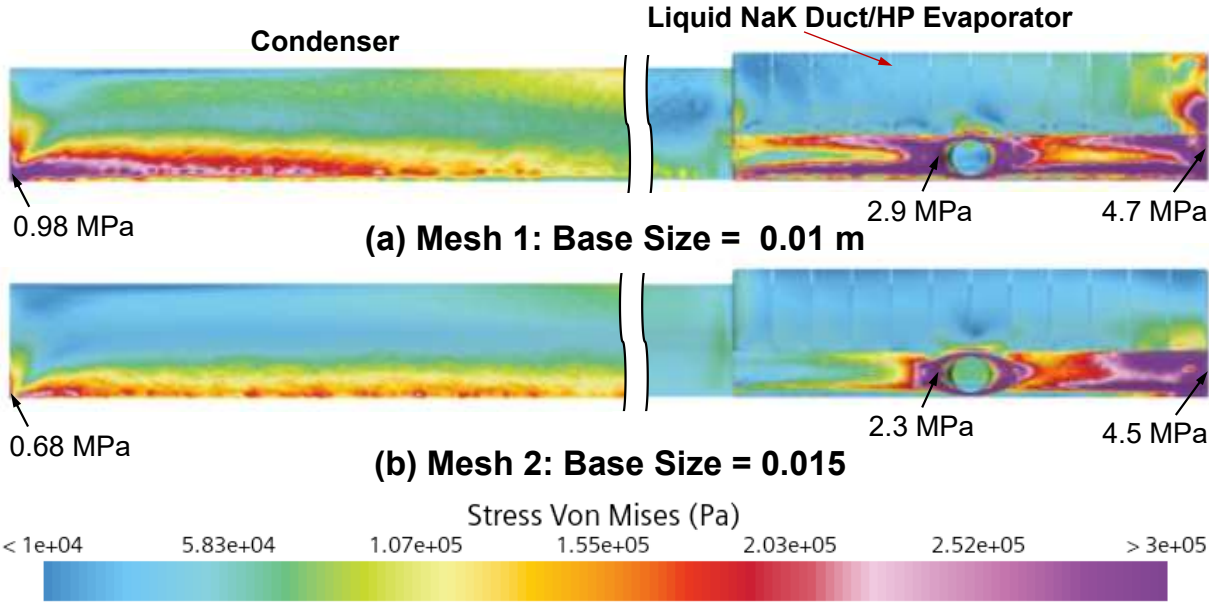


Figure 26: Enlarged images of the calculated Von Mises stress at the ends of the Cs-Ti heat pipe in Fig. 24 using Meshes 1 and 2 for 5 Hz lateral vibration load.

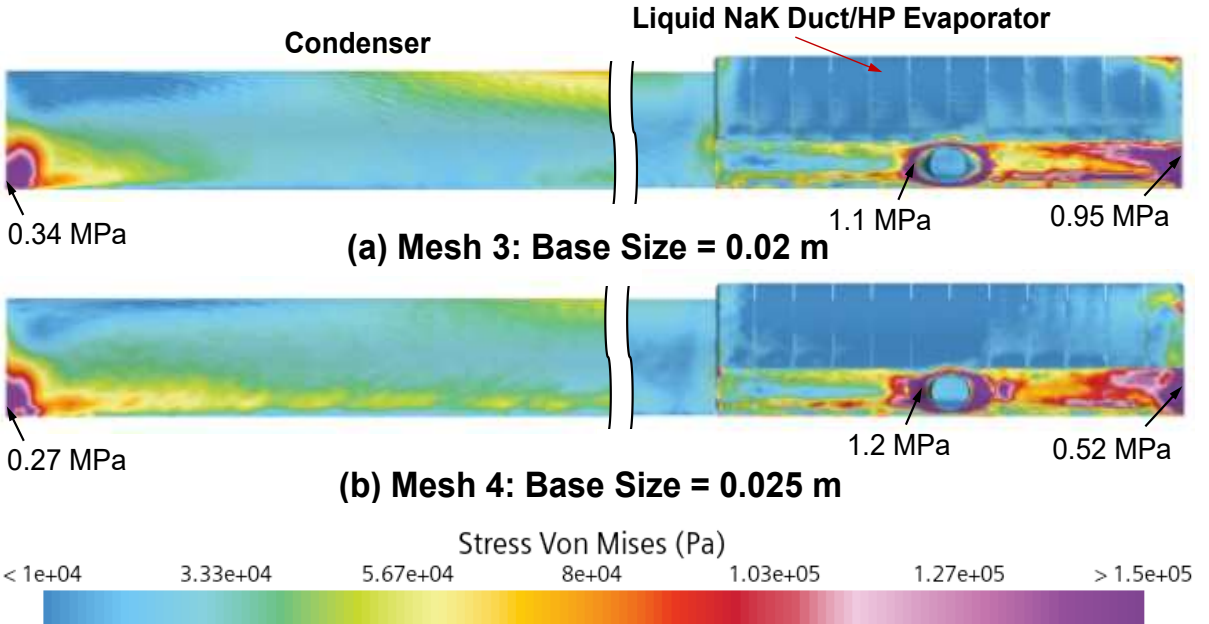


Figure 27: Enlarged views of Von Mises stress for the ends of the Cs-Ti heat pipe in Fig. 25 for Meshes 3 and 4 with 5 Hz lateral vibration load.

The mesh sensitivity analysis shows that the highest calculated stress in the Ti heat pipe wall and NaK-78 flow duct are only 4.4% higher for the finest Mesh 1 compared to those for Mesh 2, despite Mesh 1 having 222.7% more mesh cells (Fig. 28). The calculated stresses for the two coarser mesh settings resulted in much lower calculated stresses within the heat pipe radiator module. The calculated highest Von Mises stress of 4.7 MPa is also far below the yield stress of 898 MPa for the Grade 5 Ti structural alloy. The differences in the calculated stresses in the metal support frame and the C-C armor for Meshes 1 and 2 are also much lower than the strengths for those materials. *Therefore, the meshing settings for the fine Mesh 2 are selected for modeling the heat pipe radiator modules and panels to reduce the overall computational cost for the finite element solid stress analysis with insignificant effect on the calculated results.*

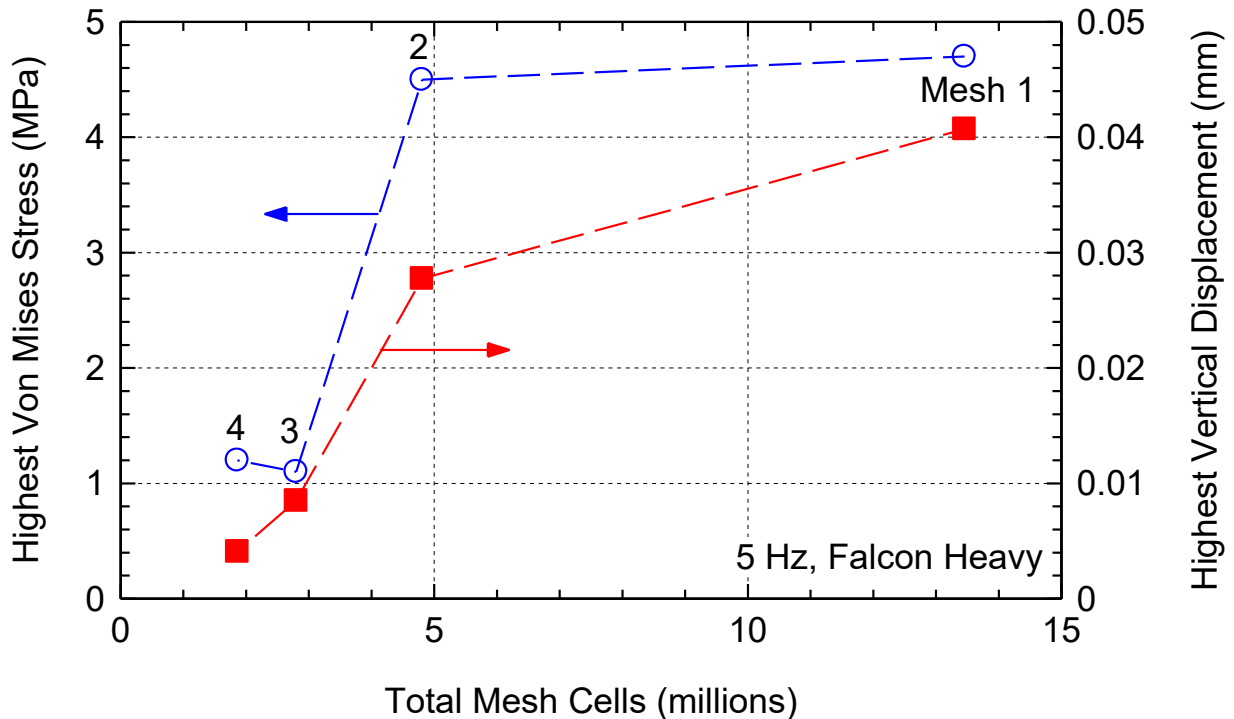


Figure 28: Effect of the number of mesh gride cells on the highest calculated Von Mises stress and vertical displacement for the Ver. 7 heat pipe module.

6.4. Single HP radiator module stress analyses

The performed analysis for a single Ver. 7 heat pipe radiator module calculates the launch stresses for the lateral vibration loads of the Falcon Heavy and Delta IV Heavy launch vehicles at 5, 50, and 100 Hz. Figs. 29a and b plot the estimated vertical displacements for frequencies of 5 Hz and 100 Hz, respectively, at the axial midpoint of the module, the middle of the heat pipe condenser, and the end of the evaporator (Fig. 22). The results displayed in Fig. 29 are when the calculated displacement is maximum. The displacement increases inward from the lateral edges of the HOPG/Ti fins. It is flattened in the middle where the hemispherical heat pipe with center Ti support webbing has greater resistance to bending from the vibration load. The displacement is highest at the module’s midpoint, and much lower at the end of the condenser and within the Ti heat pipe evaporator and NaK-78 duct (Figs. 29a and b).

The single Ver. 7 heat pipe module vibrates in its fundamental mode for frequencies between 5 and 100 Hz. The highest displacement for the heat pipe module increases with increased frequency from 5 Hz to 100 Hz (Figs. 29a and b). The maximum displacement at 100

Hz is 2.78 times that at 5 Hz frequency for the vibration load of the Falcon Heavy and 2.32 times greater for the vibration load of the Delta IV Heavy. The higher acceleration load for the Delta IV Heavy launch vehicle for the Falcon Heavy (Fig. 21), results in larger displacement within the Ver. 7 heat pipe module (Fig. 29). The flexing of the heat pipe radiator module induces stresses within its structural materials. The calculated stresses are used to evaluate potential damage to the structure of the Cs-Ti heat pipe module. Cracking or failure of the Ti heat pipe wall would vent the Cs working fluid into space, ceasing the heat pipe's operation. On the other hand, cracking in the HOPG layer in the HOPG/Ti fins may degrade the lateral thermal conductivity of the aligned graphene layers and increase the temperature drop along and across the fins.

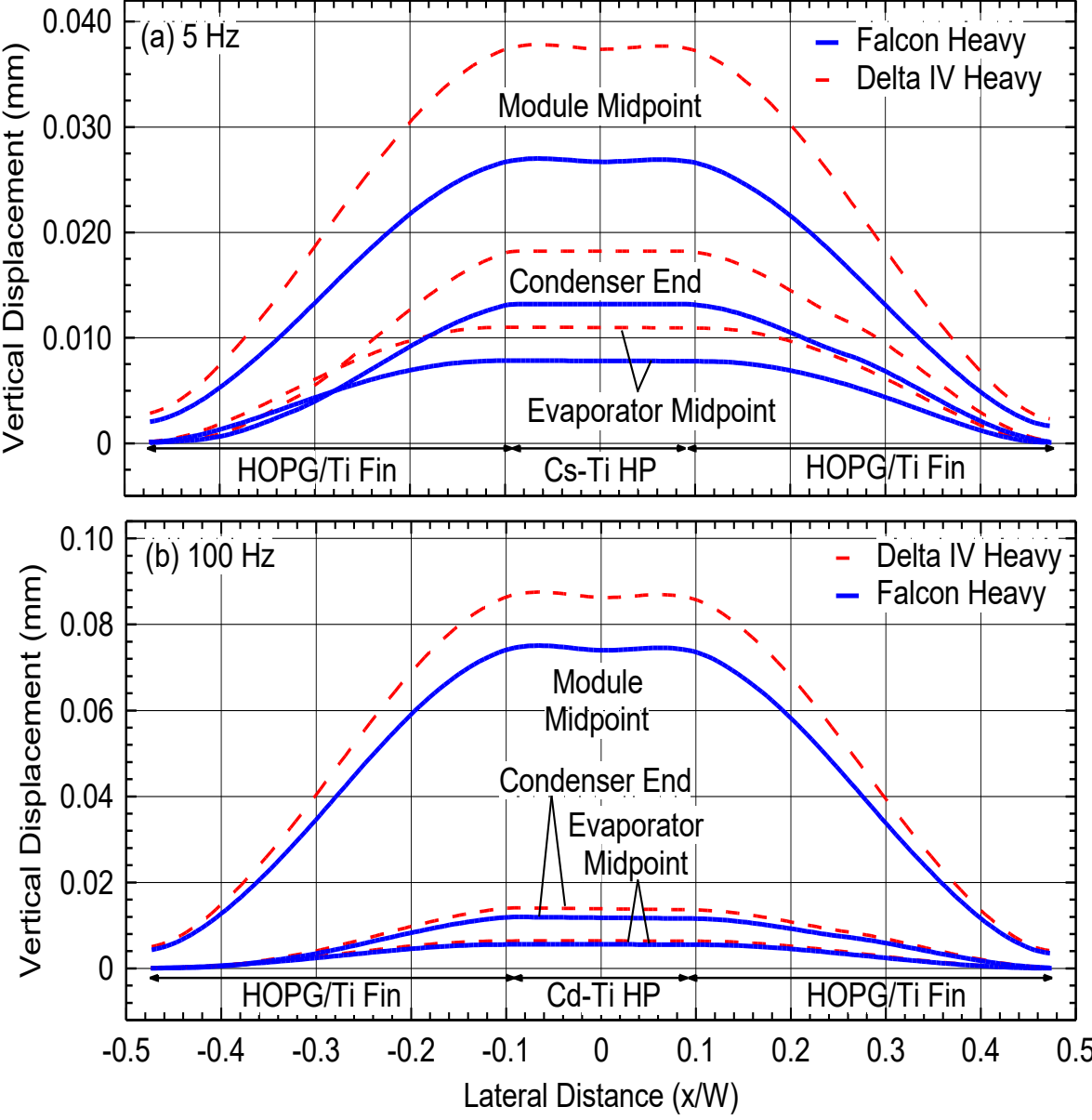


Figure 29: Calculated vertical displacement for the Ver. 7 heat pipe module for the lateral sinusoidal acceleration loads of the Falcon Heavy and Delta IV Heavy launch vehicles at 5 Hz and 100 Hz frequencies.

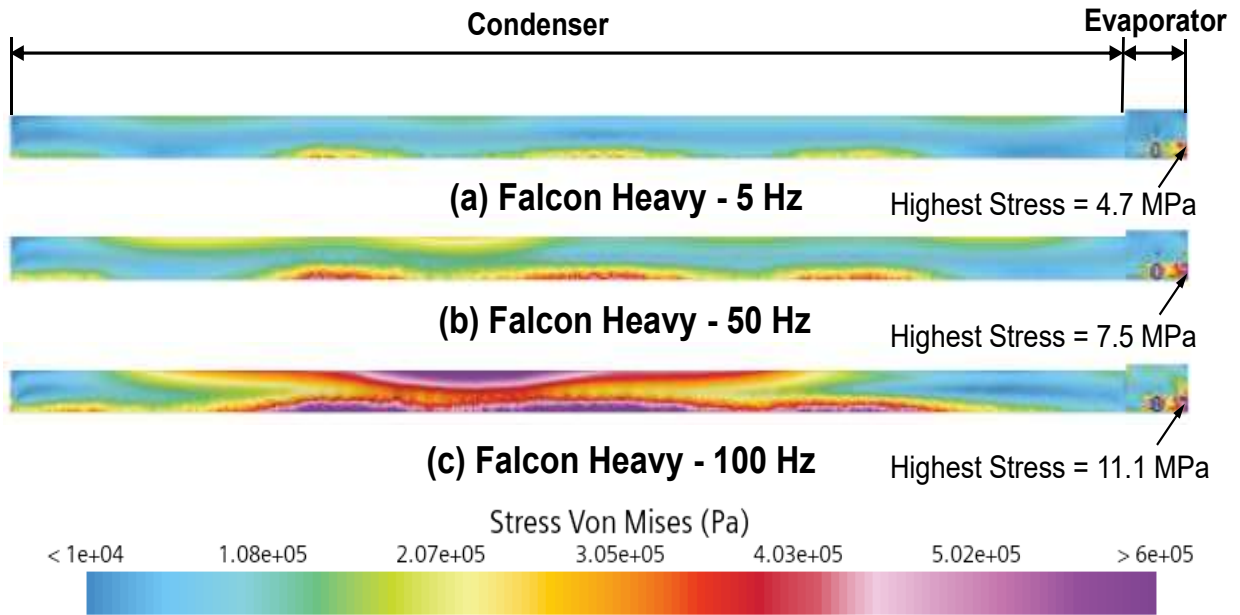


Figure 30: Image of the calculated Von Mises stress along the inner surface of the Ti wall of the Cs-Ti heat pipe and the NaK-78 flow duct of Ver. 7 heat pipe module for Falcon Heavy launch loads with frequencies of 5, 50, and 100 Hz (images not to scale).

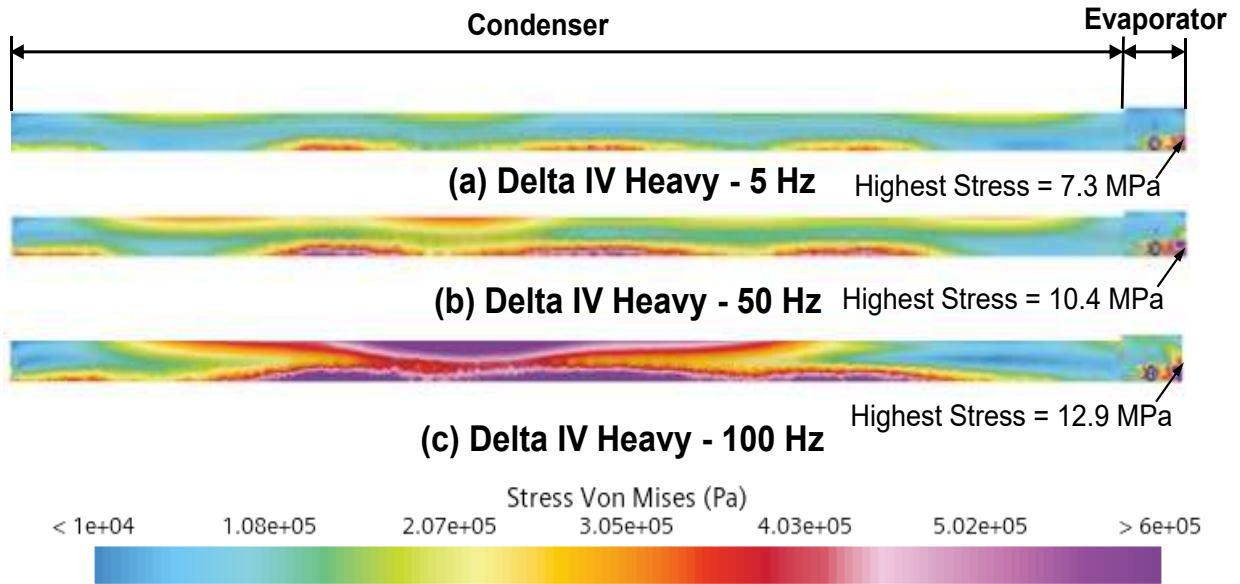


Figure 31: Calculated images on the induced Von Mises stress along the inner surface of the Ti wall of the Cs-Ti heat pipe and NaK-78 flow duct of Ver. 7 heat pipe module for Delta IV Heavy launch loads with frequencies of 5, 50, and 100 Hz (images not to scale).

Figs. 30-33 present the calculated Von Mises stresses along the inner surface of the Ti walls of the Cs-Ti heat pipe and NaK-78 duct of the Ver. 7 heat pipe module for the launch vibration loads of the Falcon Heavy (Figs. 30 and 32) and Delta IV Heavy (Figs. 31 and 33) at frequencies of 5, 50, and 100 Hz. Figs. 30 and 31 shows images of the calculated stress field for the heat pipe and the NaK-78 flow duct wall for the full length of the heat pipe. The highest

Von Mises stress is at the end of the evaporator section and the NaK-78 flow duct. Figs. 32 and 33 show enlarged images of the calculated Von Mises stresses for the ends of the heat pipe condenser and evaporator sections where stresses are highest.

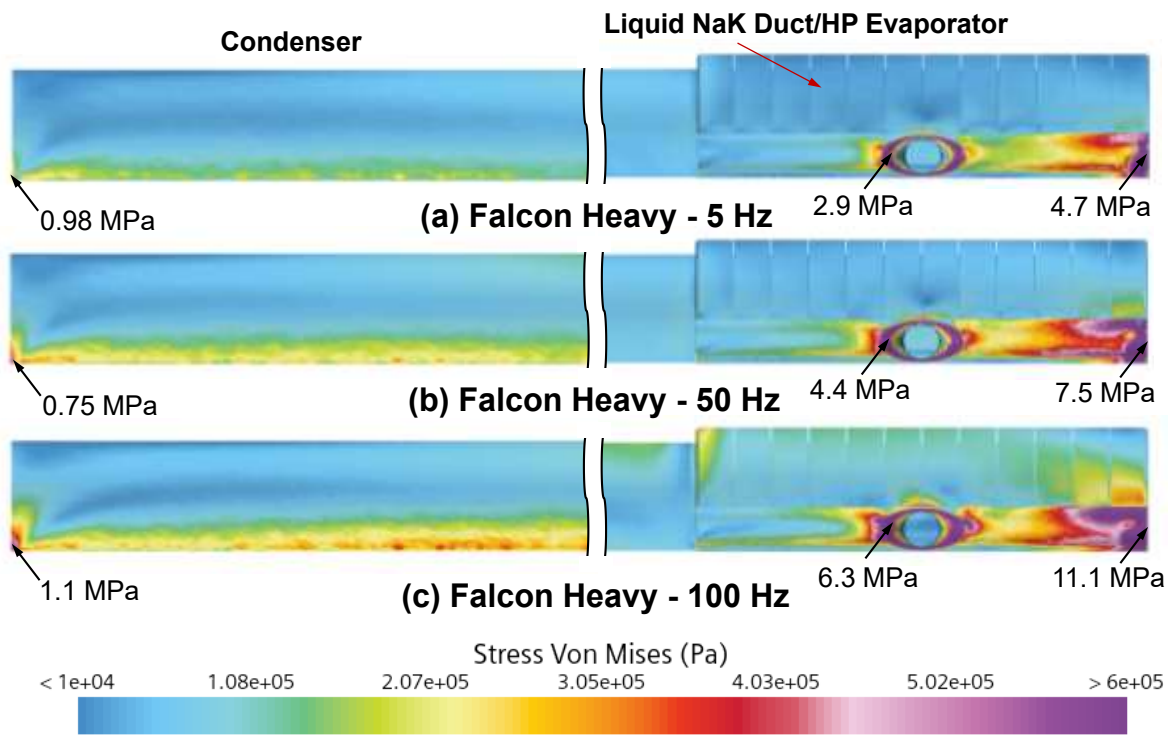


Figure 32: Enlarged images of the calculated Von Mises stress in the Ti wall of the Cs-Ti heat pipe and NaK-78 flow duct of Ver. 7 heat pipe module, at the ends of the Cs-Ti heat pipe in Fig. 30, for the Falcon Heavy acceleration loads.

The induced Von Mises stress in the thin Ti wall increases with increased load frequency. The highest Von Mises stress for the Falcon Heavy profile at the 100 Hz frequency is 11.1 MPa. This is 1.48 and 2.36 times the peak stress at 50 Hz and at 5 Hz, respectively (Figs. 30a-c). The higher acceleration loads of the Delta IV Heavy left vehicle result induce higher Von Mises stress than for the Falcon Heavy (Figs. 31a-c). The calculated peak Von Mises stress at 100 Hz for the Delta IV Heavy is 12.9 MPa. This is 1.24 and 1.76 times higher than the highest stresses at 50 and 5 Hz, respectively. Note that the stresses along the length of the heat pipe radiator module are much lower than the highest values at the ends of the heat pipe evaporator and condenser sections (Figs. 30-33).

The enlarged images in Figs. 32-33 show the calculated induced stresses at the ends of the evaporator and condenser of the Cs-Ti heat pipe radiator module. The highest Von Mises stress occurs within the Ti wall of the NaK-78 flow duct at the end of the HP evaporator section. Concentrated stresses also occur within the wall of the NaK-78 flow duct where the circular conduits of the inlet and outlet flow of the ducts join with the circular flow headers on either side of the duct (Fig. 8). Induced high stress also occurs within the Ti wall of the Cs heat pipe at the end of the condenser. They are up to 1.1 MPa for the Falcon Heavy and 1.5 MPa for the Delta IV Heavy (Figs. 32-33).

The Von Mises Yield Criteria [60] evaluates the safety limit for the ductile Ti walls of the heat pipe and the liquid NaK-78 flow duct. This limit is reached when the induced Von Mises stress equals the yield strength of the wall material. For launches at ambient room

temperature, the yield strength of the Ti-6Al-4V titanium alloy for the walls of the heat pipe radiator modules is 898 MPa [59]. The calculated induced Von Mises stresses within the Ti walls of the Cs heat pipe and the NaK-78 flow duct for a single Ver. 7 heat pipe radiator module are only ~ 1.2% of the yield strength of the Ti-6Al-4V titanium alloy.

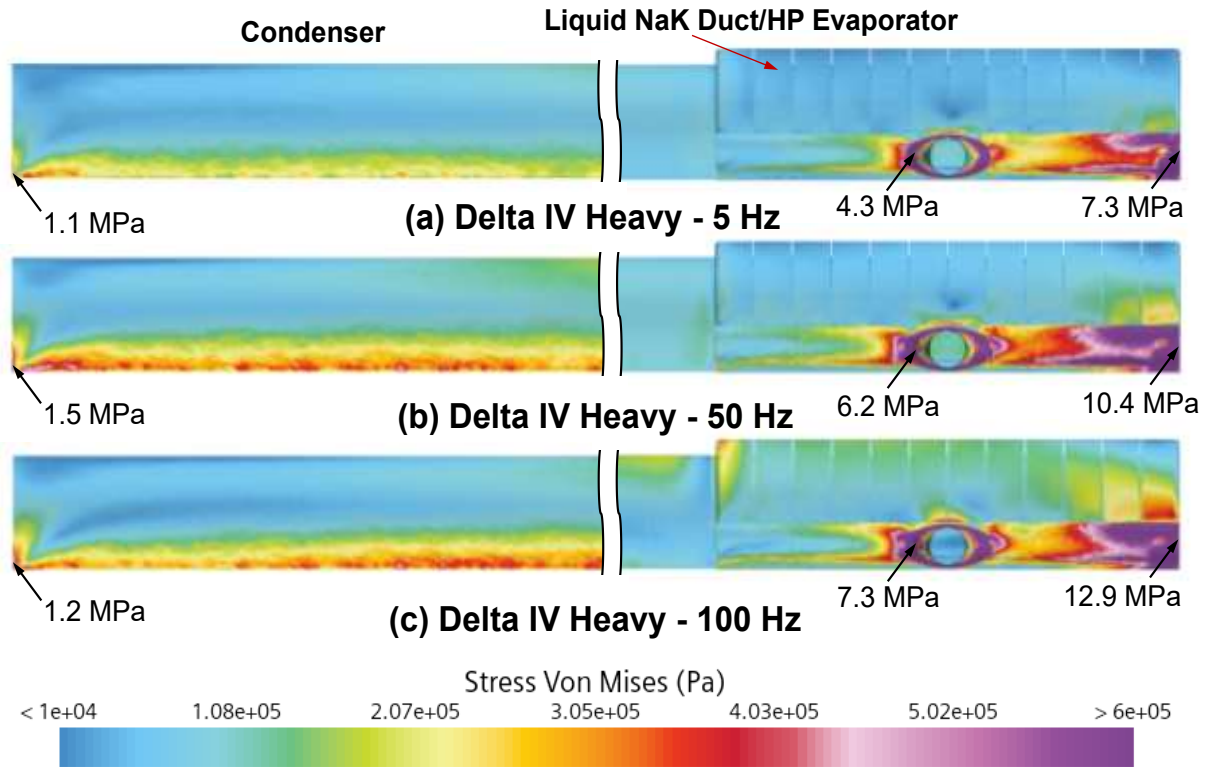


Figure 33: Enlarged views of induced Von Mises stresses in the Ti wall of the Cs-Ti heat pipe and NaK-78 flow duct of Ver. 7 heat pipe module at the ends of the Cs-Ti heat pipe in Fig. 31 for the Delta IV Heavy acceleration loads.

Figures 34 and 35 plot the induced Von Mises Stresses in the Ti cladding or casing of the HOPG/Ti heat spreading fins at vibration frequencies of 5 and 100 Hz for the launch loads of the Falcon Heavy and Delta IV Heavy vehicles. These stresses are at the same locations as the calculated displacement shown in Figs. 22 and 29. The induced highest stresses in the Ti cladding material exceed those calculated in the Cs heat pipe Ti wall. These high induced stresses are due to the flexing of the thin fins during the simulated launch vibration loads.

The induced Von Mises stress spikes at points along the HOPG/Ti fins on either side of the central Cs-Ti heat pipe (Figs. 34 and 35). The value of the induced stress is the same in the middle of the radiator modular. This is because the semi-cylindrical shape of the heat pipe helps resist bending compared to the flat HOPG/Ti fins. The highest induced stresses are calculated at the line cutting through the end of the heat pipe condenser section (Fig. 22). They are higher for the acceleration loads of the Delta IV heavy (Fig. 35) than for those of the Falcon Heavy (Fig. 34). Although higher than the calculated Von Mises stress for the heat pipe and duct walls, the induced stresses in the heat spreading fins are well below the yield strength of the titanium alloy wall.

Figure 36 presents the calculated values of the highest induced stress in the Ti heat pipe wall and in the HOPG layer of the HOPG/Ti fins at vibration frequencies of 5, 50, and 100 Hz and the launch loads for the Falcon Heavy and Delta IV Heavy launch vehicles. The induced

stresses in the 0.45 mm thick HOPG layer are much lower than those experienced in the thinner 0.2 mm thick heat pipe Ti wall. Although cracking the HOPG layer could degrade the high lateral conductivity for spreading the rejected waste heat along the 10 cm wide fins into space, the Ti casing could maintain the fins' structure integrity. Note that increasing the vibration frequency increases the induced tensile stress in the HOPG for the investigated load profiles for the two launch vehicles considered. The induced highest tensile stress onboard of the Falcon Heavy during launch is 1.6 MPa at a frequency of 100 Hz. The higher acceleration load for the Delta IV Heavy increases the calculated peak tensile stress to 3.2 MPa at 100 Hz.

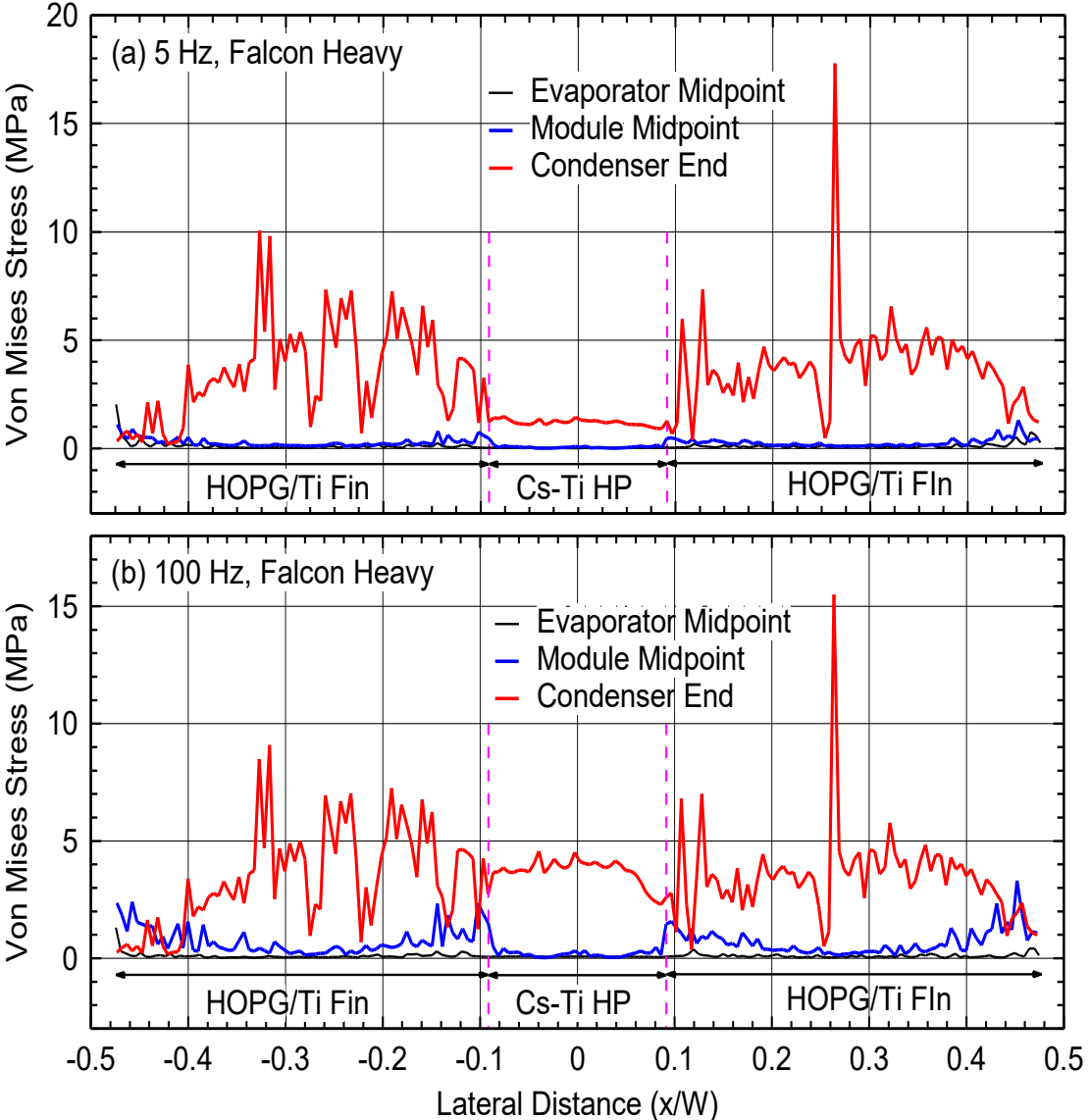


Figure 34: Plots of Von Mises stresses along the Ti cladding of the HOPG/Ti fins for the Ver. 7 heat pipe module due to the lateral sinusoidal acceleration loads of the Falcon Heavy launch vehicle at frequencies of 5 and 100 Hz.

The HOPG is a brittle material with anisotropic structural strength. The tensile and flexure strength of pyrolytic graphite in different orientations has been measured by Berry and Gebhardt [61]. They reported that the average tensile strength is ~ 122 MPa in the

perpendicular direction and ~ 124 MPa for the in-plane direction. The flexure strength is highly anisotropic, with an average failure strength of 161 MPa in the perpendicular direction and 134 MPa for the in-plane direction [61]. Ishihara et al. [62] proposed a pyrolytic graphite failure criterion for bending stresses of 1/3 of the material's tensile failure strength. During oscillations, the HOPG layer bends in the perpendicular direction to the aligned graphene layers. Thus, the flexure failure limit is determined as 53.7 MPa for the HOPG layer in the present analysis.

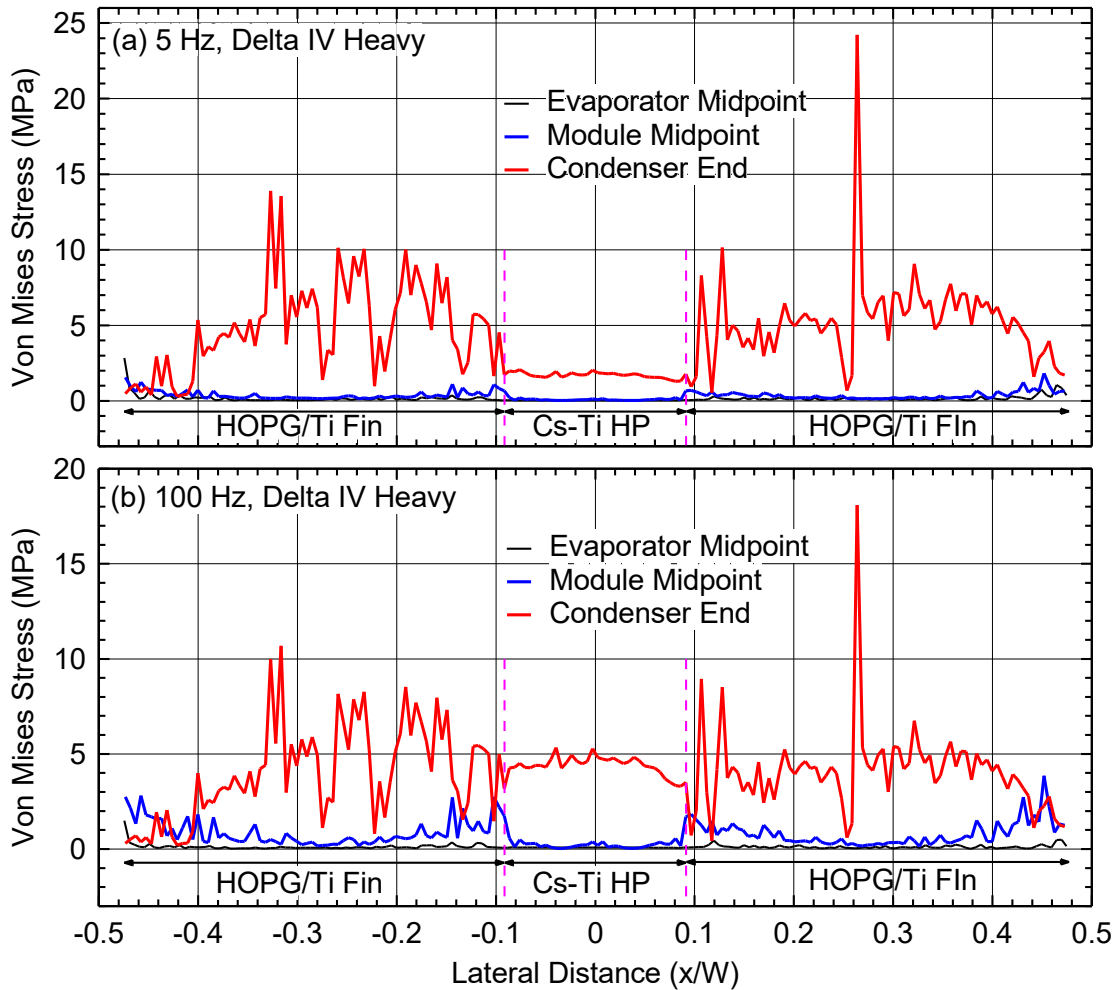


Figure 35: Plots of the calculated Von Mises stresses along the Ti cladding of the HOPG/Ti fins of Ver. 7 heat pipe radiator module, subject to the lateral sinusoidal acceleration loads of the Delta IV Heavy launch vehicle at frequencies of 5 Hz and 100 Hz.

The calculated induced peak stresses of 1.6 and 3.2 MPa for the two launch vehicles considered are significantly lower than the flexure failure limit of 53.7 MPa for the HOPG layer in the heat spreading fins of the radiator module (Fig. 36). This suggests that the HOPG layer in the heat spreading fins of the designed radiator module is unlikely to experience cracking when subjected to the 5 - 100 Hz frequency lateral sinusoidal launch loads. The calculated induced stresses for the Delta IV Heavy launch vehicle are consistently higher due to the higher lateral acceleration loads (Fig. 21). The difference in the calculated stresses among the two launch vehicles is minor, however, considering the large margin below the failure criteria of the structural materials in the Cs-Ti heat pipe radiator module. The next section presents the

results of the performed solid stress launch vibration analysis for an integrated radiator panel of ten-Ver. 7 heat pipe radiator modules (Fig. 37).

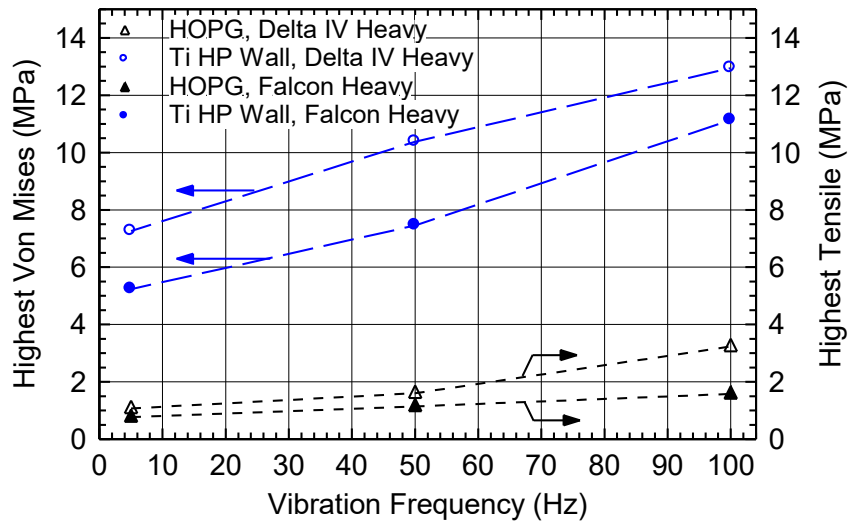


Figure 36: Highest calculated Von Mises stress in the Ti heat pipe wall and tensile stress in the HOPG layer of the heat spreading fins for a single Ver. 7 heat pipe radiator module versus vibration frequency of the lateral loads for Falcon Heavy and Delta IV Heavy launch vehicles.

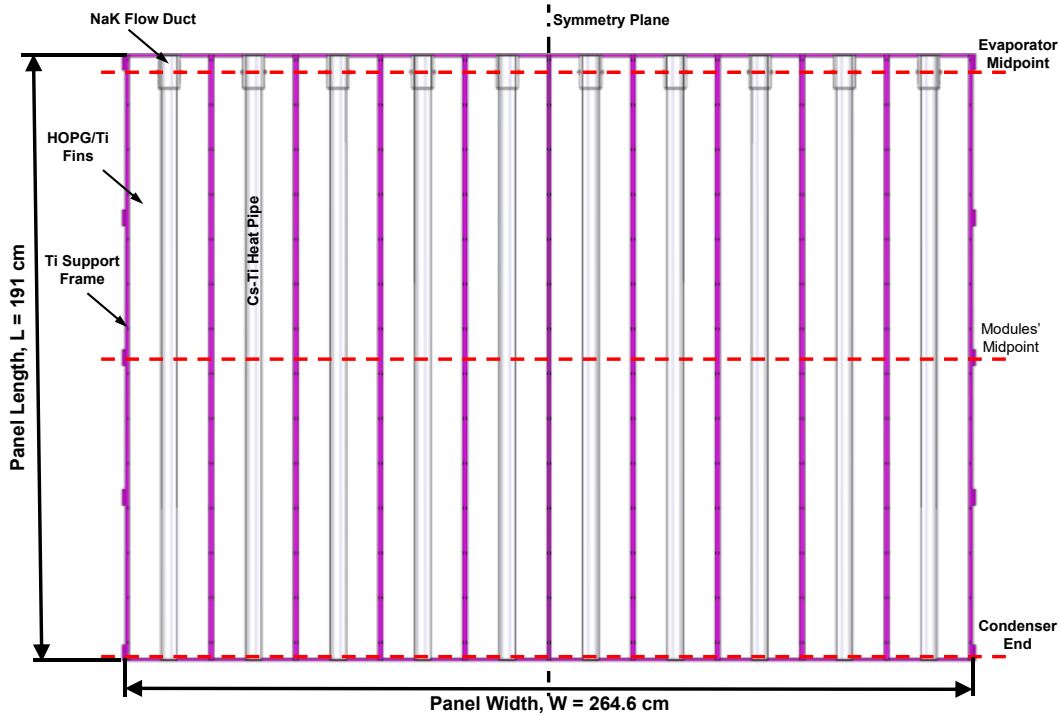


Figure 37: Integrated radiator panel of ten Ver. 7 heat pipe modules in support frame.

6.5. Launch vibration stress analysis of ten modules radiator panel

Launch vibration stress analyses are performed for a radiator panel of ten Ver. 7 modules (Fig. 37) subject to the launch acceleration loads of the Falcon Heavy launch vehicle. This is the primary heavy lift vehicle currently in service for US launches. The conducted FEA models

one half radiator panel of ten modules, with a symmetry plane along the middle (Fig. 37). Investigated is the effect of the launch vibration frequency on the highest induced stresses within the radiator panel structure (Fig. 37).

The results of the FEA show that the single Ver. 7 heat pipe module vibrates in the 1st, or for all load vibration frequencies considered, 5 - 100 Hz. However, the vibration mode for the ten-modules radiator panel (Fig. 37) depends on the vibration frequency. At 5 and 25 Hz the radiator panel vibrates in the 1st mode, in the 2nd mode at 50 Hz and in the 3rd mode at the higher frequencies of 75 and 100 Hz. During the sinusoidal oscillations, the higher vibration modes decrease the maximum displacements in the radiator panel, which are much lower for the lower vibration frequencies of 5 - 50 Hz (Fig. 38).

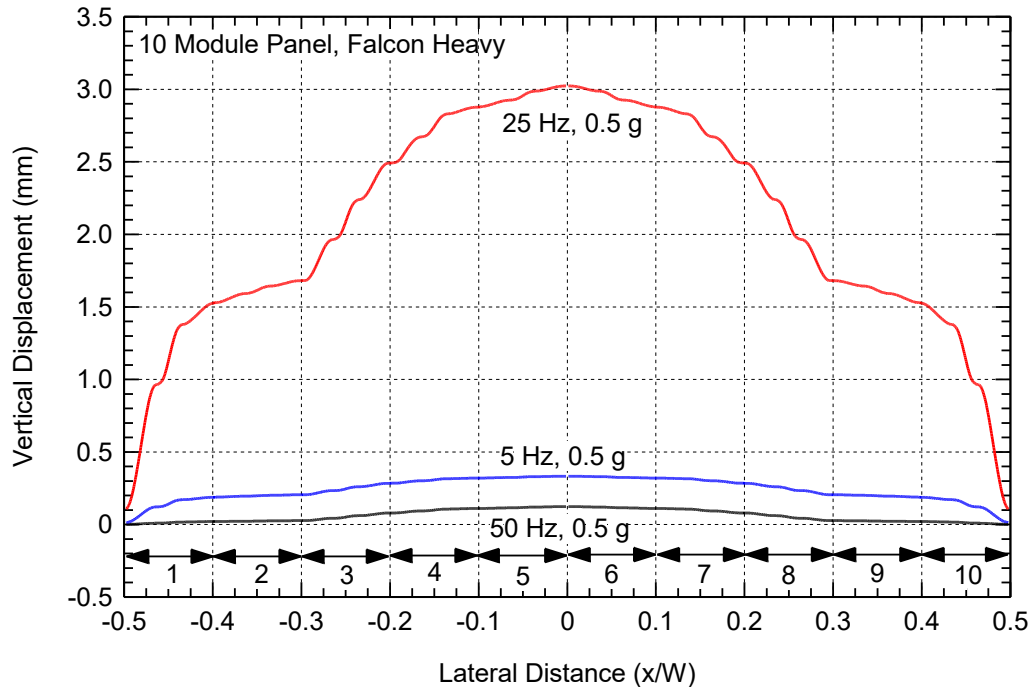


Figure 38: Calculated vertical displacement along midpoint of radiator panel with ten Ver. 7 heat pipe modules subject to the launch loads of the Falcon Heavy at 5, 25, and 50 Hz.

Figure 38 compares the calculated vertical displacements along the midpoint for the ten-module radiator panel at vibration frequencies of 5, 25, and 50 Hz at an acceleration load of 0.5 g (Fig. 21). The displacements for the panel of ten-Ver. 7 modules are much higher than those calculated for the single Ver. 7 module (Figs. 29 and 38). The maximum vertical displacement occurring at the symmetry plane of the radiator panel is 3.0 mm at 25 Hz for the Falcon Heavy launch vehicle. At 5 and 50 Hz, the calculated maximum displacement is only 11% and 4%, respectively, of that at 25 Hz (Fig. 38). The ten-modules panel does not flex in a perfect sinusoidal shape, but instead it experiences bending along the metal support frames between the adjacent radiator modules within the panel (Fig. 37).

Figures 39 - 41 plot the induced Von Mises stresses in the Ti walls of the Cs heat pipe and the NaK-78 flow duct around the evaporator section, and in the Ti cladding of the HOPG/Ti heat spreading fins. These stresses are those over the surface of the ten-module radiator panel for the launch vibration load of the Falcon Heavy at vibration frequencies of 5, 25, and 50 Hz. The highest Von Mises stress in the Ti heat pipe wall of 22.5 MPa occurs for the 25 Hz launch load, along the heat pipes evaporator sections in the modules (Figs. 39a). At 5 Hz and 50 Hz, the calculated peak stresses are lower, 14.9 MPa and 6.9 MPa, respectively (Figs. 39b

and c). The highest stresses occur in the heat pipe evaporator section near where the upper hemispherical portion meets the flat, lower section of the heat pipe wall (Fig. 5b and c). Although the induced highest stresses for the ten-modules radiator panel are greater than those for a single heat pipe module, they are well below the yield strength of the Ti-6Al-4V titanium alloy of 898 MPa at room temperature.

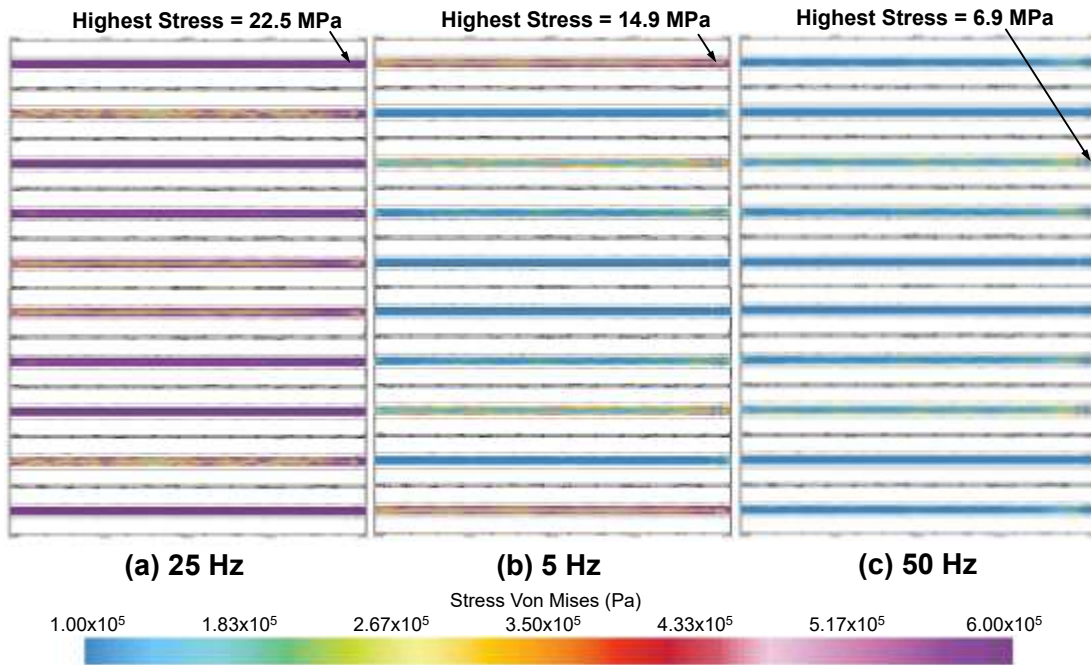


Figure 39: Images of the calculated Von Mises stresses along the inner surface of the Ti walls of the Cs-Ti heat pipes in the integrated panel with ten Ver. 7 heat pipe modules, for the Falcon Heavy launch loads and frequencies of 5, 25, and 50 Hz.

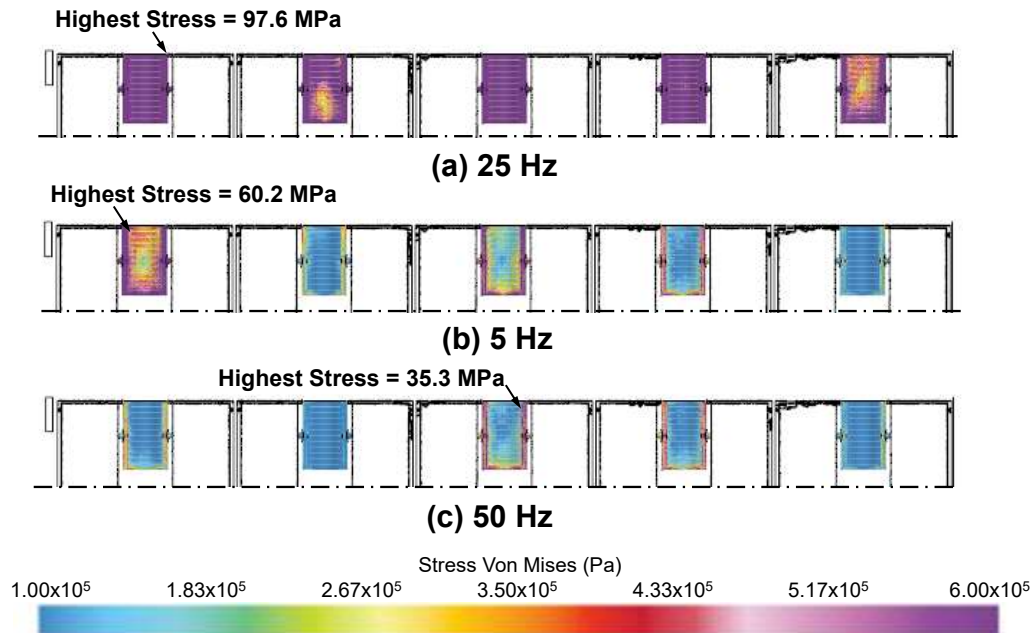


Figure 40: Images of calculated Von Mises stress in Ti walls of NaK-78 flow ducts of integrated radiator panel with ten Ver. 7 heat pipe modules for the Falcon Heavy at 5, 25, and 50 Hz.

Figure 40 shows an image of the calculated stresses in the Ti walls of the NaK-78 flow duct surrounding the heat pipe evaporator section for one half of the radiator panel in Fig. 37. The calculated stresses within the Ti duct wall (Fig. 40) are higher than within the heat pipe Ti wall (Figs. 39). The highest calculated stresses occur at the inlet and outlet flow headers of the NaK-78 flow ducts (Figs. 5, 8). The induced stresses in the walls of the curved upper ribbed portion and lower ribbed portion of the flow duct (Fig. 8) are much lower than in the headers of the duct. At load vibration frequencies of 25 Hz and 5 Hz, the highest stresses are 97.6 MPa and 60.2 MPa, respectively (Fig. 40a and b). The highest stress at a higher frequency of 50 is much lower, ~35.3 MPa (Fig. 40c). The highest calculated stress at 25 Hz is only 10.9% of the yield strength of the Ti-alloy duct wall. These results indicate that the calculated Von Mises stresses for the radiator panel with ten Ver. 7 heat pipe modules are safely below the failure criteria for the Ti walls of the Cs-Ti heat pipe and NaK-78 duct.

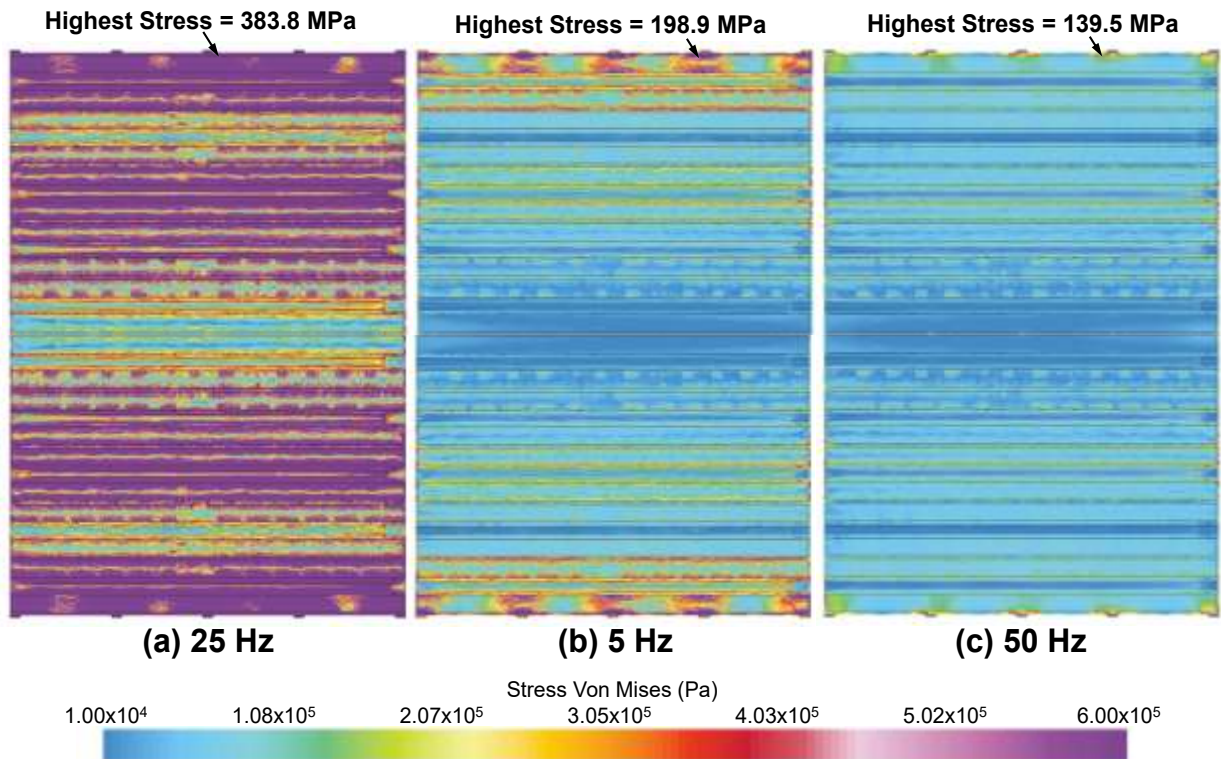


Figure 41: Calculated Von Mises stress for the Ti cladding of the HOPG/Ti fins in the integrated panel with ten Ver. 7 modules for Falcon Heavy at 5, 25, and 50 Hz.

Figure 41 shows a surface image of the calculated Von Mises stresses in the Ti cladding of the HOPG heat spreading fins and the outer support Ti frame of the radiator panel. In addition, Fig. 42 plots the calculated Von Mises stress along the lateral width of the radiator panel at the indicated locations in Fig. 37 of the end of the condenser section and the middle of the evaporator section of the Cs-Ti heat pipes. The induced stresses concentrate at points where the fins bend at either side of the hemispherical heat pipe in the modules and where the edge of the fins fit into the slots of the support frame (Figs. 41 and 42).

The calculated Von Mises stresses and the vertical displacements are highest at a vibration frequency of 25 Hz (Figs. 38 and 41a), followed by those for the 5 Hz and 50 Hz frequencies (Figs. 41b and c). The analysis results show that the highest calculated stresses within the HOPG's Ti cladding are 383.8 MPa for the 25 Hz vibration frequency (Fig. 41a). The highest

calculated peak stresses at frequencies of 5 Hz and 50 Hz are 198.9 MPa and 139.5 MPa, respectively (Figs. 41b-c). These stresses occur where the edges of the heat spreading fit into the slots of the support frame of the radiator panel.

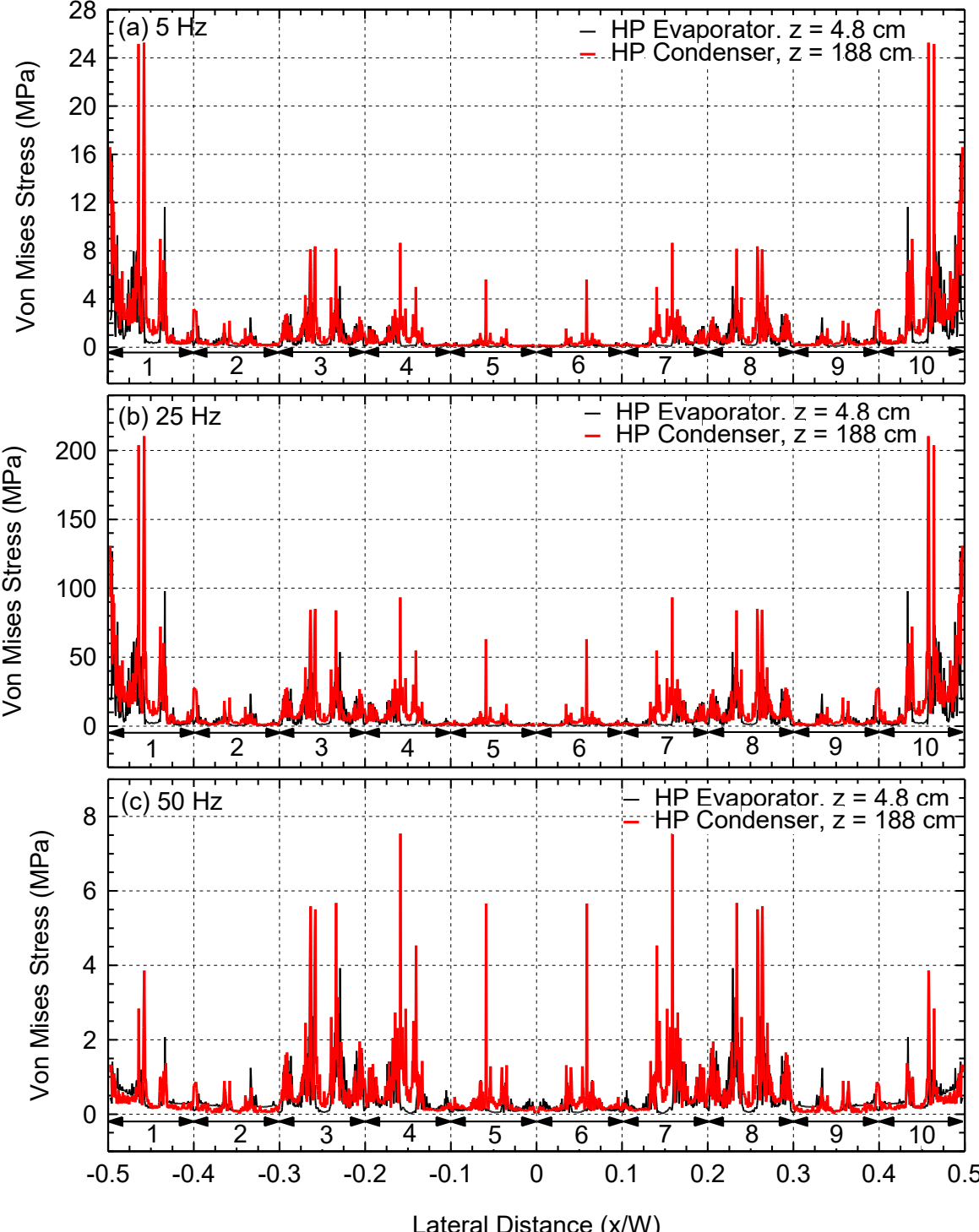


Figure 42: Plots of calculated Von Mises stresses along the Ti cladding of the HOPG/Ti fins for the radiator panel of ten Ver. 7 modules subject to lateral sinusoidal acceleration loads of the Falcon Heavy launch vehicle at 5, 25, and 50 Hz.

The calculated induced tensile stresses in the HOPG layer of the heat spreading reach a maximum of 56.1 MPa at 25 Hz. The calculated peak stresses are 11.7 MPa at 5 Hz, and 2.8 - 1.5 MPa at 50 - 100 Hz (Fig. 43). The calculated stress of 56.1 MPa is slightly higher than the tensile bending limit for the pyrolytic graphite of 53.7 MPa. However, this high stress occurs only along the extreme outer edges of the HOPG/Ti heat spreading fins within the support frame of the radiator panel. Also, the induced stresses throughout the width of the heat spreading fins moving outward from the central heat pipe are well below this limit. Therefore, the performance of the HOPG layers encased in Ti is unlikely to be affected. Additionally, the results indicate that the Ti cladding of the HOPG will remain intact because the calculated Von Mises stresses are below the yield strength criteria (Fig. 41).

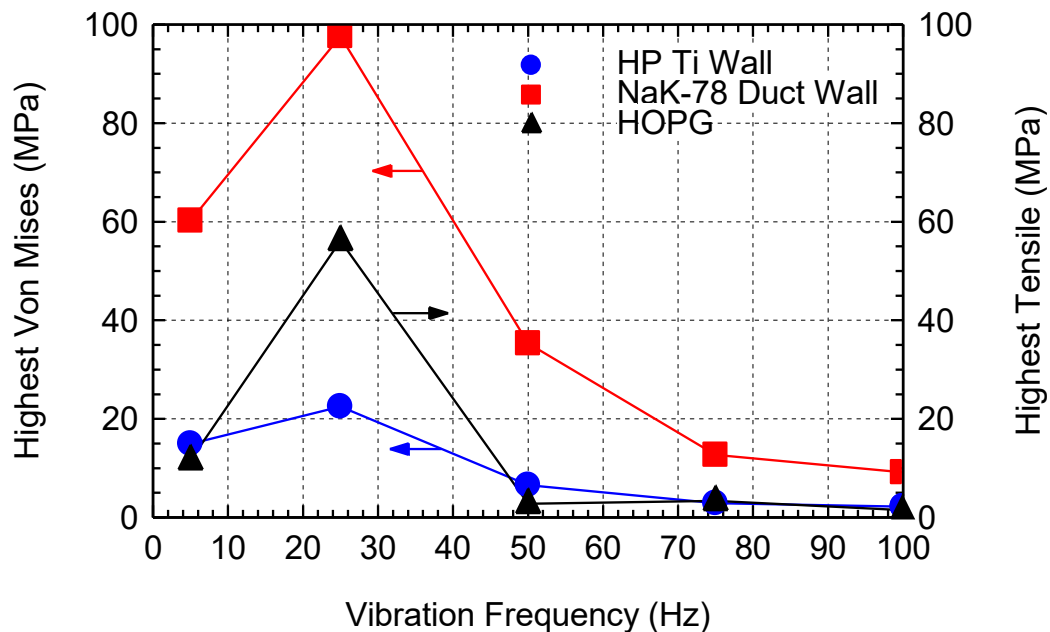


Figure 43: Comparison of the highest calculated Von Mises stress in the Ti heat pipe walls and the tensile stress in the HOPG heat spreading fins for ten Ver. 7 modules integrated radiator panel subject to the lateral launch loads of the Falcon Heavy launch vehicle at 5 -100 Hz.

6.5. Summary

The performed FEA calculated the induced stresses for a single Ver. 7 lightweight Cs-Ti heat pipe radiator module and an integrated radiator panel of ten modules with a Ti support frame. The calculated stresses are those experienced due to lateral vibration acceleration loads within the payload bay of the launch vehicle. The STAR-CCM+ multiphysics code is used to perform the FEA using the code's finite element solid stress analysis model. The heat pipe modules would be stowed within the launch vehicle in a vertical orientation with the evaporator section pointing upward and the condenser downward. The single module and panel of ten modules are subjected to the low-frequency 5 - 100 Hz lateral acceleration loads for two representative heavy lift launch vehicles, the Falcon Heavy and Delta IV Heavy.

The FEA analysis for the single Ver. 7 heat pipe module in a metal support frame simulated the launch vibration loads for the Falcon Heavy and Delta IV Heavy at 5, 50, and 100 Hz. The induced stresses within the heat pipe module due to the lateral acceleration loads increases with increased vibration frequency. The higher lateral acceleration loads for the Delta IV Heavy

result in higher stresses being higher than those for the Falcon Heavy, at same vibration frequencies.

For the Falcon Heavy left vehicle, the calculated Von Mises stresses within the Ti wall of Cs-Ti heat pipes peak at 4.7, 7.5, and 11.1 MPa at frequencies of 5, 50, and 100 Hz, respectively. The peak Von Mises stresses calculated for the Delta IV Heavy profile at these frequencies are 55%, 39%, and 16% higher, respectively. These differences are due to the higher payload acceleration loads for the Delta IV Heavy launch vehicle. The highest calculated Von Mises stresses in the Ti walls of the Cs-Ti heat pipe and NaK-78 flow duct wrapped around the evaporator are only 1.2 and 1.4% of the yield strength of the Grade 5 titanium alloy (Ti-6Al-4V). The highest calculated tensile stresses for the HOPG layer of the heat spreading fins are only 3% and 6% of the 1/3 tensile bending strength failure criteria for pyrolytic graphite. These results suggest that the induced vibration launch stresses for a single Ver. 7 heat pipe radiator module should not compromise the structural integrity during launch.

The results of the analyses of the ten-module radiator panel subjected to the Falcon Heavy launch loads show that the displacement is highest at 25 Hz when the panel is vibrating in the 1st mode. The maximum vertical displacement for the ten-modules radiator panel of 3.0 mm, is much higher than the 0.075 mm for the single heat pipe module. The large displacements induce higher stresses within the structural materials of the Ver. 7 heat pipe modules. The highest Von Mises stresses within the Ti-alloy walls of any of the ten the Cs-Ti heat pipes and NaK-78 ducts within the radiator panel are 22.5 and 97.6 MPa, respectively.

The flexing of the HOPG/Ti heat spreading fins by the oscillating launch acceleration load induces tensile stresses in the HOPG layer up to 56.1 MPa and Von Mises stresses in the Ti casing up to 383.8 MPa. The induced maximum Von Mises stresses in the ten Ver. 7 heat pipe modules of the radiator panel are all well below the room temperature yield strength of the Grade 5 Ti alloy for the wall material. The highest calculated stresses for the HOPG layer in the heat spreading fins reach the bending failure limit for pyrolytic graphite, but only at the extreme edges of the fins. These high stresses are unlikely to impact the heat spreading performance of the fins. In addition, the induced Von Mises stresses in the Ti-alloy material encasing of the HOPG heat spreading layers in the fins are significantly below the failure limit, thus maintaining the integrity of the fins.

7. Performance Parameters and Estimates of the Heat Pipe Radiator Panel

Table 10 lists the calculated estimates of the performance parameters for the developed C-C composite armored radiator panels of ten Ver. 4, 5, 6, 7, or 8, Cs-Ti heat pipe radiator modules (Figs. 6 and 7). These parameters are the total rejected power (kW), the total mass (kg), the specific power (kW/kg), the power density (kW/m²), the areal density (kg/m²). The radiator modules are mounted within a titanium support frame, with the NaK-78 flow ducts for the heat pipes' evaporator sections. The Cs-Ti heat pipes are hydraulically connected in parallel for operating at the same evaporator temperature and thermal power throughput and rejection into space at a surface average temperature of 600 K (Fig. 9). The estimates in Table 10 are based on the determined dimensions in Section 5 of the developed designs of the lightweight Cs-Ti heat pipe radiator modules.

The exposed surfaces of the Cs-Ti heat pipes and HOPG/Ti fins are adequately armored with C-C composite for protection against impact by micrometeoroids and space debris for ≤ 10 years of surface life on the lunar surface. The estimates of the thicknesses of the C-C composite armor in Section 6 are for vertically erected radiator modules and panels. The determined thicknesses are functions of the perforation probability of the Cs-Ti heat pipe and the penetration probability of the HOPG/Ti heat spreading fins. The values for the heat pipe modules listed in Table 10 are for 10% penetration and perforation probabilities more than 10 years of service life on the Moon.

The total mass estimates in Table 10 include those of the radiator modules for the Cs-Ti heat pipe, the Cs heat pipe working fluid, the C-C composite armor, the Ti support frame, and the dry flow ducts of the heat pipe evaporator section, but not the masses of the portion of the liquid NaK-78 loop prior to the Cs-Ti heat pipe flow ducts (Fig. 9). The radiatively rejected total thermal power from the ten-radiator modules panel at an average temperature of $T_s = 600$ K into space on the lunar surface decreases as the Cs vapor flow area in the Cs-Ti heat pipes in the modules decreases.

The heaviest panel of ten Ver. 4 modules, rejects 67.5 kW and the lightest panel of ten Ver. 7 modules rejects 56.3 kW. The radiator panel with ten Ver. 8 modules of the Cs-Ti heat pipes with the longest evaporator section, $L_{ev} = 15$ cm, has the highest rejected thermal power of 96.3 kW compared to 60.8 kW for the panel with ten Ver. 6 Cs-Ti heat pipe radiator modules of the same Cs vapor flow area in the heat pipes, but with 33% shorter evaporator sections, $L_{ev} = 10$ cm (Table 10).

The mass of the Cs-Ti heat pipe in the radiator modules decreases by decreasing the vapor flow area of the Cs vapor flow from 27.7 cm² for Ver. 4 Cs-Ti heat pipe module to 13.8 cm in Ver. 6 and 8 heat pipe modules, a 50% reduction. The Cs vapor flow area for the Cs-Ti heat pipe in Ver. 7 radiator module of only 8.3 cm² is the lowest, only 30% of that in the Ver. 4 radiator module (Table 10). As shown in this table, the mass of the Ver. 4 heat pipes panel is 36.4% of that of panel, and the masses of the HOPG/Ti heat spreading fins, the C-C armor, and the aluminum frame support structure are 38.4%, 20.9%, and 4.1% of the total panel mass, respectively.

The larger projected area of the Ver. 4 Cs-Ti heat pipe compared to those for Ver. 5, 6, and 7 radiator modules require thicker C-C composite armor for the same 10% perforation probability over the 10-year operation life on the lunar surface [24, 27]. The estimated thickness of the C-C composite armor of the heat pipe for the Ver. 4 radiator module is 0.78 mm. For the same perforation probability, thickness of the C-C composite armor for Cs-Ti heat pipe in the Ver. 5, 6, and 7 radiator modules decreases to 0.72, 0.65, and 0.58 mm, respectively. The thickness of the C-C composite armor of the longest Cs-Ti heat pipe in Ver. 8 radiator module at same perforation probability of 10% (~ 0.78 mm), is larger than that in Ver. 6 heat pipe module with the same Cs vapor flow area. The applied C-C composite armors for the

Cs-Ti heat pipe and the HOPG/Ti heat spreading fins increase the total mass of the heat pipe modules.

The planar area for the integrated radiator panel of ten Ver. 7 radiator modules is 17.4% lower than that of the panel with the same number of Ver. 4 radiator modules. The 29.4 % lower total masses of Ver. 7 radiator module and of the radiator panel of 10 modules effectively decrease the corresponding areal density estimates in kg/m² (Table 10). The radiator panel with ten Ver. 6 heat pipe modules has an areal density of 3.08 kg/m² and that of the radiator panel with ten Ver. 7 heat pipe modules is lowest at 2.98 kg/m² (Table 10). The value satisfies NASA's desired target for the present work.

Table 10. Estimates comparison of the total rejected power (kW), total mass (kg), specific power (kW/kg), areal density (kg/m²) and power density (kW/m²) of C-C composite armored radiator panels, each of ten Ver. 4, 5, 6, 7, and 8 designs of Cs-Ti heat pipe radiator modules (Figs. 6, 7, and 15).

Cs-Ti Module Version/HP OD (cm)	Ver. 4/8.73	Ver. 5/7.34	Ver. 6/5.94	Ver. 7/4.60	Ver. 8/5.94
Armor HP Perforation & HOPG/Ti Fins Penetration Probabilities	10%	10%	10%	10%	10%
Cs HP Vapor Flow Area (cm²)	27.7	19.4	13.8	8.3	13.8
Cs HP Condenser/Total Length (cm)	188/198	186/196	183/193	179/189	277/292
Cs HP Margin to Entrainment Limit (%)	79	71	61	40	69
Armored Panel Frame Mass (kg)	0.84	0.79	0.75	0.65	1.14
Panel Cs-Ti HPs (kg)	7.31	6.61	5.80	5.15	9.52
Panel HOPG/Ti Fins (kg)	7.69	7.28	6.92	6.59	10.99
Panel C-C Composite Armor (kg)	4.20	3.26	2.43	1.76	6.36
Armored Panel Heat Rejection area (m ²)	5.76	5.42	5.14	4.75	7.77
Armored Panel Rejected Power (kW)	67.5	64.0	60.8	56.3	96.3
Armored Panel Total Mass (kg)	20.05	17.94	15.91	14.15	28.0
Armored Panel Specific Power (kW/kg)	3.36	3.56	3.82	3.98	3.44
Armored Panel Areal Density (kg/m²)	3.47	3.30	3.08	2.98	3.60
Armored Panel Power Density (kW/m²)	7.56	7.56	7.56	7.56	7.56

The integrated radiator panel with ten Ver. 8 radiator modules with the longest heat pipe evaporator, $L_{ev} = 15$ cm and heat pipe condenser, $L_{cd} = 277$ cm has much larger projected area than the panel with ten Ver. 6 and Ver. 7 Cs-Ti heat pipe modules with $L_{ev} = 10$ cm and shorter $L_{cd} = 183$ cm and 197 cm, respectively (Table 10). Larger projected area of the Cs-Ti heat pipe in the radiator modules increases the C-C composite armor thickness and mass and the total mass of the Ver. 8 heat pipe radiator modules, compared to those of Ver. 6 and 7 modules, for the same 10% perforation probability for more than 10-year service life on the lunar surface. Consequently, the C-C armor mass increases the areal density of the panel with ten Ver. 8 modules to 3.60 kg/m², compared to 3.08 and 2.08 kg/m² for the radiator panel with ten Ver. 6 and Ver. 7 heat pipe modules, respectively (Table 10). Thus, increasing the evaporator length of the heat pipe in Ver. 8 module, although significantly increases the total rejected power into space, it is not an attractive option for decreasing the radiator panel's areal density.

The total masses of the Cs-Ti heat pipes and the C-C composite armor decrease with decreasing the Cs-Ti heat pipe diameter or the Cs vapor flow area in the developed designs of the radiator modules. The mass of the integrated radiator panel of ten Ver. 7 radiator modules is 29.4% lower than that of the panel of ten Ver. 4 radiator modules, while the rejected total power decreases by only 16.5%. As a result, the specific power of the radiator panel with ten Ver. 4 radiator modules is 3.36 kW/kg compared to 3.98 kW/kg for the panel with ten Ver. 7 modules. The radiator panel with ten Ver. 8 radiator modules has an estimated specific power of 3.44 kW/kg, which is lower than the 3.82 kW/kg for the panel with ten Ver. 6 modules of the same Cs-Ti heat pipe diameter. The higher mass of the C-C composite armor for the Ver. 8 module compared to that of the Ver. 6 module decreases the specific power of the integrated radiator panel of ten modules.

8. Summary and Conclusions

The focus of present Phase 1 ESI NASA grant award to UNM-ISNPS is to develop a lightweight design of a heat rejection radiator for operating at a surface average temperature of 600 K for heat rejection into space on the lunar surface. Our team successfully developed innovative lightweight radiator modules and panel of Cs-Ti heat pipes with HOPG/Ti heat spreading fins for meeting the stated objectives. In addition to selecting the heat pipe working fluid and structural materials, this effort conducted 2D heat pipe analyses, 3D CFD thermal analyses, armoring analyses using C-C composite, and structural analyses during launch on board two representative heavy launch vehicles. The final estimate of the areal density of the radiator panel of ten Ver. 7 Cs-Ti heat pipe modules with HOPG/Ti heat spreading fins meet the desired objectives of modularity, redundancy, reliability for the avoidance of single point failures and an areal density $< 3.0 \text{ kg/m}^2$.

In addition to the 2-D modeling of the Cs-Ti heat pipe and the 3-D CFD thermal performance of the Cs-Ti heat pipe modules, the armor analyses to protect the exposed surfaces against the impact by meteorites and space debris determined the thicknesses of the C-C composite armor as functions of the perforation probability of the Cs-Ti heat pipes and the penetration probability of the heat spreading fins. The obtained results of the performed modeling of the induced stresses due to the vibration load and frequencies of the heat pipe modules and the integrated radiator panel are for launch conditions of two heavy lift vehicles.

The developed designs of the heat pipe radiator modules and panel are appropriately armored with C-C composite, to reduce the risk of the impacting micrometeorites. The finale selected designs are for $< 10\%$ probabilities of perforating the Cs-Ti heat pipes and penetrating the HOPG/Ti heat spreading fins during more than ten-year operation life on the lunar surface.

The performed FEA of the Cs-Ti heat pipe modules with HOPG/Ti heat spreading fins and a radiator panel of ten integrated modules with a Ti frame confirmed the integrity of the structural materials in the panel during launch to the lunar surface. Obtained results of the induced stresses are for the launch vibration loads on board of two heavy left vehicle for a wide range of frequencies from 5 – 100 Hz. In addition, experimental characterization of the Ti-C interfaces for HOPG test samples coated with thin Ti layer is conducted. Results show a clean interface without the formation of carbides, which could be suitable for diffusion bonding.

In conclusion, the breadth and the results of this three-year effort by UNM-ISNPS support the promise of developing a lightweight radiator concept with no single point failures for surface fission power system on the lunar surface. The lightweight radiator panel with ten Ver. 7 heat pipe modules with an estimated areal density of 2.98 kg/m^2 and a specific power of 3.98 kW/kg meets NASA's desired object for this project. These values are considerable improvements over those reported for SOA heat pipes radiators of $5.24 - 12.7 \text{ kg/m}^2$ and $0.1-2.68 \text{ kW/kg}$, respectively (Figs. 1 and 2).

9. Dissemination of Results

The results of the performed research have been widely disseminated and distributed among the space and nuclear power communities. In addition to the virtual technical seminars at the NASA Glenn Research Center and the NASA Marshall Space Flight Center, the results of the completed work have been presented at the AIAA ASCEND'23 and ASCEND'24 conferences and the ANS NETS 2024 conference to large audiences.

The results have also been published in referred journal articles and conference proceedings papers. In addition, the issued annual reports for the project's continuation reviews have been made publically available on the UNM-ISNPS's website <https://isnps.unm.edu/>. The list of current publications is as follows:

Journal Articles

EI-Genk, M. S., T. M. Schriener, "Lightweight Heat Pipe Radiator for Nuclear Reactor Power Systems on Lunar Surface". Nuclear Technology, 1-29, 2024.
<https://doi.org/10.1080/00295450.2024.2329830>.

Schriener, T. M., M. S. EI-Genk, "Armor Analyses of Lightweight, Heat Rejection Radiator Modules on the Lunar Surface," Nuclear Technology (submitted, 2024).

Schriener, T. M., M. S. EI-Genk, "Finite Element Stress Analyses of a Lightweight Cs-Ti Heat Pipe Radiator for Fission Surface Power Systems under Low Frequency Vibration Launch Loads," (in preparation).

Conference Papers

EI-Genk, M. S., T. Schriener, "Design and Analyses of Lightweight Radiator Module for Nuclear Reactor Lunar Surface Power". Proceedings AIAA ASCEND 2023 Conference, Las Vegas, Nevada, 23 October – 25 October 2023. <https://doi.org/10.2514/6.2023-4690/>.

EI-Genk, M. S., T. Schriener, "Lightweight Heat Pipe Radiator Panel for Lunar Surface Fission Power Systems". Proceedings AIAA ASCEND 2024 Conference, Las Vegas, Nevada, 29 July – 2 August 2024. <https://doi.org/10.2514/6.2024-4937/>.

Schriener, T. M., M. S. EI-Genk, "Armored Lightweight Heat Rejection Radiator for Lunar Surface Nuclear Reactor Power Systems". Proceedings ANS 2024 Nuclear and Emerging technologies for Space (NETS 2024), Santa Fe, New Mexico, 6 May – 10 May 2024. <https://www.ans.org/pubs/proceedings/article-55754/>.

Technical Reports

EI-Genk, M. S., T. Schriener, O. Anderoglu, C. Wolf, "Advanced Lightweight Heat Rejection Radiators for Space Nuclear Power Systems Year 1 ESI Continuation Review Grant Performance Summary." Technical Report 21 ESI-0049-1, Institute for Space and Nuclear Power Studies (ISNPS), University of New Mexico, Albuquerque, New Mexico, 2022. https://isnps.unm.edu/reports/ISNPS_Tech_Report_97.pdf

EI-Genk, M. S., T. Schriener, O. Anderoglu, "Advanced Lightweight Heat Rejection Radiators for Space Nuclear Power Systems Year 2 ESI Continuation Review Grant Performance

Summary.” Technical Report 21 ESI-0049-2, Institute for Space and Nuclear Power Studies (ISNPS), University of New Mexico, Albuquerque, New Mexico, 2023.
https://isnps.unm.edu/reports/ISNPS_Tech_Report_99.pdf

10. NASA Collaboration

Regular contact has been maintained with NASA Research Collaborator Dr. Fernando Reyes Tirado at Marshall Space Flight Center. Frequent meetings have been held with Dr. Tirado to keep him apprised for research progress and for discussion of results and feedback. Dr. Tirado hosted a virtual technical seminar at MSFC on November 2024 and Lee Mason hosted a virtual seminar at NASA Glenn Research Center on 13 January 2023. See next section for details.

11. Annual Technical Seminars

Completed Annual Technical Seminars				
<i>Award Year</i>	<i>Date</i>	<i>NASA Center</i>	<i>Seminar POC</i>	<i>Seminar Topic and <u>Optional</u> Comments</i>
1	1/11/23	GRC	Lee Mason	The seminar presented a historical review of heat rejection radiator systems for space nuclear power systems and presented the results of the performance analysis and experimental characterization work performed to date for the project. The seminar was presented to a virtual audience at GRC. A total of twenty-five people attended the seminar from GRC, MSFC, JSC. This is in addition to individuals from space and fission power industries.
3	11/25/24	MSFC	Fernando Reyes Tirado	The seminar presented the results of the ESI project to a virtual audience at Marshall Space Flight Center, summarizing the accomplishments for the completed modeling and simulation and experimental tasks.

12. New Technology, Reportable Items, Inventions, and Patents

A patent disclosure had been filed with the University of New Mexico's Rainforest Innovation prior to the submission of the proposed work for funding consideration by NASA.

13. Students

Assistance Type	Number	Roles / Comments
Graduate	2	Graduate students funded in part or entirely by the ESI grant helped with the C-C and Graphite samples' preparation for Ti deposition, the characterization of the coated samples, and the modeling and simulation tasks.
Undergraduate	3	Undergraduate students funded by the ESI grant assist with the upgrade of the vacuum test facility and out gassing of the test samples.

14. Technology Outlook

The present Phase-1 NASA ESI project involved comprehensive design, modeling and performance analyses of Cs-Ti heat pipe radiator modules and an integrated ten modules panel. This is in addition to 3-D CFD and thermal modeling, micrometeoroid armor analysis, and 3-D thermal performance and structural analyses of launch vibration stresses using FEA methods. The experimental tasks characterized the interfaces of Ti-coated HOPG and C-C composite samples to investigate the potential for diffusion bonding in vacuum space. At the conclusion of this effort, the TRL of the lightweight heat pipe radiator design concept has increased from ~1-2 to ~ 3 defined as *analytical studies place the technology in an appropriate context, modeling and simulation validate analytical prediction*.

The next phase of development could involve fabricating and testing prototype Cs-Ti heat pipe modules for experimental testing and demonstration. The testing would also provide validation data for future modeling and simulation efforts. Further material testing could demonstrate large area diffusion bonding of the C-C composite armor to the Cs-Ti heat pipe modules and HOPG/Ti heat spreading fins.

The developed innovative heat pipe radiator design concept for average surface temperature of 600 K for heat rejection is attractive for future nuclear fission power systems for future space exploration and planetary surface power applications at different heat rejection temperatures, but for different heat pipe working fluids and material commensurate with the design of the fission reactor power system. The developed lightweight heat pipe radiator concept in the present project has an estimated areal density $\leq 3.0 \text{ kg/m}^2$. This is a significant reduction from the SOA values of 5.24-12.7 kg/m^2 for heat pipe radiator panels for space fission power systems and fulfils NASA's state objectives for the present work.

The present project designed and analyzed the performance of a modular, foldable, rectangular radiator panel for fission surface power systems to support the future human exploration and development of the Moon and Mars. A modified design of the developed Cs-Ti heat pipe modules in this work can be assembled and hydraulically operated in parallel in the truncated cone heat rejection radiators of nuclear reactor power systems for nuclear electric propulsion to explore the solar system.

Potential users of this technology include NASA, the US Space Force, and space industry for future development and deployment of fission power systems for space and planetary surface power missions. The growing commercial interest in nuclear power to support the development of space resources on the Moon under the Artemis Accords would be a major driver. This means that interest in the lightweight heat pipe radiator technology could extend beyond the US government to include commercial space companies with plans for lunar development activities.

Acknowledgements

We acknowledge Professor Osman Andergolu for leading the experimental effort in 2022 and 2023 characterizing the C-Ti interfaces using TEM and EDX methods on the prepared and coated HOPG and C-C composite samples. We also acknowledge Jared Justice, graduate student of Professor Osman Andergolu, for helping with the FIB and SEM characterizations of the Ti coated specimens. We also acknowledge the contributions of Chris Wolfe, graduate student of Professor Mohamed El-Genk, and undergraduate student Christopher Arguello for assisting with the sample preparation and upgrading the vacuum test facility at UNM-ISNPS.

We thank Lee Mason for generously hosting the virtual seminar held at NASA Glenn Research Center, and Fernando Reyes Tirado for hosting the virtual seminar at NASA Marshall Space Flight Center.

We wish to acknowledge the valuable assistance provided by J. Kevin Baldwin at the Center for Integrated Nanotechnologies (CINT) at Los Alamos National Laboratory in performing the magnetron sputtering coating of the prepared C-C composite and HOPG samples and for helping the upgrade of the vacuum facilities at UNM-ISNPS. The magnetron sputtering of Ti onto the surfaces of the prepared C-C and graphite samples is performed as part of a 2022 CINT rapid access proposal to UNM-ISNPS (CINT proposal number 2022ARA0038) to support the research on the NASA ESI grant.

This work is performed, in part, at the Center for Integrated Nanotechnologies, an Office of Science User Facility operated for the U.S. Department of Energy (DOE) Office of Science by Los Alamos National Laboratory (Contract 89233218CNA000001) and Sandia National Laboratories (Contract DE-NA-0003525).

We are also grateful for the access to the resources of the High-Performance Computing Center at Idaho National Laboratory, which is supported by the Office of Nuclear Energy of the U.S. Department of Energy and the Nuclear Science User Facilities under Contract No. DE-AC07-05ID14517 and the UNM Center for Advanced Research Computing, supported in part by the National Science Foundation, for providing access to its high-performance computing capabilities.

Nomenclature

A_{an}	Flow area of the heat pipe liquid annulus (m^2)
A_{vap}	Heat pipe vapor flow area (m^2)
AFSPS	Affordable Fission Surface Power System
AMTEC	Alkali Metal Thermal to Electric Conversion
C	Speed of sound in armor material (m/s)
C-C	Carbon-Carbon composite
CBC	Closed Brayton Cycle energy conversion.
CFD	Computational Fluid Dynamics
CMOR	Canadian Meteor Orbit Radar
Cs	Cesium
D_{HP}	Heat pipe curvature diameter (m)
D_h	Equivalent hydraulic diameter (m)
d_p	Micrometeor particle diameter (mm)
ESA	European Space Agency
ESI	Early Stages Innovation
F_{ip}	Cumulative interplanetary micrometeor flux (number/ m^2 -s)
F_r	Cumulative incident flux of micrometeors (number/ m^2 -s)
FEA	Finite Element solid stress Analysis
FOM	Figure of Merit
FPSE	Free Piston Stirling Engine
FSPS	Fission Surface Power System
G_p	Gravitational focusing factor.
h_{fg}	Latent heat of vaporization (kJ/kg)
HB	Brinell hardness
HOPG	Highly Oriented Pyrolytic Graphite
HP	Heat Pipe
HPTrAM™	Heat Pipe Transient Analysis Model for the radiator Cs heat pipe
IMEM	Interplanetary Micrometeoroid Environmental Model
ISNPS	Institute for Space and Nuclear Power Studies
JIMO	Jupiter Icy Moons Orbiter
k	Shielding factor for orientation relative to direction compared to orbital plane
K	Potassium
L	Length (m)
L_{cd}	Heat pipe condenser length (m)
L_{ev}	Heat pipe evaporator length (m)
L_{hp}	Heat pipe total length (m)
LANL	Los Alamos National Laboratory
Li	Lithium
m_p	Micrometeor particle mass (g)
\dot{m}	Liquid NaK-78 flow rate (kg/s)
MEM	Meteoroid Engineering Model
MMOD	Micrometer and Orbital Debris

MW	Molecular weight of working fluid (kg/mol)
Na	Sodium
NaK-78	Sodium-Potassium alloy with 78wt% Potassium
NASA	National Aeronautics and Space Administration
P	Probability
Pr_t	Turbulent Prandtl number
PMD	Power Management and Distribution
R_g	Gas constant (J/mol-K)
R_p	Geometric radius of pores in sintered wick in heat pipe (m)
RANS	Reynolds Averaged Navier Stokes
Rb	Rubidium
Q	Heat pipe power throughput (W)
Q_{ent}	Heat pipe entrainment limit (W)
Solid angle factor incoming isotropic micrometeor particles	
SAIRS	Scalable AMTEC Integrated Reactor space power System
SEA	Statistical Energy Analysis
SOA	State-of-the-Art
SCoRe-TE	Sectored Compact Reactor with TE conversion for lunar surface power.
SST	Shear Stress Transport
t	Time (s)
T	Temperature (K)
TE	Thermoelectric energy conversion
TE-EM	Thermoelectric Electromagnetic
T_{ex}	Circulating liquid NaK-78 exit temperature (K)
T_{ev}	Heat pipe evaporator temperature (K)
T_{in}	Circulating liquid NaK-78 inlet temperature (K)
T_s	Radiator surface average temperature for heat rejection (K)
T_{sink}	Radiative environment sink temperature (K)
TE	Thermoelectric conversion
TI	Thermionic conversion
Ti	Titanium
UNM	University of New Mexico
UTS	Ultimate tensile strength (Pa)
V	Velocity (m/s)
W_{fin}	Width of the HOPG/Ti/C-C heat spreading fins (cm)
x	lateral coordinate (m)
z	axial coordinate (m)

Greeks

δ_{HOPG}	Thickness of the HOPG layer in the heat spreading fins (m)
δ_{an}	Width of liquid annulus in the Cs-Ti heat pipe (m)
δ_{al}	Equivalent aluminum thickness of the HOPI/Ti fins (mm)
δ_{C-C}	C-C armor thickness of the Cs-Ti heat pipes in radiator modules (mm)
$\delta_{C-C,f}$	C-C armor thickness for the HOPG /Ti heat spreading fins (mm)

δ_{∞}	Semi-infinite depth of penetration (mm)
ΔP_{cap}	Heat pipe capillary pressure head (Pa)
ΔP_l	Liquid pressure losses (Pa)
ΔP_v	Vapor pressure losses (Pa)
ε	Radiator surface emissivity (-)
μ_l	Liquid viscosity (Pa.s)
ρ	Density (kg/m^3)
ρ_v	vapor density (kg/m^3)
σ_l	Liquid surface tension (N/m)

References

1. M. RUCKER, "Integrated surface power strategy for Mars," *Proceedings Nuclear and Emerging Technologies for Space 2015 (NETS)*, Albuquerque, NM, February 23-26, 1-10 (2015).
2. L. KALDON, Overview of NASA Fission Surface Power, Proceedings of Nuclear and Emerging Technologies for Space 2023 (NETS), Idaho Falls, ID, May 7-11 (2023).
3. J. ANGELO JR, D. BUDEN, *Space nuclear power*. Malabar, FL: Orbit Book Co., p. 159–176 (1985)
4. A. MARRIOTT, T. FUJITA, "Evolution of SP-100 System Designs," *Proceedings of 11th Symposium on Space Nuclear Power and Propulsion* (El-Genk and Hoover, Editors), AIP Conference Proceedings No. 301, American Institute of Physics, New York, NY (1994).
5. T.M. SCHRIENER, M.S. EL-GENK, "Thermal-Hydraulics and Safety Analyses of the Solid Core-Sector Compact Reactor (SC-SCoRe) and Power System," *Progress in Nuclear Energy*, **76**, 216-231 (2014).
6. M.S. EL-GENK, J.-M. TOURNIER, "Performance Analysis of Potassium Heat Pipes Radiator for HP-STMCs Space Reactor Power System." *Proceedings of Space Technology and Applications International Forum, STAIF-2004* (M.S. El-Genk, Editor), AIP No. 699, 793-805 (2004).
7. M.S. EL-GENK, J.-M. TOURNIER, "SAIRS' - Scalable AMTEC Integrated Reactor Space Power System." *J. Progress in Nuclear Energy*, **45**, 25-69 (2004).
8. L. MASON, D. POSTON, L. QUALLS, *System Concepts for Affordable Fission Surface Power*. NASA Glenn Research Center, Cleveland, OH, NASA/TM-2008-215166 (2008).
9. K.L. LEE, C. TARAU, W.G. ANDERSON D. BEARD, "Titanium-water heat pipe radiators for space fission power system thermal management," *Microgravity Science and Technology*, **32**, 453-464 (2020).
10. D.I. POSTON, "The heat pipe-operated Mars exploration reactor (HOMER)," *Proceedings of Space Technology and Applications International Forum, (STAIF-2001)* (M.S. El-Genk, Editor), AIP No. 552, 1, 797-804 (2001).
11. R. HARTY, L. MASON, "100 kWe Lunar/Mars surface power utilizing the SP-100 reactor with dynamic conversion," In: El-Genk MS, editor. *Proceedings Symposium on Space Nuclear Power and Propulsion* (M.S. El-Genk, Editor). AIP CP-271, 2, 1065–1071 (1993).
12. M.J. WOLLMAN, M.J. ZIKA, *Prometheus Project Reactor Module Final Report*. Knolls Atomic Power Laboratory and Bettis Atomic Power Laboratory. SPP-67110–0008 (2006).
13. J. SIAMIDIS, L.S. MASON, *A Comparison of Coolant Options for Brayton Power Conversion Heat Rejection Systems*, NASA/TM—2006-214121, GRC, Cleveland, OH (2006).
14. J. ELLIOTT et al., *Prometheus – Project Lunar Fission Surface Power System Study Report*. NASA Jet Propulsion Laboratory, Pasadena, CA, JPL-982-R66153 (2005).
15. M.S. EL-GENK, J.-M. TOURNIER, B.M. GALLO, "Dynamic Simulation of a Space Reactor System with Closed Brayton Cycle Loops," *J. Propulsion and Power*, **26**, 3, 394-406 (2010).
16. M.S. EL-GENK, J.-M. TOURNIER, "High Temperature Water Heat Pipes Radiator for a Brayton Space Reactor Power System." *Proceedings of Space Technology and Applications International Forum, STAIF-2006* (M.S. El-Genk, Editor), AIP Conference Proceedings No. 813, 716-729 (2006).

17. D.I. POSTON, R.J. KAPERINICK, R.M. GUFFEE, "Design and analyses of the SAFE-400 space fission reactor," *Proceedings of Space Technology and Applications International Forum, (STAIF-2002)* (M.S. El-Genk, Editor), AIP No. 608, 578–588 (2002).
18. M.S. EL-GENK, J.-M. TOURNIER, "Performance Comparison of Potassium and Sodium Vapor Anode, Multi-Tube AMTEC Converters," *J. Energy Conversion & Management.*, **43**, 1931-1951 (2002).
19. NASA SPACE TECHNOLOGY MISSION DIRECTORATE, *Space Technology Research Grants Program, Early-Stage Innovations Appendix*, 80HQTR21NOA01-21ESI-B2, Washington, DC (2021).
20. M.S. EL-GENK, T.M. SCHRIENER, O. ANDEROGLU, C. WOLF, *Advanced Lightweight Heat Rejection Radiators for Space Nuclear Power Systems Year 1 ESI Continuation Review Grant Performance Summary*, Technical Report 21 ESI-0049-1, Institute for Space and Nuclear Power Studies (ISNPS), University of New Mexico (2022).
21. S.A. HATTON, M.S. EL-GENK, "Sectored Compact Space Reactor (SCoRe) Concepts with a Supplementary Lunar Regolith Reflector," *Progress in Nuclear Energy*, **51**, 93-108 (2009).
22. M.S. EL-GENK, "Deployment history and design considerations for space reactor power systems," *Acta Astronautica*, **64**, 9-10, 833-849 (2009).
23. M.S. EL-GENK, T.M. SCHRIENER, O. ANDEROGLU, *Advanced Lightweight Heat Rejection Radiators for Space Nuclear Power Systems Year 2 ESI Continuation Review Grant Performance Summary*, Technical Report 21 ESI-0049-1, Institute for Space and Nuclear Power Studies (ISNPS), University of New Mexico (2023).
24. M.S. EL-GENK, T. M. SCHRIENER, "Lightweight Heat Pipe Radiator for Nuclear Reactor Power Systems on Lunar Surface". *Nuclear Technology*, 1-29 (2024).
25. M.S. EL-GENK, T.M. SCHRIENER, "Design and Analyses of Lightweight Radiator Module for Nuclear Reactor Lunar Surface Power", *Proceedings AIAA ASCEND 2023*, Las Vegas, NV, October 23-25 (2023).
26. M.S. EL-GENK, T.M. SCHRIENER, "Lightweight Heat Pipe Radiator Panel for Lunar Surface Fission Power Systems". *Proceedings AIAA ASCEND 2024*, Las Vegas, NV, July 29 –August 2 (2024).
27. T.M. SCHRIENER, M.S. EL-GENK, "Armored Lightweight Heat Rejection Radiator for Lunar Surface Nuclear Reactor Power Systems". *Proceedings ANS 2024 Nuclear and Emerging technologies for Space (NETS 2024)*, Santa Fe, NM, May 6-10 (2024).
28. SIEMENS PLM, STAR-CCM+, <https://plm.sw.siemens.com/>, (2023)
29. J.-M. TOURNIER, M.S. EL-GENK, "Current Capabilities of 'HPTAM' for Modeling High-Temperature Heat Pipes Startup from a Frozen State". *Proc. Space Technology and Applications International Forum (STAIF-2002)*, AIP No.608, 139-147 (2002).
30. P.G. KLEMENS, D.F. PEDRAZA, "Thermal conductivity of graphite in the basal plane," *Carbon*, **32**, 4, 735-741 (1994).
31. M.S. EL-GENK, J.-M. TOURNIER, "Challenges and Fundamentals of Modeling Heat Pipes Startup from a Frozen State". *Proc. Space Technology and Applications International Forum (STAIF-2002)*, AIP No.608, 127-138 (2002).
32. J.-M. TOURNIER, M.S. EL-GENK, "Transient Analysis of the Startup of a Water Heat Pipe from a Frozen State," *Journal of Numerical Heat Transfer, Part A, Applications*, **28**, 461-486 (1995).

33. R.S. REID, et al., *Heat Pipe Development for Advanced Energy Transport Concepts, Phase II - Progress Report Covering the Period October 1, 1997, to September 30, 1998*, Los Alamos National Laboratory, Los Alamos, NM, Progress Report No. LA-13549-PR, (1999).
34. A.J. REYNOLDS, "The prediction of turbulent Prandtl and Schmidt numbers," *International Journal of Heat and Mass Transfer*, **18**, 1055–1069 (1975).
35. G.P. PETERSON, *An Introduction to Heat Pipes: Modeling, Testing, and Applications*, John Wiley & Sons, New York, NY (1994).
36. B. J. ANDERSON and R. E. SMITH, "Natural Orbital Environment Guidelines for Use in Aerospace Vehicle Development," NASA technical memorandum 4527, NASA Marshall Space Flight Center, Huntsville, AL, (1994).
37. V. DIKAREV, E. GRUEN, J. BAGGALEY, D. GALLIGAN, M. LANDGRAF, and R. JEHN, "The new ESA meteoroid model," *Advances in Space Research*, **35**, 7, 1282-1289 (2005), <https://doi.org/10.1016/j.asr.2005.05.014>.
38. R. H. SOJA, E. GRUEN, P. STRUB, M. SOMMER, M. MILLINGER, J. VAUBAILLON, W. ALIUS, G. CAMODECA, F. HEIN, J. LASKAR, and M. GASTINEAU, "IMEM2: a meteoroid environment model for the inner solar system," *Astronomy & Astrophysics*, **628**, A109 (2019), <https://doi.org/10.1051/0004-6361/201834892>.
39. A. V. MOORHEAD, H. M. KOEHLER, and W. J. COOKE, "NASA Meteoroid Engineering Model Release 2.0," Technical report NASA/TM-2015-218214, NASA Marshall Space Flight Center, Huntsville, AL, (2015).
40. E. GRUEN, R. SRAMA, M. HORANYI, H. KRÜGER, R. SOJA, V. STERKEN, Z. STERNOVSKY, and P. STRUB, "Comparative Analysis of the ESA And NASA Interplanetary Meteoroid Environment Models," *Proceedings 6th European Conference on Space Debris*, Darmstadt, Germany, paper 165, (2013).
41. E. GRUEN, H. A. ZOOK, H. FECHTIG, and R. H. GIESE, "Collisional Balance of the Meteoritic Complex," *Icarus*, **64**, 244-272 (1985), [https://doi.org/10.1016/0019-1035\(85\)90121-6](https://doi.org/10.1016/0019-1035(85)90121-6).
42. E. GRUEN, M. HORANYI, and Z. STERNOVSKY, "The lunar dust environment," *Planetary and Space Science*, **59**, 14, 1672-1680 (2011), <https://doi.org/10.1016/j.pss.2011.04.005>.
43. E. L. CHRISTIANSEN, "Meteoroid/Debris Shielding," Technical report TO-2003-210788, NASA Johnson Space Center, Houston, TX, (2003).
44. M. I. ALLENDE, J. E. MILLER, B. A. DAVIS, E. L. CHRISTIANSEN, M. D. LEPECH, and D. J. LOFTUS, "Prediction of micrometeoroid damage to lunar construction materials using numerical modeling of hypervelocity impact events," *International Journal of Impact Engineering*, **138**, 103499 (2020), <https://doi.org/10.1016/j.ijimpeng.2020.103499>.
45. J. ARNOLD, E.L. CHRISTIANSEN, A. DAVIS, J. HYDE, D. LEAR, J.C. LIOU, F. LYONS, T. PRIOR, G. STUDOR, M. RATLIFF, and S. RYAN, "Handbook for Designing MMOD Protection," Technical report JSC-64399, NASA Johnson Space Center, Houston, TX, (2009).

46. B. COUR-PALAIS, "Meteoroid protection by multi wall structures," *Proceedings of the Hypervelocity Impact Conference*, Cincinnati, OH, AIAA (1969).
47. K. L. KARR, C. C. POTEET, and M. L. BLOSSER, "Hypervelocity Impact Test Results for a Metallic Thermal Protection System," Technical report NASA/TM-2003-212440, NASA Langley Research Center, Hampton, VI, (2003).
48. S. RYAN and E. L. CHRISTIANSEN, "A ballistic limit analysis programme for shielding against micrometeoroids and orbital debris," *Acta Astronautica*, **69**, 245-257 (2011), <https://doi.org/10.1016/j.actaastro.2011.04.012>.
49. W. P. SCHONBERG, "Concise history of ballistic limit equations for multi-wall spacecraft shielding," *REACH - Reviews in Human Space Exploration*, **1**, 46-54 (2016), <https://doi.org/10.1016/j.reach.2016.06.001>.
50. G. CORDERLEY, F. MOSTERT, and J. J. KRUEGER, "Failure modes in a carbon / titanium fiber metal laminate under hypervelocity impact," *International Journal of Impact Engineering*, **125**, 180-187 (2019), <https://doi.org/10.1016/j.ijimpeng.2018.11.011>.
51. T. M. SCHRIENER and M. S. EL-GENK, "Armor Analyses of Lightweight, Heat Rejection Radiator Modules on the Lunar Surface," *Nuclear Technology* (submitted, 2024)
52. ECSS SECRETARIAT, "Space engineering: Spacecraft mechanical loads analysis handbook," ECSS-E-NB-32-26A, ESA Requirements and Standards Division, Noordwijk, The Netherlands (2013).
53. D. KERN and T. SCHARTON. "NASA handbook for spacecraft structural dynamics testing." *Proceedings of the 5th International Symposium on Environmental Testing for Space Programmes*, Noordwijk, The Netherlands (ESA SP-558, June 2004). Compiled by: K. Fletcher, **558**, 375-384 (2004).
54. MARSHALL SPACE FLIGHT CENTER, "MSFC Technical Standard: Development of Vibroacoustic and Shock Design and Test Criteria Standard," MSFC-STD-3676, Marshall Space Flight Center, Huntsville, AL (2017).
55. SPACEX, "Falcon User's Guide," Space Exploration Technologies Corp., Hawthorne, CA (2021).
56. UNITED LAUNCH ALLIANCE, "Delta IV Launch Services User's Guide," United Launch Alliance, LLC, Centennial, CO (2013).
57. A. ISRAR, "Vibration and Model Analysis of Low Earth Orbit Satellite," *Shock and Vibration*, 1-8 (2014). <http://dx.doi.org/10.1155/2014/740102>.
58. E.E. UNGAR, "Fundamentals of Statistical Energy Analysis of Vibrating Systems," AFFDL-TR-66-52, Air Force Flight Dynamics Laboratory, Dayton, OH (1966)
59. B. HANSON, "The Selection and Use of Titanium, A Design Guide," Institute of Materials, Minerals & Mining, London, UK (1995).
60. R. VON MISES, "Mechanik der festen Körper im plastisch-deformablen Zustand". *Mathematisch-Physikalische Klasse*, **1**, 582–592 (1913).
61. J.M. BERRY and J.J. GEBHARDT, "Mechanical properties of pyrolytic graphite." *AIAA Journal*, **3**, 2, 302-308 (1965).
62. M. ISHIHARA, J. SUMITA, T. SHIBATA, T. IYOKU, and T. OKU, "Principle design and data

of graphite components," *Nuclear Engineering and Design*, **233**, 1-3, 251-260 (2004).